A STUDY OF ION LINE BROADENING IN THE TORMAC DISCHARGE.

Shaw, Robert Stephen

1980-07-01

√

LBL-10748

Lawrence Berkeley Laboratory
UNIVERSITY OF CALIFORNIA

Accelerator & Fusion
Research Division

MASTER

A STUDY OF ION LINE BROADENING IN THE TORMAC DISCHARGE

Robert Stephen Shaw
(Ph.D. thesis)

July 1980

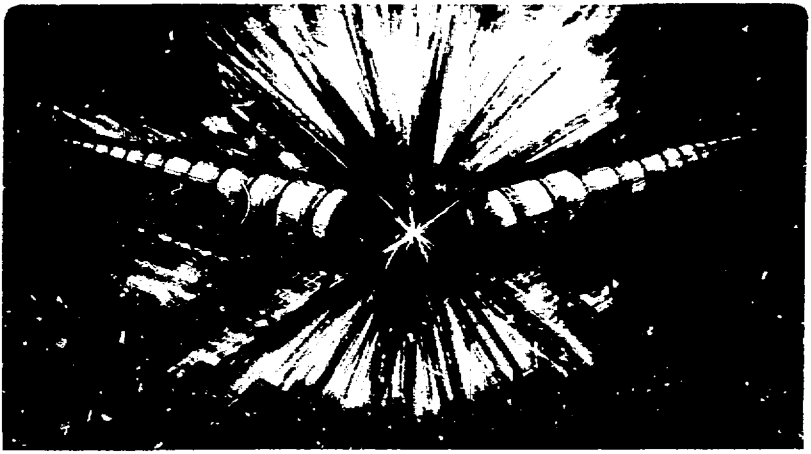

Prepared for the U.S. Department of Energy under Contract W-7405-ENG-48

A Study of Ion Line Broadening in the Tormac Discharge

By

Robert Stephen Shaw

Ph.D. Thesis

Lawrence Berkeley Laboratory
University of California
Berkeley, CA 94720

July 1980

A STUDY OF ION LINE BROADENING
IN THE TORMAC DISCHARGE

Table of Contents

A STUDY OF ION LINE BROADENING IN THE TORMAC DISCHARGE

Robert Stephen Shaw

Department of Physics, University of California
Lawrence Berkeley Laboratory, Berkeley, California 94720

ABSTRACT

Tormac (Toroidal Magnetic Cusp) is a magnetic confinement plasma concept having absolute minimum-B geometry. Two versions of Tormac are considered here. Tormac T IV-c has a glass vessel of rectangular cross section, 0.5 m in diameter. The confinement field rises to ~ 4.5 kG in ~ 8.3 μsec. Tormac T V has a T-shaped glass vessel, 1 m in diameter, with a field of ~ 3 kG, rising in ~ 10 μsec.

Gaussian HeII 4686 Å spectral lines having full widths at half maximum over 2 Å have been observed in both Tormac plasmas. Interpretation of these widths as due to thermal Doppler broadening would give ion temperatures of > 100 eV, in contradiction with other diagnostics. Indications are that these widths are not simply explained either by thermal Doppler broadening, or Stark broadening due to interparticle fields. Magnetic probe measurements indicate that compressional Alfven modes are excited by the main containment field rise in T IV-c. No indication of this was found in T V. The fluid motion associated with this mode is used to explain the broadening of HeII 4686 Å during cusp field rise in T IV-c, at which time the broadening is greatest. After field peak, the broadening is explained as Stark broadening due to turbulence excited by a large toroidal plasma current, which persists long after cusp peak. This current is larger in T V, and is taken as the sole mechanism for the line broadening.

I. INTRODUCTION

Tormac Concept

Since the early 1950's, the idea of producing power from fusion reactions has appeared very attractive. A virtually inexhaustible supply of fuel for these reactions was known to exist as naturally-occurring deuterium in the waters of the ocean. The many advantages of fusion power include the lack of radioactive waste products, absence of a waste heat problem, inherent safety against nuclear explosions, and the possibility of direct conversion of charged particle energy into electrical energy, bypassing inefficient heat exchangers.

To produce fusion reactions, the nuclei of the interacting particles must be given enough energy to overcome their coulumb repulsion. To do this, the fuel must be heated to temperatures of 10^8-10^9 °K, as in the interior of stars. In addition, the fuel must be contained long enough for a significant number of fusion reactions to occur. One approach is to use magnetic fields to keep the plasma away from any material walls, interaction with which could contaminate and cool the plasma.

Many magnetic field configurations have been proposed and pursued, the Tokamak and the magnetic mirror being the most popular. However, numerous economic and technical requirements must be met for any design to become commercially viable. A number of smaller power plants are preferable over a very large, centralized plant, as they would side-step the problem of transporting power over large distances. In order to achieve adequate confinement time in a Tokamak reactor, the reactor must be made uneconomically large. Further, efficient use of containment magnetic fields is a definite advantage. This property may be described by the β, which is the ratio of contained plasma pressure to the magnetic field pressure [$\beta = (8\pi p/B^2)$]. The higher the β, the more plasma pressure may be held by a given magnetic field. Containment schemes which rely on closed magnetic field lines, such as the Tokamak, have good particle containment properties, but are found to have a β limit, above which instabilities occur and cause loss of plasma confinement. In Tokamak, this β limit is thought to be a few percent. Therefore, to confine a quantity of plasma in a Tokamak, much power must be used to produce the confining magnetic field -- resulting in a large reactor.

Open magnetic field line configurations, such as the magnetic mirror, do not have this β limitation. However, particle confinement on open lines is poor, so that only a fraction of the fuel is burned while the rest is lost.

Tormac, toroidal magnetic cusp, is a magnetic containment scheme having an absolute minimum-B geometry; i.e., the plasma is contained in a region where the magnetic field strength increases in every direction away from the plasma. It has been shown that absolute minimum-B devices are MHD stable, even at high values of β.[1,2,3] Unfortunately, absolute minimum-B configurations require open magnetic field lines.[4,5,6] Tormac uses both open and closed magnetic field lines; the open lines provide stability, while the closed lines give good particle confinement. The closed lines are in the toroidal direction and are generated by currents along the axis of the system. The bulk of the Tormac plasma is located on these closed field lines, while a thin sheath a few ion gyroradii wide separates this central region from the open field lines (see Fig. 1). The open field lines are in the form of a bicusp. Figure 2 compares the Tokamak and Tormac geometries. Note that the poloidal field is dominant at large major radius, while the toroidal field is dominant at small major radius. The advantage of this magnetic field geometry is that a high β plasma may be stably contained and that particle losses may be kept low.

A simple cusp, without the internal closed field lines, is shown in Fig. 3. This configuration has absolute minimum-B, and is therefore MHD stable. However, because of the low internal field magnitude, the particles move in essentially straight lines, until they are lost at the cusp points; i.e., the simple cusp acts as a container with holes at each of the cusp points. The particle motion is thus non-adiabatic. The flux of particles out one cusp is given by $\Gamma \sim \frac{1}{4} nv$, where v is the average velocity of the contained particles, and n is the density. Therefore, the number of particles per second lost per length out of a cusp line is given by

$$\frac{dN}{dt} \sim \frac{1}{4} nv\delta \quad ,$$

where δ is the effective hole size, usually taken as ρ_i.[7,8] The total number of particles per length is

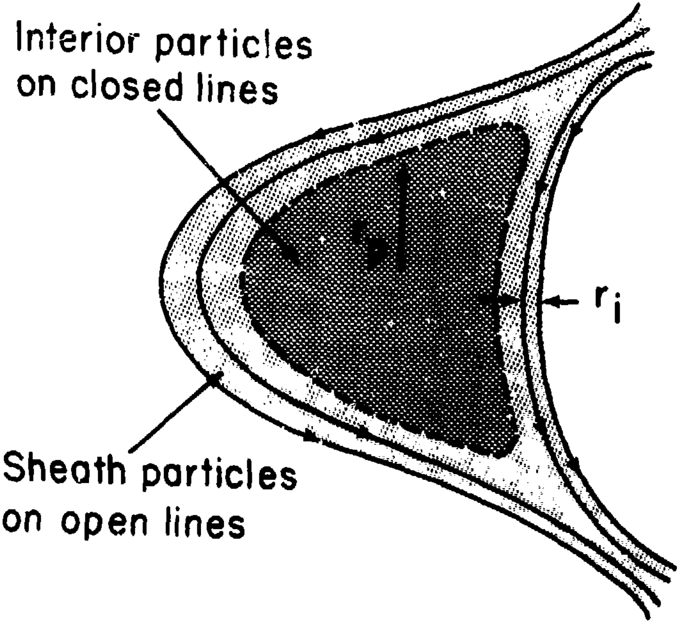

Tormac confinement

XBL 789-2224

Fig. 1

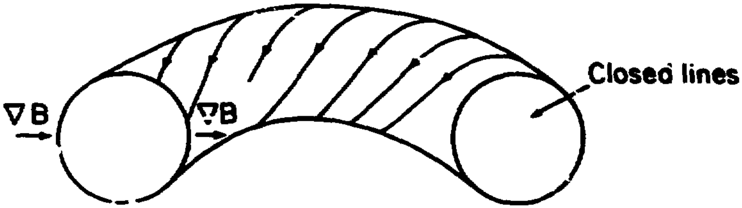

Tokamak average minimum-B geometry

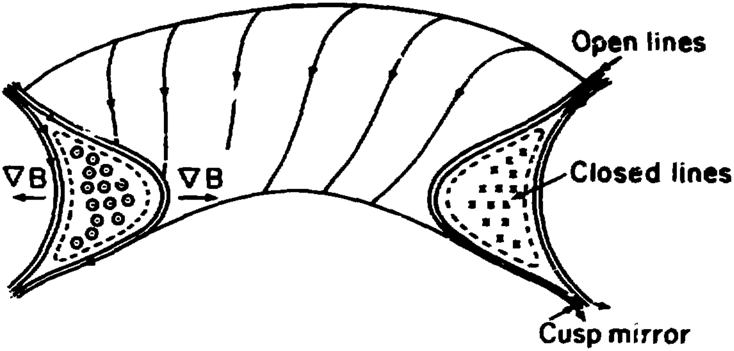

Tormac absolute minimum-B geometry

XBL 789-2222

Fig. 2. Schematic of the Tormac absolute minimum B configuration contrasted with the Tokamak average minimum B. In both cases, toroidal fields with a 1/R dependence provide favorable curvature at small major radius.

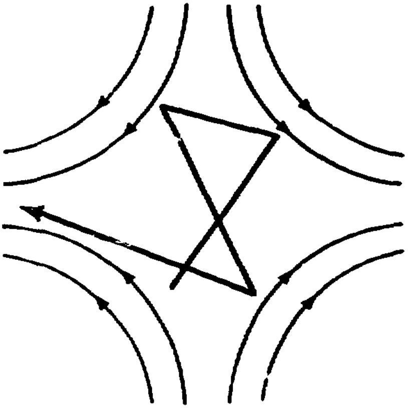

$$\dot{N} \sim -nv\delta$$

$$N \sim n r_p^2$$

$$\tau = \frac{-N}{\dot{N}} \sim \frac{r_p^2}{v\delta}$$

Particle loss in cusp fields

XBL 804-4146

Fig. 3

$$N = \pi r_p^2 n \quad ,$$

where r_p is the minor radius of the plasma. Then the containment time of a simple cusp is given by

$$\tau \sim \frac{-N}{dN/dt} \sim 4\pi \frac{r_p^2}{v\delta}$$

Setting $\delta = \rho_i$ and $v \sim (T/m)^{1/2}$

$$\tau \sim \frac{eB}{cT_i} r_p^2$$

Later theories of the cusp[9] make use of symmetries that may exist in the system. For example, a toroidal line cusp, as found in Tormac, has toroidal symmetry. This symmetry causes a generalized canonical momentum to be conserved, which in turn causes the particle motion to be different from a free gas escaping from a hole. Those particles not lost immediately need to undergo collisions in order to escape. Therefore, the confinement time for a symmetric cusp scales as τ_{ii}, the ion-ion collision time, just as a magnetic mirror.

In Tormac, a further lengthening of the confinement time is achieved by the closed field lines of the stuffing field.[10] Since there is field everywhere in the plasma, the particle motion in the bulk of the plasma is adiabatic; i.e., magnetic field scale lengths in this region are longer than the gyroradii of the particles. An invariant is now present, which was not present in the unstuffed cusp.

The stuffing field, therefore, sets up two distinct regions: an interior region having plasma with frozen-in closed magnetic field lines and an external region having open magnetic field lines. These two regions are separated by a sheath. The magnetic field strength on the surface of the plasma is a constant and increases away from the plasma. Magnetic shear is strong inside the sheath.[11]

The plasma in the interior region is thought to be Maxwellian. Here, $\nabla p \approx 0$, since there are no poloidal currents. The plasma in the sheath, however, is mirror contained, having a confinement time $\sim\tau_{ii}$, as discussed above. The sheath then makes up the lost particles by drawing on the plasma in the interior region. There is a balance between particles lost from the sheath along the open field lines, and particles diffusing into the sheath from the bulk plasma. Balancing these two processes gives a value for the sheath thickness of $\sim \rho_i$.[7] Therefore, the picture of the Tormac particle loss is that particles are lost from the sheath along the open field lines with a time $\sim \tau_{ii}$, and the sheath eats into the bulk plasma to make up this loss. The particle containment time for Tormac is

$$\tau_{\text{Tormac}} \sim \tau_{ii} \frac{V_{\text{bulk}}}{V_{\text{sheath}}} \sim \tau_{ii} \frac{r_p}{2\rho_i} \quad .$$

This is quite an enhancement over the mirror confinement time and the unstuffed cusp confinement time:

$$\frac{\tau_{\text{Tormac}}}{\tau_{\text{Mirror}}} \sim \frac{r_p}{2\rho_i}$$

$$\frac{\tau_{\text{Tormac}}}{\tau_{\text{Cusp}}} \sim \tau_{ii} \frac{v}{r_p} \sim \frac{\lambda_i}{r_p} \sim \frac{\text{ion mean free path}}{\text{plasma radius}}$$

Both of these ratios can be made large. τ_{Cusp} and τ_{Tormac} are shown in Fig. 4. Note that both τ_{Cusp} and τ_{Tormac} scale ~B, whereas $\tau_{Cusp} \sim r_p^2$ and $\tau_{Tormac} \sim r_p$. To show the improved Tormac scaling over that of a simple cusp, a minimum ion temperature is required. This temperature increases as n increases, since $\tau_{Tormac} \sim \frac{1}{n}$, while τ_{Cusp} *does not depend on n*. At $n \sim 1 \times 10^{15} cm^{-3}$, this cross-over temperature is ~ 120 eV, for all magnetic field strengths.

For the Tormac scaling to occur, it is important for the two regions to remain separate; i.e., particles in the interior region having a Maxwellian distribution should not mix with the sheath particles having a loss cone distribution. To accomplish this, all the drift orbits of the interior region particles must be closed. These particles experience ∇B and curvature B drifts in the $\frac{1}{R}$ stuffing field (Fig. 5). A rotational transform is necessary to close these orbits. To compute this, let V_d be the drift velocity,[12] and ω_R be the circulation frequency in the poloidal direction.

$$V_d = \frac{cmV_{\parallel}^{\ 2}}{qRB} + \frac{cmV_{\perp}^{\ 2}}{2qRB} = \frac{1}{R\Omega_i}\left(V_{\parallel}^2 + \frac{V_{\perp}^{\ 2}}{2}\right) ,$$

where R is the major radius, q is the charge, $V_{\parallel}$ and $V_{\perp}$ are the components of the particle velocity parallel and perpendicular to B, and

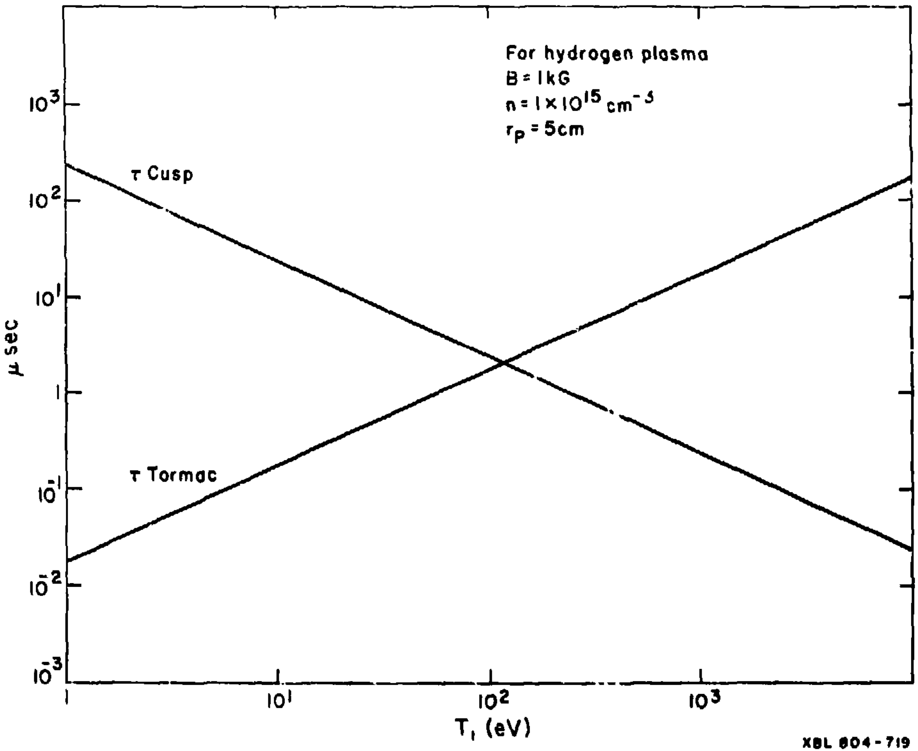

XBL 804-719

Fig. 4. Cusp confinement time and Tormac confinement times vs ion temperature.

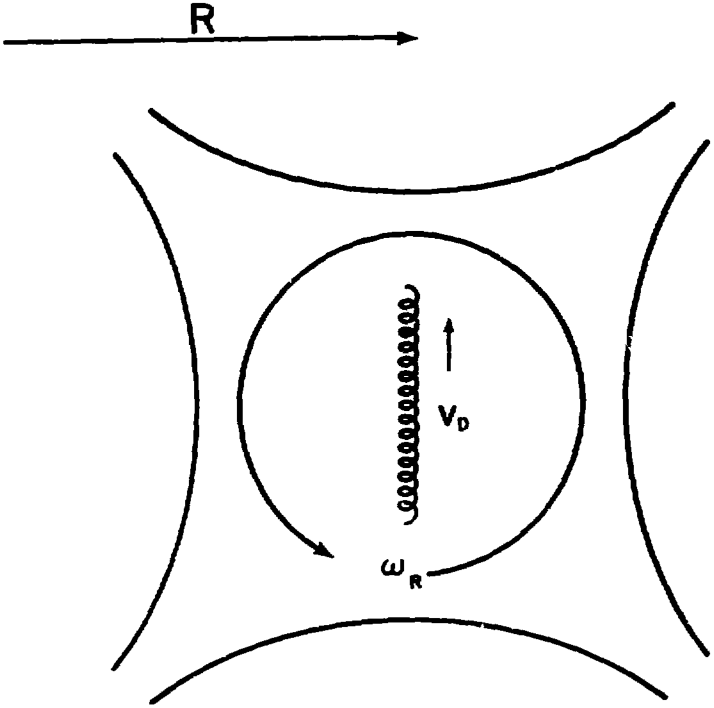

Geometry for drift orbit calculation

XBL 789-2206

Fig. 5. V_D IS THE DRIFT VELOCITY IN THE NONUNIFORM INTERNAL TOROIDAL FIELD. ω_R IS THE CIRCULATION FREQUENCY AND IS DETERMINED BY THE ROTATIONAL TRANSFORM AND THE PARALLEL VELOCITY OF THE PLASMA PARTICLES.

$$\Omega_i = \frac{qB}{M_i C}.$$

For these orbits to close, the time it takes the particle to drift across the plasma, t_d, should be longer than the time it takes to make one poloidal rotation, τ.

$$t_d = r_p/V_d$$

$$\tau = \frac{2\pi}{\omega_R} \qquad .$$

Now let ι be the rotational transform:

$$\iota = \frac{2\pi R\ B_p}{r_p B_T} \qquad ,$$

where B_p is the poloidal magnetic field and B_t is the toroidal magnetic field. ι is the angle in the poloidal direction through which a field line rotates for one complete rotation in the toroidal direction.

$$\omega_R = \omega_T \frac{\iota}{2\pi} \sim \frac{V_{\parallel}}{R} \frac{\iota}{2\pi}$$

where ω_T is the circulation frequency in the toroidal direction, and it is assumed that $B_T >> B_p$ in the bulk plasma. Therefore,

$$\tau = \frac{4\pi^2 R}{V_{\parallel}\,\iota}$$

For the drifts to close, $\tau < t_d$, so

$$\frac{4\pi^2 R}{V_\parallel \iota} < \frac{r_p}{V_d} = \frac{r_p\ R\Omega_i}{(V_\parallel^2 + V_\perp^2/2)} .$$

This implies that

$$\iota > \frac{4\ \sqrt{2}\pi^2 \rho_i}{r_p} ,$$

and

$$B_p > 2\ \sqrt{2}\ \pi\ B_T \quad \left(\frac{r_p}{R}\right) \quad \left(\frac{\rho_i}{r_p}\right) .$$

Since both $\left(\frac{r_p}{R}\right)$ and $\left(\frac{\rho_i}{r_p}\right)$ may be small, not much poloidal field is needed.

In addition to this rotational transform, it is necessary for the sheath to be stable. Sheath structure and stability have been examined, but various problems remain unsolved.[7,11,13,14] Microinstabilities are expected to play a role in sheath structure and stability, due to large gradients, the lost cone distribution, anisotropic pressure, and large drift velocities present in the sheath. However, high β as well as magnetic sheer provide a stabilizing influence.[15-20]

Several versions of the Tormac concept have been built and operated.[21-26] This thesis is concerned with diagnostic studies in two versions, T IV-c and T V. In particular, it deals with an explanation of helium ion line broadening that had been intended as a means to determine the ion temperature in the Tormac discharges.

Problem

HeII 4686 Å is widely used as a plasma diagnostic.[27-29] Its applicability depends on the density, temperature, and nature of plasma formation. Primarily used as an ion temperature diagnostic in low temperature plasmas, the lines are interpreted as being broadened by the thermal Doppler effect. For Maxwellian ions, the line shape is Gaussian, and the full width at half maximum gives the ion temperature. Gaussian HeII 4686 Å spectral lines having widths corresponding to ion temperatures of $\gtrsim$ 100 eV are routinely obtained in Tormac.[30] However, Thomson scattering measurements indicate an electron temperature of ~ 5 eV. At this temperature and density, ~ 3×10^{15} cm^{-3}, electron drag would drain any initial ion energy in a time less than the duration of the observed broadening, and power input is inadequate to sustain high ion temperature in the presence of such drag. Magnetic probes indicate that the confinement field rapidly penetrates the entire plasma. Therefore, the plasma is on open field lines in contact with the walls, and is expected to remain cold, since energy would rapidly be conducted along these open lines to the walls.

Additional evidence of a cold plasma is available. No X-rays were detected by B. R. Myers with an X-ray detector on T IV-a. Spectroscopic measurements using line to line and line to continuum indicate an electron temperature of < 10 eV in T IV and T V.[31] Measurements done by B. Feinberg on T V using a Faraday cup showed an electron temperature of < 10 eV.

An upper bound on the plasma temperature may be estimated from the energy deposition on the glass walls, following Reference 32. Since no marks were left on the T IV-a pyrex vessel where plasma streaming out the cusp points is expected to contact the glass (the mirror points are on the glass in T IV),

$$T < \frac{7.55 \times 10^9}{n^{2/3}\ t_b^{\ 1/3}} ,$$

where T is the temperature in eV, n is the plasma density in cm^{-3}, and t_b is the time required for the glass surface to reach its boiling temperature. This assumes that no net current goes to the vessel walls, and that the flux of particles is $\sim \frac{1}{4}\, nv_i$. If t_b is taken to be 10 μsec, which is the approximate length of time of the density compression (Fig. 39), and $n \sim 3 \times 10^5$ cm^{-3}, then $T < 20$ eV.

The temperature inferred from HeII 4686 Å widths is far above that at which helium should be fully ionized. Stark broadening due to interparticle fields is relatively small at these densities. All diagnostic and other evidence, except the interpretation of the broadening of HeII 4686 Å as due to the thermal Doppler effect, indicates that the Tormac plasma is dense and cold. The problem addressed by this thesis is, then, why these spectral lines are so broad and Gaussian. It will be demonstrated that a combination of mass motion associated with driven compressional Alfven modes, and the Stark effect due to turbulence can account for this broadening.

II. EXPERIMENTAL APPARATUS

A. Tormac T IV-c

The T IV-c experiment is the smaller of the two considered here.[7,21,33,34,35] The vacuum vessel is a glass toroid of rectangular cross section (Fig. 6). The dimensions and coil locations are illustrated in Fig. 7. The details of construction have been discussed elsewhere[34,35] and will only be summarized here.

The vacuum vessel is pyrex and is pumped by a turbomolecular pump (260 l/sec) to a base pressure of 1×10^{-7} Torr. The main bicusp windings consist of a copper axial conductor, for creating the toroidal component of the bicusp field, in series with 100 parallel wires wrapped in solenoid of varying pitch, for the poloidal component of the bicusp field. This series arrangement was done to ensure that the ratio of poloidal to toroidal current was constant throughout the pulse. This, together with backwinding, helps decouple this coil from other coils. The main bank, consisting of eight 14.1 μf capacitors in parallel, has a total capacitance of 113 μf and is normally charged to 15 kV. It is switched by eight 7703-type ignitrons, one for each capacitor, and has a rise time of ~8.3 μsec. Sixteen low-inductance cables run from the bank to a two copper plate arrangement, across which are four 5555-type ignitrons, which serve as crowbars. An 8-inch wide strip line connects this to the experiment. The measured inductance is ~ 300 nH and resistance is ~ 7mΩ, giving a peak current of

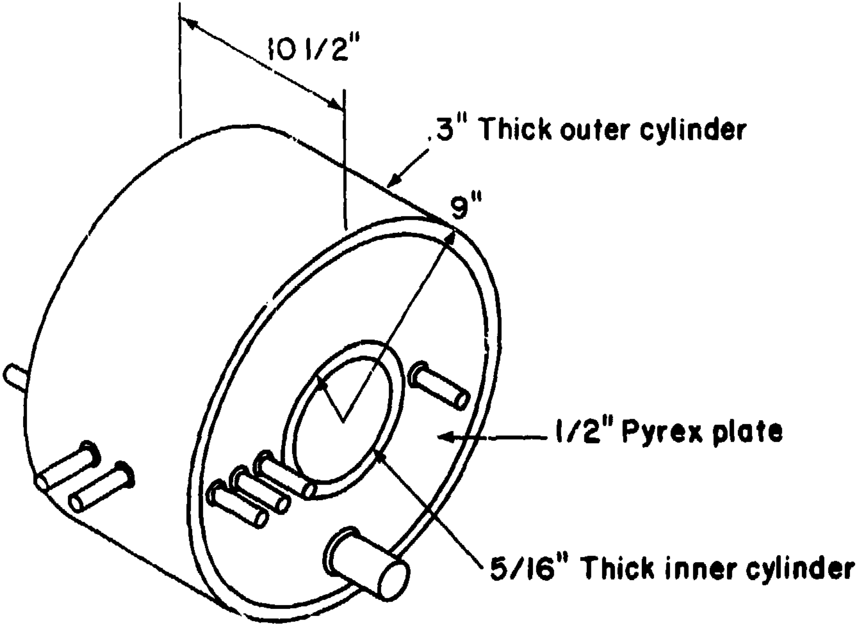

Glass vessel and access

XBL 789-2219

Fig. 6

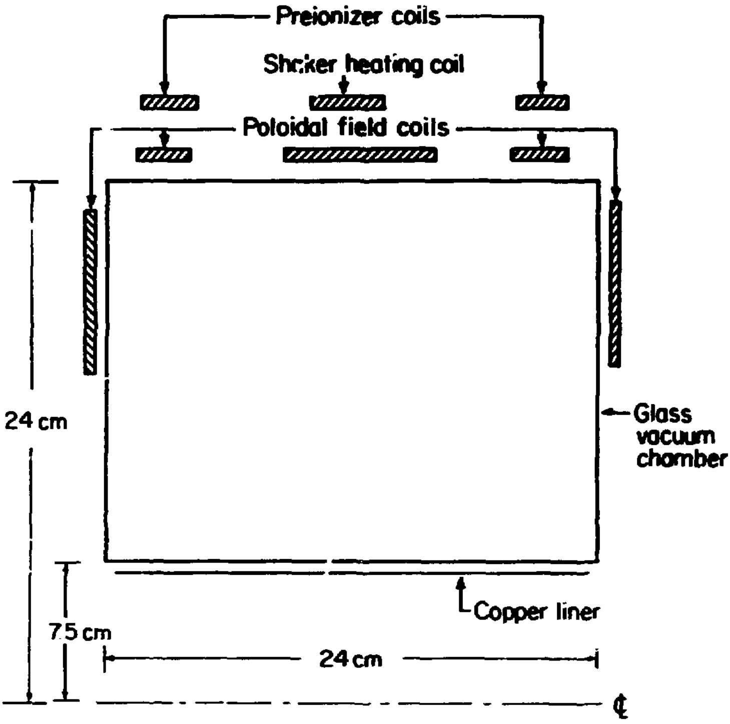

XBL 794-1281A

Fig. 7. A schematic of the T IV vessel showing dimensions and coil locations. The device is toroidally symmetric around the indicated center line.

~ 260 kA for 15 kV charging voltage. This gives a peak field at the plasma surface of ~ 4.5 kG. The poloidal field lines produced by these coils are shown in Fig. 8. The |B| contours are shown in Fig. 9. The absolute minimum-B is clearly seen.

The preionization bank consists of two sections: 1) a low-frequency (~ 120 kHz) bank having one 2.14 μf capacitor driving a pair of toroidal two-inch wide straps in parallel, and 2) a high-frequency (~ 300 kHz) bank having two 0.04 μf capacitors driving two toroidal loops in parallel, one on each end of the vessel. Both banks are charged in parallel to 25-30 kV and fired by a spark gap. They are crowbarred by means of two 7703-type ignitrons.

The bias field is created by an 8-turn solenoid powered by a 375 μf capacitor charged to 1-4 kV. The rise time is ~ 200 μsec. This bank is meant to apply a field of ~ 150-600 G, which remains essentially constant throughout the experiment.

A shaker heating bank, the coils of which are illustrated in Fig. 7, was used on T IV-a, an earlier experiment, as a means of heating the plasma. This bank was to launch magneto-acoustic waves into the plasma, where they would be absorbed. A small effect was noted with spectroscopic diagnostics at pressures below 50 mTorr and no effect was seen above 50 mTorr. Shaker heating is not used in the experiments reported here.

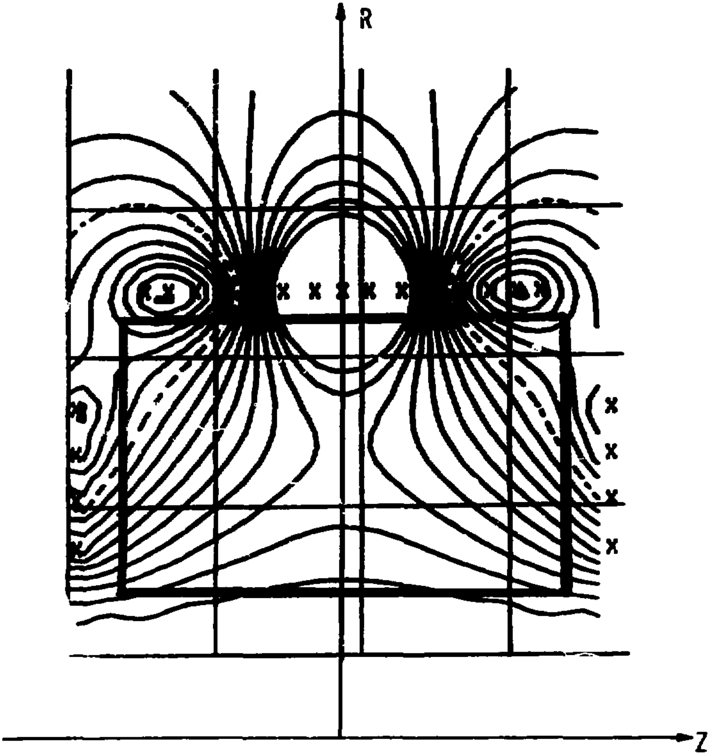

Fig. 8. POLOIDAL FIELD LINES (PSI CONTOURS) OUTPUT FROM VACUUM FIELD PROGRAM. THE POSITION OF THE GLASS VESSEL IS SHOWN BY HEAVY LINES.

XBL 789-11085

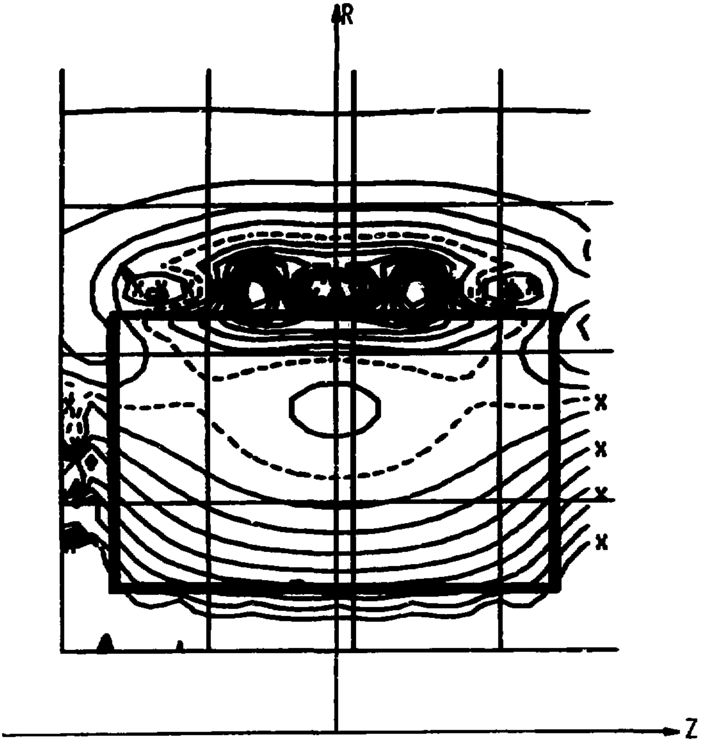

Fig. 9. |B| CONTOURS, OUTPUT FROM VACUUM FIELD PROGRAM. THE POSITION OF THE GLASS VESSEL IS SHOWN BY HEAVY LINES.

XBL 789-11084

The experimental sequence, illustrated in Fig. 10, begins with the introduction of a gas mixture (80% H_2, 20% He) into the vessel at 10 to 100 mTorr. The slowly-rising bias field is applied. The two preionization banks are then discharged. They induce toroidal electric fields which ionize the gas, freeze in the bias field, and generate a toroidal current. This current of a few kA supplies the rotational transform necessary for Tormac scaling. After about 15 μsec, the main bank is discharged, rising to ~ 4.5 kV in ~ 8.3 μsec. The cusp field induces toroidal currents, which are necessary for the high β equilibrium. At the peak of the cusp field, the preionization banks are crowbarred.

B. Tormac T V

T V is a much larger device,[23,25,36] as shown in Fig. 11. In T IV, the mirror point, i.e., that is the point of strongest magnetic field following the poloidal field towards the cusp point, occurs outside the vessel. This means that the particles in the sheath are in communication with the walls and are never expected to get hot. In T V, however, the "T" sections were made so that the mirror points are located inside the vessel away from the walls. This means that the contained particles are not touching the walls. Further, particles that do escape through the cusp, as well as any impurities from the wall, have trouble getting into the plasma, since they must climb a magnetic barrier. This is illustrated in Fig. 12, showing the poloidal field lines, and in Fig. 13, showing the |B| surfaces for T V. The purpose of T V was to test Tormac confinement scaling.

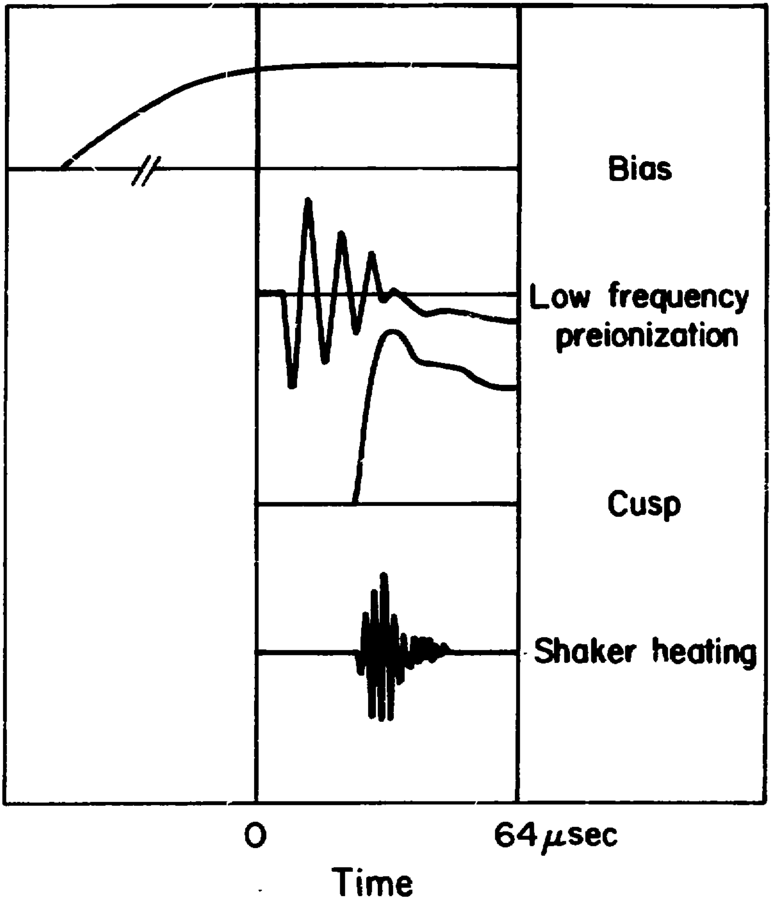

XBL 804-4144

Fig. 10 The T IV experimental sequence.

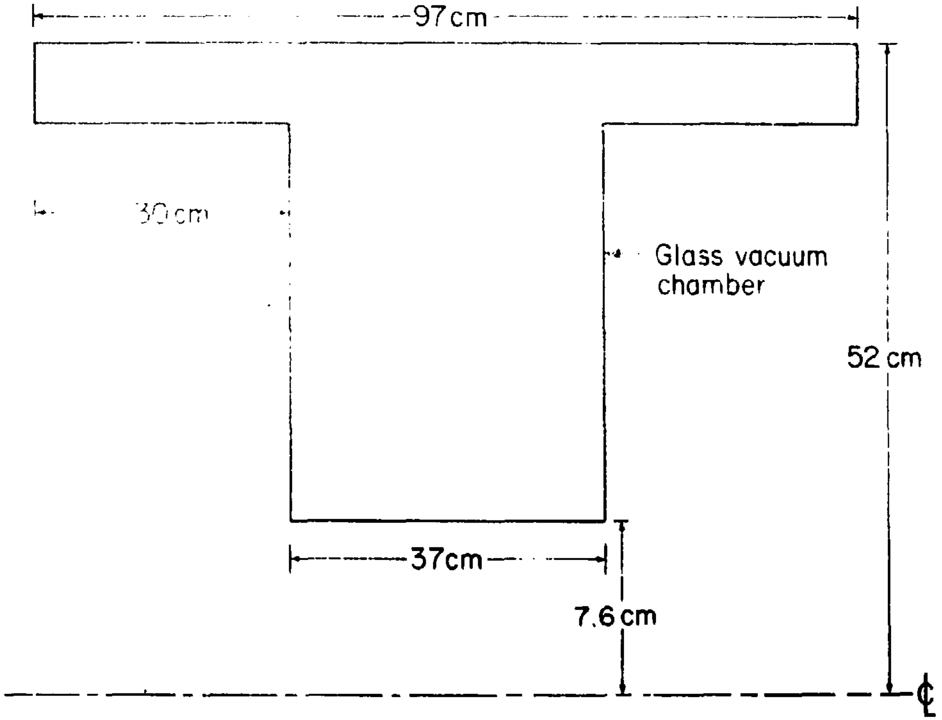

Fig. 11. Schematic of the TV vessel. The device is toroidally symmetric around the indicated center line.

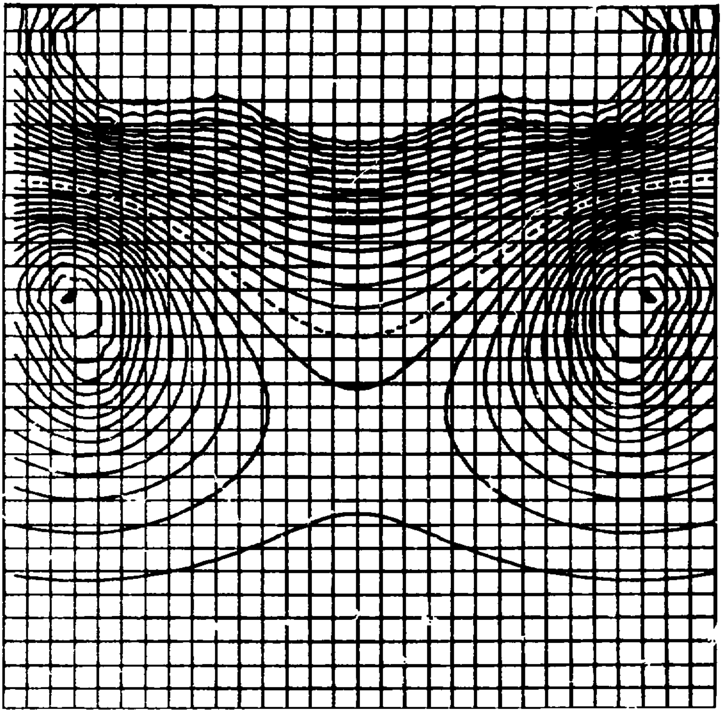

XBL 781-315

Fig. 12. Poloidal field lines (Psi contours) output from vacuum field program for TV.

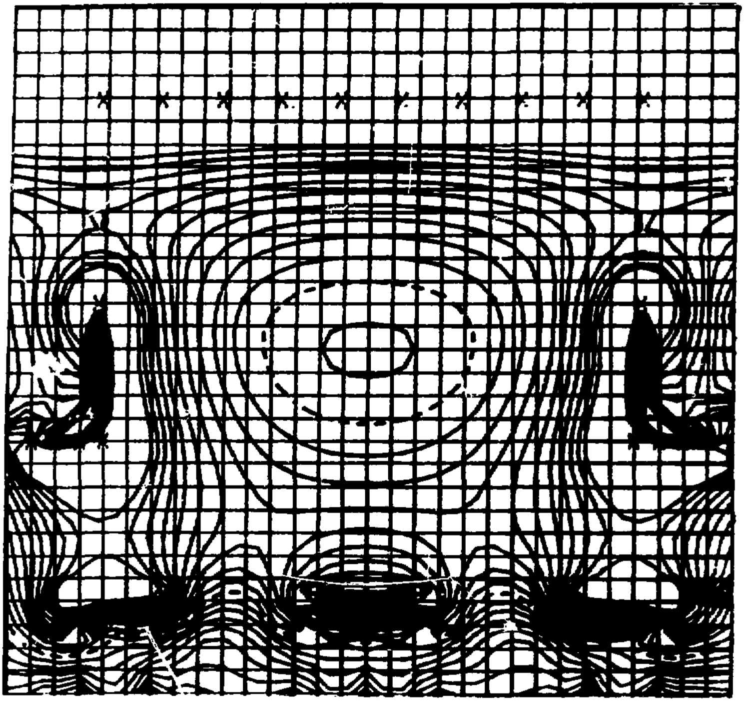

XBB 803-3028

Fig. 13. |B| contours, output from vacuum field program for TV.

The T V vessel is pyrex, and is pumped to a base pressure of 5×10^{-7} Torr by a turbomolecular pump. The cusp windings are very similar to those of T IV. They consist of 132 parallel conductors mounted in lexan and wound into a solenoid of varying pitch. There is a copper center conductor in series with this winding to provide the toroidal component of the field. The cusp capacitor bank is different from that of T IV, since it is meant to store much more energy. The bank consists of three sub-banks, which are charged in parallel and discharged in series. The total capacitance is 81.6 μf, charged effectively to 36 kV. This has a stored energy of ~ 53 kJ, compared with 13 kJ in T IV-c. The bank is switched by 7703-type ignitrons mounted in the bank, one for every two capacitors. The containment field windings may be thought of as three sections in series. Low-inductance cables lead from the three sections of the capacitor bank to the three sections of the main coil, as illustrated in Fig. 14. The rise time is ~ 10 μsec, giving an inductance of ~ 1.0 μH and a resistance of ~ 10mΩ. The bank is crowbarred by 7703-type ignitrons mounted directly on the windings at the vessel, 8 ignitrons for each of the three sections. There was much trouble with this crowbar arrangement, which was responsible for the low limit of the charging voltage. The field at the plasma was ~ 3 kG for normal operation.

The preionization bank was redone while T V was in operation. Originally, a simple arrangement was used as in T IV; i.e., a small bank powered four toroidal coils. It was discovered,[37,38] however, that the start-up phase in Tormac is very important. Before the main

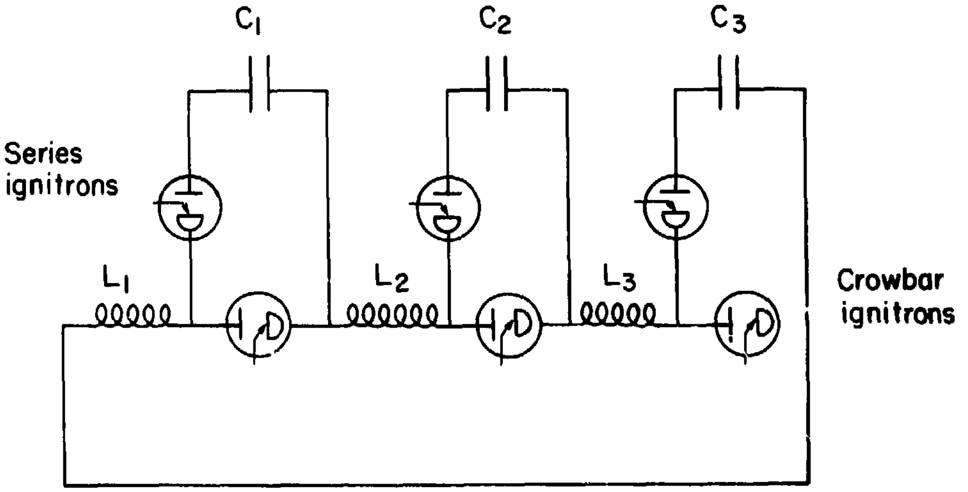

XBL 804-4149

Fig. 14. Schematic of the cusp field generating circuit in T V.

bicusp field is applied, the bias and preionize banks are expected to produce a toroidal Z-pinch plasma; i.e., a toroidal field is frozen into the plasma, and a toroidal current is induced, giving the lines a helical twist. It was known that in T IV the safety factor,

$$q = \frac{r_p \, B_T}{R \, B_p} \quad ,$$

was less than 1; the preionization phase was not Tokamak-like. From Z-pinch experience, it was found that the most stable discharges occurred when the pinch parameter $\theta = B_p/B_T$ satisfies

$$1.2 \leq \theta \leq 2$$

For $\theta > 2$, relaxation to a stable $\theta \leq 2$ regime by rapid short wavelength instabilities have been observed in Z-pinches.[39] Since T IV has $\theta \geq 2.4$, this relation to a stable regime may play a role in Tormac start-up. With the simple preionization bank, start-up in T V was very difficult. The Z-pinch discharge was very unstable and could not be expected to last long enough for the cusp to provide stability. Therefore, the preionization bank was redone in order to produce a θ more like T IV, the start-up of which was believed successful. This entailed producing more toroidal current in the plasma, and having the correct "vertical fields" for equilibrium. This was done, as illustrated in Figs. 15 and 16, by having three sets of windings: 1) windings toroidally around the outside of the vessel, 2) windings on each

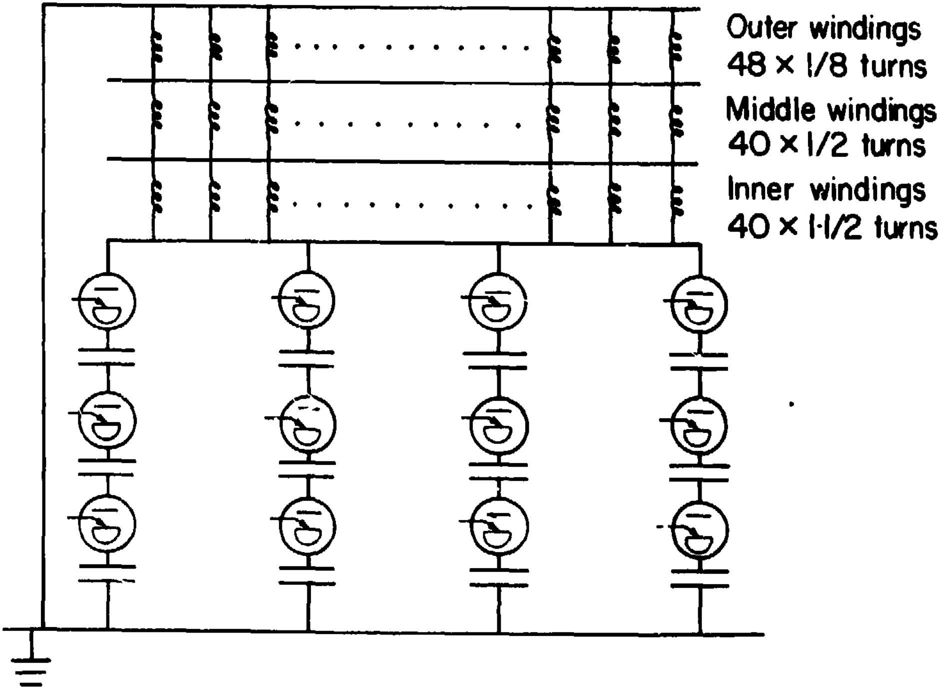

Fig. 15. Schematic of the preionization field generating circuit in T V.

XBL 804-4158

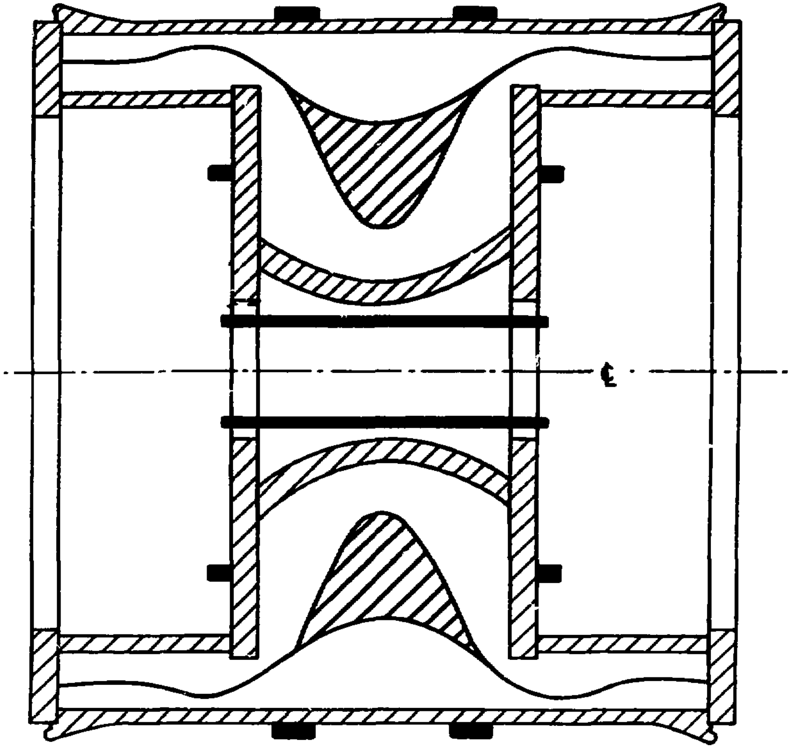

XBL 757-4469A

Fig. 16. Preionization coil locations in T V.

side of the vessel, and 3) windings inside the axial core of the device. These windings were powered by a bank consisting of 12 capacitors, a parallel arrangement of three in series (see Fig. 15). The three were charged in parallel and discharged in series in a Marx arrangement. The total capacitance was 19.3 μf, with an effective charging voltage of 40 kV. The bank, switched with a 7703-type ignitron mounted on each capacitor, rang with a frequency of 50 kHz, and was not crowbarred.

The bias field windings consist of a 16-turn solenoid, 4 turns in series and 4 of these in parallel. The bias bank had six 375 μf capacitors in parallel, charged to 3 kV and switched by a single 7703-type ignitron. The rise time is ~ 230 μsec, and the field at the plasma center is ~ 500 G.

A shaker heating arrangement was used on T V at one time. Not much effect was noticed, and for the experiments reported here, no shaker heating was used.

The experimental sequence is the same on T V and T IV. The gas mixture (80% H_2, 20% He) is introduced and the bias bank discharged. When the bias peaks, the preionization bank is fired, breaking down the gas and creating a toroidal current of up to 100 kA. The cusp field is then applied at ~ 23 μsec after the preionize, peaks in ~ 13 μsec to a value of ~ 3 kG and is crowbarred. The preionization bank was not crowbarred.

C. Diagnostics - T IV

A number of diagnostics have been used on Tormac, and will be discussed below:

(1) Magnetic Probes: These probes are used to record the time variation of various components of the magnetic field at a number of spatial positions throughout the vessel. Two probes are used: a radial probe is inserted into the vessel radially at the axial center, an axial probe is inserted into the vessel at fixed major radius and can be moved parallel to the axis. Each probe consists of two separate coils, wound in such a way as to measure mutually-perpendicular components of the magnetic field. These coils were wound on a 2.5 mm diameter wooden stick and placed inside a 4 mm diameter 12 inch long quartz tube (Fig. 17).

The coils of the radial probe are separated by 1 cm and are identical, except that their axes are perpendicular. Each coil consists of 15 turns of #37 wire, wound through 2 holes, drilled 7 mm apart through the wooden shaft. The axial probe has one coil wound as described above, and another coil in the form of a solenoid. This coil consists of 45 turns of #37 wire wound around the wooden shaft, and has a length of 7 mm. In both probes, the leads are twisted together in pairs and connected at the ends of the quartz tubes to 50 Ω RG178B cables. Each probe also has a null coil, consisting of a twisted pair of wires shorted at the end. This measures any electrostatic pickup or magnetic pickup in the leads.

XBB 789-12492

Fig. 17. Small magnetic probes used in T IV.

The probes enter the vessel through compression fittings. The typical data taking procedure is as follows:

a) The probe is moved to the desired spatial position and oriented to measure the various components of the magnetic field.

b) Data shots are repeated to ensure reproducibility or to measure shot to shot variation.

c) The probe is rotated 180° to see if the signals exactly reverse. This test is to ensure that the signals are magnetic in origin.

d) The null coil is occasionally checked to be sure that there is no stray signal. This coil always gave negligible signals.

From Faraday's law, the response of the probes is given by

$$V = 10^{-8}\, na \frac{dB}{dt} \quad ,$$

where V is the voltage out (in volts), n is the number of turns in the coil, a is the area of each turn in cm^2, and B is the field component in Gauss. To give the magnetic field, a passive integrator of time constant RC = 100 μsec is used, which gives

$$V = 10^{-4}\, na\, B \quad , \tag{1}$$

na for the coils is calculated to be 2.63 cm^2, while for the solenoid it is 2.2 cm^2. 100 μsec integrators are chosen since the longest time of interest in studying field penetration is the cusp risetime, which is ~ 8.3 μsec.

The probes are calibrated by putting them into a known magnetic field. This field is generated by discharging a 1 μf capacitor charged to 3 kV through a Helmholtz coil of radius 5.7 cm. Since the current through the coil can be measured, the magnetic field can be known accurately. The calibration of the probes is done using the 100 μsec integrators, which are separately calibrated. The measured na for the three coils is ~ 2.17 cm^2, while for the solenoid, na = 2.18 cm^2.

Equation 1 is valid for frequencies

$$\omega < R/L \quad .$$

The inductance of the coils is calculated to be 2.5 μH, and that of the solenoid to be 22 μH. Therefore, the probe-integrator system using 50Ω cable is good for frequencies up to 10 MHz.

The perturbation of the plasma by a quartz probe has been studied by Lovberg.[32] The time for which the probe may be used before boil-off of the quartz causes contamination of the plasma is given by

$$t = \frac{4.31 \times 10^{29}}{n^2 T^3} \text{ sec} \quad ,$$

where n is the density in cm^{-3}, and T is the temperature in eV. For the Tormac IV plasma, n ~ 3x10^{15} cm^{-3} and T ~ 5eV, so that t ~ 380 μsec. Therefore, for the times of interest in this experiment, the perturbation caused by the probe is not serious.

(2) <u>He-Ne Laser Interferometer</u>: The interferometer is used to determine the time variation of the integral of the electron density along the line of sight for lines of sight parallel to the machine axis at various major radii. Six holes, drilled into the fiberglass end panels protecting the vessel and supporting the coils, allow access to the plasma at the following major radii: 10.24 cm, 12.15 cm, 14.05 cm, 16.0 cm, 17.9 cm, and 19.8 cm (~ 1.9 cm separation). An end on view of the vessel is illustrated in Fig. 18, which shows 12 possible interferometer positions, of which only 6 were used. The interferometer is suspended above the vessel by springs and pulleys, and is easily lowered or raised into the desired position.

The arrangement of the interferometer components is illustrated in Fig. 19. The entire unit is built into a rigid fiberglass frame. This helps to cut down mechanical vibrations, and makes the interferometer very rugged and portable. The He-Ne laser (~ 5mW power) is mounted on top of the fiberglass, as is mirror 1 and the selsyn-controlled mirror. The other components are inside the hollow frame. All components have mounts with adjusting screws for fine adjustment of their orientation.

The laser light is led by mirrors 1 and 2 to the beamsplitter, where it is divided into two beams of approximately equal length. One beam goes through the plasma, to mirror 3, to the selsyn-controlled mirror, and back again to the beamsplitter. From there it goes through the filter-lens arrangement to a light pipe. The selsyn-controlled mirror is adjusted from outside the high voltage screen cage.

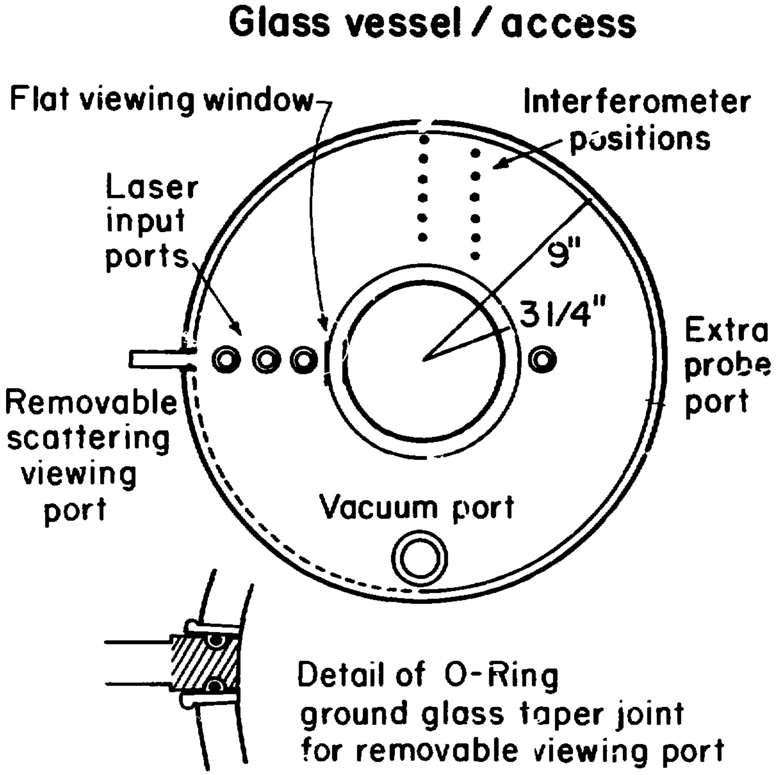

XBL 789-2220

Fig. 18

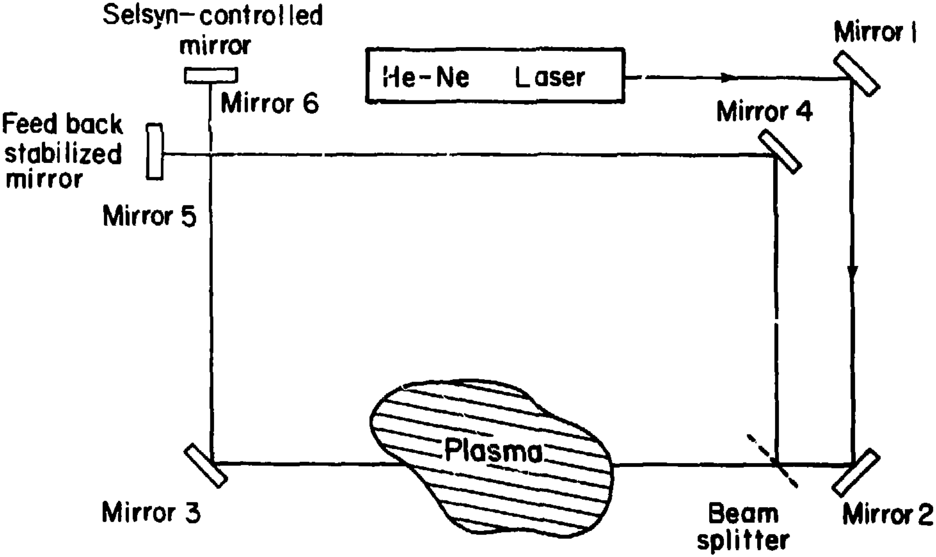

He-Ne Interferometer

XBL 804-4147

Fig. 19

Frequently during operation, this mirror is adjusted to give maximum intensity of the beam at the light pipe.

The reference beam goes from the beamsplitter to mirrors 4 and 5 and back to the splitter, where it interferes with the other beam at the light pipe. Mirror 5 is glued to the center of a small speaker (2 inches diameter), the position of which is controlled by a feedback network. The purpose of this scheme is to reduce the effect of mechanical and acoustic vibrations. The feedback network attempts to hold the fringe pattern constant, and can respond on a timescale of ~1 msec. The circuit cannot respond on the timescale of interest during a plasma shot (~ 100μsec) and, therefore, has no effect on the density data. Vibrations, however, are typically in the range of a few kHz and lower, and their effects are cancelled out. Stabilization to ~ $\frac{1}{1000}$ of a fringe can be obtained, while $\frac{1}{100}$ of a fringe is routinely obtained.

Interferometry is a measurement of the electron line density which does not perturb the plasma. It is based on the fact that the phase velocity of light is greater in the presence of plasma than in vacuum, and, therefore, the plasma introduces a phase shift which shifts the fringe pattern. The intensity information carried by the light pipe to the photo-detector may be written as

$$I = \text{average intensity at the light pipe} \propto \langle \underline{E}^* \cdot \underline{E} \rangle \quad ,$$

where the brackets indicate a time average, and $\underline{E}$ is the total electric field. $\underline{E}$ is made up of the two beams, and may be written as

$$\underline{E} = \underline{E}_1\, e^{i(\phi_1 - i\omega t)} + \underline{E}_2\, e^{i(\phi_2 - i\omega t)} \quad ,$$

where $\underline{E}_1$ and $\underline{E}_2$ are the electric field vectors of the two beams, ϕ_1 and ϕ_2 are the phase changes experienced during travel by the beams. Since the interferometer is constructed in such a way as to ensure that both beams are reflected the same number of times from identical mirrors and that they experience the same number of transits through the beamsplitter,

$$\underline{E}_1 = \underline{E}_2 \quad .$$

Therefore,

$$I \propto \cos^2\left(\frac{\Delta\phi}{2}\right) \quad ,$$

where

$$\Delta\phi = \phi_1 - \phi_2 \quad .$$

The individual total phase shifts are given by

$$\phi_1 = k_o D$$

and

$$\phi_2 = k_0\ (D-2d) + 2kd \quad ,$$

where D = total path length travelled by the beams,

d = distance through the plasma travelled by beam 2 (one way),

$k_0 = \omega_{laser}/c$,

$k = nk_0$,

and n = index of refraction.

Therefore,

$$\Delta\phi = 2k_0 d(1-n) \quad .$$

The index of refraction for a high frequency wave travelling in a plasma is given by

$$n = \left(1 - \frac{\omega_p^2}{\omega^2}\right)^{1/2} \sim 1 - 1.77 \times 10^{-22} N_e \ ,$$

where N_e is the electron density in cm^{-3}, and the He-Ne laser frequency is used. The phase difference depends linearly on N_e and

$$I \propto \cos^2 [1.76 \times 10^{-17} N_e d] \quad .$$

The electronics produces an output voltage V which depends linearly on I. The feedback stabilization circuit puts in an additional phase shift, which is adjusted before each shot to give maximum sensitivity of V to the electron density; i.e., when $N_e = 0$, $V = 0$. This is illustrated in Fig. 20. The line density may then be written as

$$N_e d = 2.84\times10^{16}\sin^{-1}\left(\frac{V}{V_f}\right)\ \mathrm{cm}^{-2},$$

where N_e = electron density,

d = length of one pass through the plasma,

V = output voltage,

and V_f = the maximum voltage out (at total constructive interference.)

Note that this assumes that the fringe shift is < 90°.

This result depends on the assumption that the index of refraction is not affected by the magnetic field. This will indeed be the case, since the laser frequency is so high compared to the plasma frequency and the gyrofrequency in the Tormac fields. Of course, at this frequency, ion motion may be neglected. For example, for propagation of a high frequency ($\omega \gg \Omega_e$) wave in a plasma, the index of refraction is given by[40]

$$n^2 = \begin{cases} \left(1 - \dfrac{\omega_e^2}{\omega^2} - \dfrac{\omega_e^2\Omega_e}{\omega^3}\right)^{1/2} & \text{for } \underline{k} \parallel \underline{B} \\ 1 - \omega_e^2/\omega^2 & \text{for } \underline{k} \perp \underline{B},\ \underline{B} \parallel \underline{E} \\ \dfrac{1}{\omega}\left[\dfrac{(\omega^2 - \omega_1^2)\ \ (\omega^2 - \omega_2^2)}{\omega^2 - \omega_H^2}\right]^{1/2} & \text{for } \underline{k} \perp \underline{B},\ \underline{B} \parallel \underline{E} \end{cases}$$

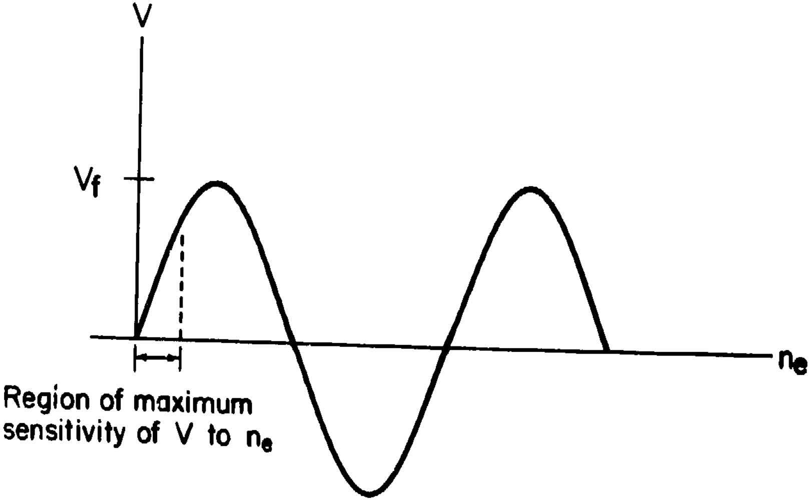

XBL 804-4150

Fig. 20. Interferometer output voltage vs electron density.

where

$$\omega_e^2 = \frac{4\pi N_e e^2}{M_e}$$

$$\Omega_e = \frac{eB}{M_e C}$$

$$\omega_1 = \frac{\Omega_e}{2}\left[-1 + \left(1 + \frac{4\,\omega_e^2}{\Omega_e^2}\right)^{1/2}\right]$$

$$\omega_2 = \frac{\Omega_e}{2}\left[1 + \left(1 + \frac{4\omega_e^2}{\Omega_e^2}\right)^{1/2}\right]$$

and $\omega_H^2 = \omega_e^2 + \Omega_e^2$. For this system, $\omega = 3 \times 10^{15}$ rad/sec,

$$\Omega_e \sim 7 \times 10^{10} \ \frac{\text{rad}}{\text{sec}} ,$$

and

$$\omega_e \sim 1.78 \times 10^{12} \ \frac{\text{rad}}{\text{sec}} ,$$

so

$$n^2 = \left(1 - \frac{\omega_o^2}{\omega^2}\right) \quad \text{to very good accuracy.}$$

Another possible modification would occur if the electrons undergo collisions at rate ν. In this case

$$n^2 = 1 - \frac{\omega_e^2}{\omega(\omega + i\nu)} .$$

However, in this plasma $\nu \sim 10^9$ sec^{-1} and, therefore, $\nu \ll \omega$, and collisions may be ignored. Also, for this plasma, finite temperature terms are of the order of 10^{-6} times the other terms, and may be neglected. Contributions to the index of refraction due to the presence of neutral atoms are considered unimportant.

(3) Spectroscopy: Spectroscopy has played a prominent role in the Tormac project, since this measurement does not perturb the plasma and the glass vessels provide ample access to the light. Since the gas used in these experiments is a combination of H_2 and He (80:20), both hydrogen and neutral and ionized helium light is collected. Light from impurity elements which might be present in the plasma is also examined.

These measurements are made using a 3/4 m Czerny-Turner type Spex spectrometer, modified to a 16 channel polychromator by using 0.68 mm thick lucite light guides to feed light from the exit slit to the sixteen photomultiplier tubes (Fig. 21). The 16 light guides are bonded together with epoxy and mounted in an Al fitting. The ends are polished to increase the transmission efficiency. The thickness of each fiber at the fitting, closest to the exit slit is ~ 0.24 mm. A cylindrical lens serves to magnify the exit slit. The thickness of the image of each fiber at the exit slit is ~ 0.027 mm. With an instrumental dispersion of 11 Å/mm, the channel separation is given by

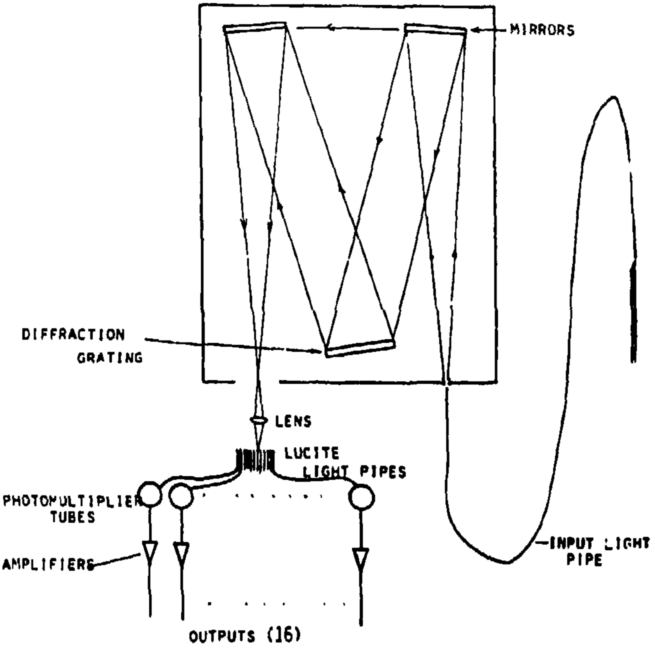

XBL 704-4145

Fig. 21. Schematic of the 16 channel polychromator.

11 Å/mm (0.027 mm) ~ .3 Å

The grating has 1200 lines/mm, is ~ 4 inches square, and is blazed to 5000 Å in first order.

The light is collected by means of a plastic Crofon light guide, 2 m in length and 1/8 inch diameter, which is positioned at various places around the vessel. At the entrance slit, the individual fibers, 10 mils in diameter, are aligned in the shape of the curved slit, epoxied in place, and polished. This arrangement ensures that the grating receives the maximum amount of light. The entrance slit used in this arrangement is 25μ wide. The other end of the light guide is mounted in a 1/4 inch diameter Al tube, epoxied in place, and the ends polished. This is done so that the guide may be placed in the interferometer holes, which are drilled in the fiber glass surrounding the glass vessels of both T IV-c and T V. The spectral transmittance of these fibers is approximately flat for wavelengths > 5000 Å and falls sharply for λ < 4300 Å.

Sixteen RCA 1P28A photomultiplier tubes are used and have a spectral response which peaks at 3500 Å, and falls sharply for wavelengths > 5500 Å and < 3000 Å. For wavelengths between 4000 Å and 5000 Å the response is good. The outputs of these tubes are fed into 16 operational amplifiers (National 531) and emitter followers, which are mounted in the polychromator housing. The gains are adjustable from 10^4 to 10^6 V/A, and the frequency response is better than 1 MHz.

Calibration of the polychromator is done in several ways. The 4765 Å line of an Ar-ion laser is swept across the 16 channels, and the profile of each channel is recorded. This gives the channel separation (~ 0.3 Å), the instrumental broadening (a Gaussian of ~ 0.6 Å full width at half maximum), and the relative sensitivities of each channel. This procedure is also done using the 5461 Å line from a low pressure Hg lamp. The channel separation and instrument broadening are not expected and are not found to change in time. The sensitivities are, however, variable, even though the polychromator is run at constant temperature using a heater, thermostat, and 2 inch thick styrofoam covering the entire instrument.

The sensitivities of the 16 channels are calibrated often using a high pressure Xe arc (solar simulator), which has an intensity vs. wavelength that is essentially flat at the optical wavelengths of interest. If light of a specific wavelength is to be measured, the polychromator is set at that wavelength. Light from the Xe arc is then taken in exactly the same way as the experimental data - through the data acquisition system and into the computer. Many shots are averaged together to eliminate photon noise. The wavelength setting is then moved to a nearby wavelength, and the procedure is repeated. This is done to ensure that the Xe arc spectrum is indeed flat at this wavelength. The relative sensitivities are stored in the computer and used to calibrate the spectral data after each machine shot.

In addition to this polychromator, a uv polychromator is used to look at both HeII 3203Å and various impurity lines. This polychromator is a 1/2 m Czerny-Turner type, Jarell-Ash spectrometer, converted to a 16 channel polychromator by using uv transmitting optical fibers to feed the light to the 15 RCA 4840 and one RCA 1P28A photomultiplier tubes. These tubes have the same spectral response, and are very good for wavelengths > 3000 Å. The output amplifiers are the same as for the above described polychromator. No light pipe is used. Instead, quartz lenses are used to guide the light into the 25 μ entrance slit.

Calibration is done using the 3341 Å line from a low pressure Hg lamp. Channel separation is ~ 0.4 Å and the instrumental broadening is ~ 1.7 Å. The grating is 5 cm square, having 600 lines/mm, and is blazed to 2000 Å.

(4) Thomson Scattering: Thomson scattering is a technique for measuring the electron temperature.[41,42,43] Intense laser light is scattered by fluctuations in the electron density, and collected here at 90°. Since the electrons are in motion, the collected light will be Doppler shifted. In this way, information on the electron velocity distribution function and, therefore, on the electron temperature, can be obtained. This measurement has been described in great detail in Ref. 34 and will only be summarized here.

For the measurement in Tormac, a ruby laser pulse, $\lambda = 6943Å$, energy ~ 2 Joules, length ~ 50 nsec, enters the device at one of three possible major radii travelling axially, and is focused to a 2 mm width at the axial center of the chamber (Fig. 22). The scattered light exits through the radial port and enters a 5 channel polychromator. Since Tormac does not have a good viewing dump, the

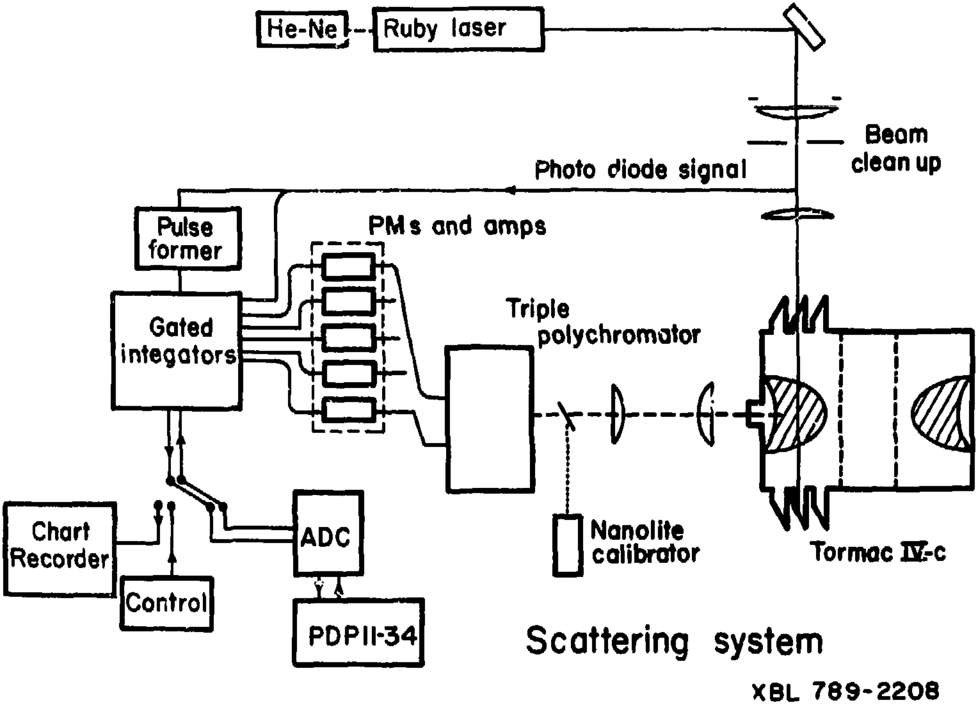

Fig. 22. Schematic of the Thomson scattering system.

polychromator was built so that stray light was reduced. This was done by building a 3 stage polychromator based on the varoilluminator.[34,44,45] Three identical gratings, 1200 lines/mm, 2 inch square, were used in conjunction with 3 stops so that light at the laser frequency was discriminated against. In this way, a net rejection of 10^9-10^{12} is achieved. Light guides are used to lead the light from the exit slit to five RCA 4836 photomultiplier tubes. Signals are displayed on Tektronix 585 oscilloscopes.

For the Tormac plasma parameters, the scattering is expected to be incoherent. This means that the scattering is off fluctuations in the density of the bare electrons and is not affected by collective plasma effects. This is expressed quantitatively by the parameter α, defined as

$$\alpha = \frac{1}{|\underline{\Delta k}|\lambda_D} ,$$

where λ_D = Debye length of the plasma, and

$$|\underline{\Delta k}| = |\underline{k}_0 - \underline{k}_s| = 2\, k_0 \sin \theta/2,$$

where $\underline{k}_0$ = incident wave vector, $\underline{k}_s$ = scattered wave vector, and θ = scattering angle. Since there are no correlations on scales smaller than the Debye length, incoherent scattering is given by

$$\alpha = \frac{\lambda_0}{4\pi \lambda_D \sin \theta/2} < 1 \quad .$$

For Tormac, $\alpha \sim 0.3$

The scattered light is Doppler shifted according to the formula[38]

$$\Delta\omega = \underline{\Delta k} \cdot \underline{v}$$

So, for a Maxwellian and the parameters in this experiment,

$$s(\Delta\lambda) = \text{scattered spectrum} = \frac{N_e}{\sqrt{T_e}} \exp\left[-\left(\frac{\Delta\lambda}{19.46}\right)^2 \frac{1}{T_e}\right]$$

where $\Delta\lambda$ is in Å and T_e is in eV.

(5) Flux loop: The flux loop consists of a single turn of insulated wire wrapped around the vessel inside the coils in the poloidal plane. The voltage out is proportional to the change in toroidal flux:

$$V = \frac{1}{c} \frac{\partial}{\partial t} \int \underline{B} \cdot \underline{dA} \; .$$

Therefore,

$$V = 10^{-8} \frac{d\phi_T}{dt} \; ,$$

where V is in volts and ϕ_T is the toroidal flux through the loop in Gauss. A passive integrator of 1 msec is used, giving

$$V = 10^{-5} \phi_T \quad .$$

Measurement with and without plasma gives the overall β of the plasma.

(6) Rogowski Coils: These coils are used to measure currents. Similar to magnetic probes, these coils respond to a change in the magnetic field due to the current to be measured.

$$V = 10^{-8} \, Na \, \frac{\partial B}{\partial t} \, ,$$

when V is the voltage out in volts, N is the total number of turns, and a is the area of each turn.

The coils are put around the current to be measured, and therefore, $B = \frac{I}{5r}$. This gives

$$V = 1.26 \times 10^{-8} \, na \, \frac{dI}{dt} \, ,$$

where n = number of turns/length.

A passive integrator is used to give the current directly. In this way the cusp, preionize, and bias circuit currents are measured and monitored at each machine shot. In addition, a Rogowski coil is wound around the vessel in the same way as the flux loop, and measures the net toroidal plasma current. It should be noted that these Rogowski coils are backwound, so that they will measure the current and are insensitive to a change in the flux through the middle of the coil.[46]

D. Diagnostics - T V

The diagnostics used on T V are essentially the same as those used on T IV. Only the differences will be discussed.

(1) Magnetic Probes: The uses of these probes and calibration procedures are the same as described for T IV. The probes themselves are different. Each probe consists of two 20 turn coils of #37 wire, 3 mm in diameter and 2 cm apart, encased in a 5 mm diameter quartz tube. The total inductance of these coils is 3 μH and are good to frequencies $\lesssim$10 MHz.

(2) He-Ne Interferometer: The T V interferometer arrangement is exactly the same as on T IV, except that it is larger so that it can fit around the larger vessel. There are 8 holes drilled in the plastic surrounding the vessel. They are located at the following major radii: 1) 18.9 cm, 2) 20.7 cm, 3) 23.3 cm, 4) 27.9 cm, 5) 30.4 cm, 6) 33.1 cm, 7) 42.0 cm, and 8) 47.5 cm.

(3) Spectroscopy: The hardware and procedures are the same as described for T IV.

(4) Thomson Scattering: A similar setup is used on T V as on T IV. A Spacerays ruby laser is used, instead of an Apollo laser, as used on T IV.

(5) Flux Loop: This is not routinely used on T V as it is on T IV. Flux loops measurements were done at an earlier time, and the loop itself was taken off when some modifications were made in the windings.

(6) Rogowski Coils: The same procedures are followed here as in T IV.

(7) Langmuir Probe: A double Langmuir probe is used in T V to measure fluctuating electric fields. It consists of two 10 mil tungsten wires imbedded in 28.5 cm long, 7 mm diameter quartz tube. The wires extend 5 mm out of the quartz, and are 3 mm apart. The wires inside the tube are kept apart by a ceramic insulator - a cylindrical rod having 2 holes drilled lengthwise which fits inside the quartz tube. In addition, a copper tube is inserted between the quartz and the ceramic cylinder, and extends over the entire length of the quartz. This is used for shielding purposes.

Each wire is connected to the center conductor of a small diameter coax cable. The cable, RG174, is 1 foot in length. The characteristic impedence of this cable is 50Ω, and its capacitance is ~ 30 pf/ft. The outer conductor of the cable is attached to the copper. Additional cable is added to this in order to lead the signal out of the high voltage screen cage.

To measure the signals, 2 high voltage probes are used. They are Tektronix P-6015, 1000x high voltage probes. These are necessary since the Langmuir probe is floating to a potential of ~ 1.5 kV with respect to ground. Also, to get an accurate measurement of the electric field of the plasma, the probe must have a high impedence; i.e., the impedence of the probe plus measuring apparatus must be high with respect to the plasma source impedence. The impedence of the high voltage probes is 100 MΩ, and is high compared to the source impedence. The frequency response of these high voltage probes is better than 30 MHz.

These signals are then put into a Tektronix 555 oscilloscope with a 1A1 plug-in. The 1A1 plug-in is used since it is good to ~ 30 MHz, and because it can subtract the 2 input signals directly. This subtraction is necessary to get the electric field from the 2 potential measurements. The common-mode rejection of the 1A1 is excellent (1000:1) out to ~ 30 MHz.

In addition to photographing the signal on the oscilloscope, the signal is put into the data acquisition system and sampled at 2 MHz. The digitized signal is stored in the computer. A fast Fourier transform is run to determine the frequency spectrum. It was found necessary to increase the sampling rate in order to increase the resolution. Since the data acquisition system could not sample faster than 2 MHz, this is done by feeding the signal into a delay box, which produces four signals, spaced 125 nsec apart. These four signals are fed into the data acquisition system and sampled simultaneously at 2 MHz. In this way, the sampling frequency was increased 8 MHz.

The high voltage probes are individually adjusted. A 70 V square wave generator is used to provide an input to these probes, and they are adjusted to reproduce the signal exactly. The same generator is then connected to both probes simultaneously, and the 1A1 is adjusted to give a null signal.

The double probe is inserted into the vacuum vessel through a compression fitting. The port used is the Thomson scattering beam dump at R = 33 cm. A model for the probe plus plasma is presented in Fig. 23. V_1 and V_2 represent the floating potential plus a small voltage due to electric fields; if there are no electric fields,

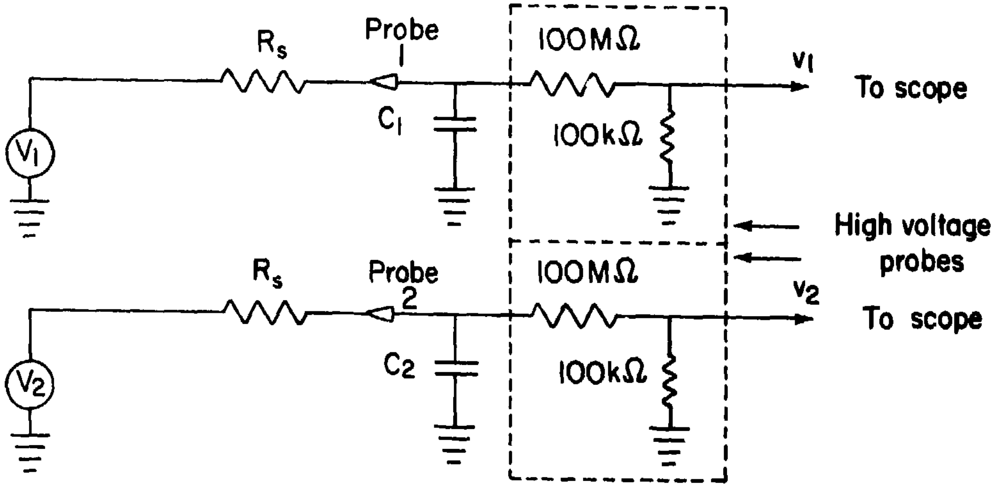

XBL 804-4148

Fig. 23. Model of the double Langmuir probe plus plasma.

$$V_1 = V_2 = V_{floating} \; .$$

With electric fields,

$$\frac{V_1 - V_2}{d} = E,$$

where d is the distance between the probe tips, and E is the electric field. R_s is the source impedence of the plasma seen by probes 1 and 2, and is given by[47]

$$R_s = \frac{kT_e}{ne^2 A} \left[\frac{2\pi \, m_i}{kT^*}\right]^{1/2} ,$$

where A is the collecting area of the probe, and

$$T^* = \begin{cases} T_i & \text{if } \; T_i > T_e \\ T_e & \text{if } \; T_e > T_i \end{cases} .$$

For the Tormac plasma parameters, $R_s < 1\Omega$. C_1 and C_2 represent the cable capacitances, which are ~ 120 pf for 4 ft. of cable. If C_1 is small, then

$$v_1 = \frac{V_1 \; (100 \; k\Omega)}{R_s + 100 \; M + 100 \; k\Omega} = \frac{V_1}{1000} ,$$

since $R_s \ll 100 \; M\Omega$. Similarly,

$$v_2 = \frac{V_2}{1000} \quad .$$

To ensure accurate reproduction of $V_1(t)$ and $V_2(t)$, the condition

$$\frac{1}{\omega} \gg R_s C$$

must be met,[48] which implies that the probe is good up to at least 10^9 Hz. The signals v_1 and v_2 go to the scope, which displays

$$v_1 - v_2 = \frac{V_1 - V_2}{1000} = \frac{Ed}{1000}$$

Therefore,

$$E = 3333\ (v_1 - v_2)\frac{\text{volts}}{\text{cm}} \quad .$$

E. Data Acquisition System on T IV and T V

The Tormac data acquisition system is discussed in detail in Ref. 35, and will be summarized here. For measurements of signals to time accuracies < 1 μsec, Tektronix oscilloscopes are used. In particular, magnetic and electric probe data and Thomson scattering data are collected using oscilloscopes. For spectroscopy, flux loops and Rogowski loop current monitors, a fast digitizing circuit[49] is used to take 128 time samples of each signal in 0.5 μsec steps. Up to 24 channels are routinely used, with sampling speeds of ~ 2 MHz. The data are stored simultaneously in serial analog memories during each machine shot. After the shot is over, the analog data go to an ADC, and then through cables to a PDP-11/34 computer located in the same room as the experiment. The computer displays the data, allows analysis (for example, spectral lines may be fit with a Gaussian or a Lorentzian), and stores them for future use.

The serial analog memories, ADC, and all controlling circuitry are located in heavily shielded boxes, one for each experiment. The computer is common to both experiments. The system was checked to ensure that the output to the computer varied linearly with input voltage. It was found that it was linear up to 2 V input. The input signals were then arranged to be $\lesssim 2$ V.

III. EXPERIMENTAL DATA

A. T IV-c

(1) Rogowski Coils: Figure 24 shows the current in the bias, preionization, and cusp banks as functions of time. Each trace is taken with only that particular bank discharging, and shows the expected damped sinusoid. Knowing the capacitance, the inductance and resistance of each circuit may be calculated. The bias trace has only one peak before the ignitron switch becomes non-conducting. None of these banks were crowbarred in these shots. Note that in each picture, the triggering time and sweep speed were adjusted to yield the entire signal, and that some banks are not charged to their normal operating voltages.

Figure 25 shows the cusp and preionize currents as functions of time, each bank firing at its normal time. The bias bank current is peaked at this time, and remains essentially constant.

It should be mentioned that these banks are not independent in that they couple to each other. For example, Fig. 26 shows the bias Rogowski signal as a function of time. At the time of peak current, the cusp bank discharges, and its effect on the bias current is evident. Note that here the cusp bank is charged to 8 kV, instead of its normal 15 kV. Coupling of the cusp bank to the preionization bank is not as severe as to the bias bank, though it exists.

With plasma present, the signals are altered. The effect is an increased damping of the current. No change in bank coupling is seen.

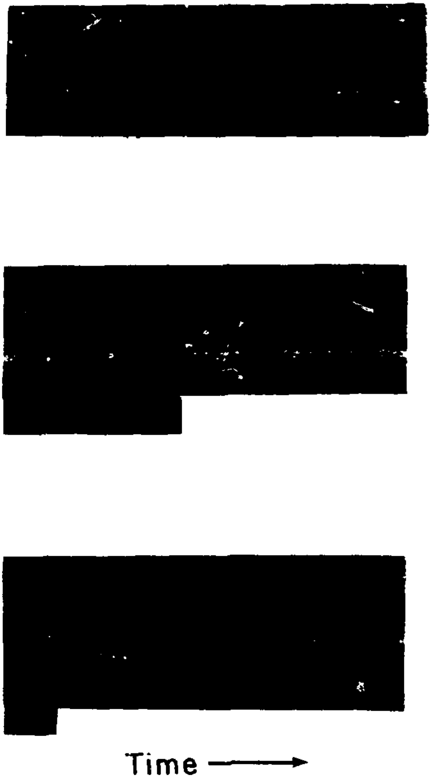

Bias Rogowski
100 μsec/div.
Bank charged
to 1kV

Preionize Rogowski
20 μsec/div.
Bank charged
to 22.5 kV

Cusp Rogowski
50 μsec/div.
Bank charged
to 4kV

XBB 804-5084

Fig. 24. Coil currents in the various T IV banks, measured with Rogowski coils.

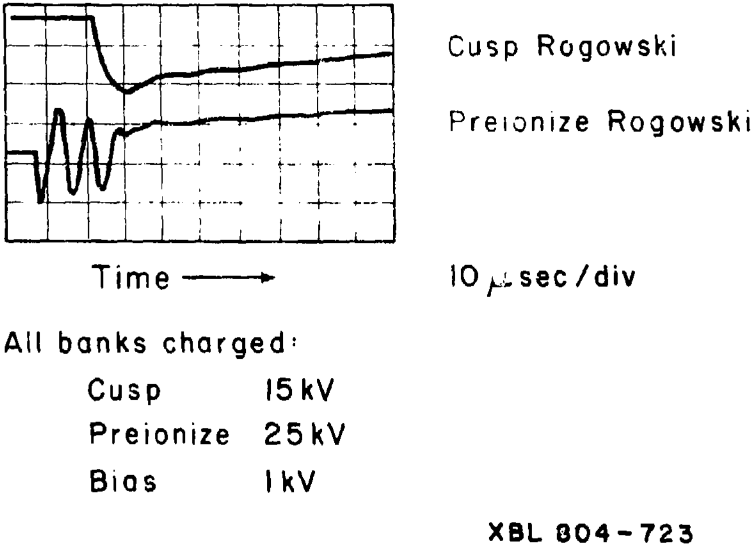

Fig. 25. T IV cusp and preionize currents vs time.

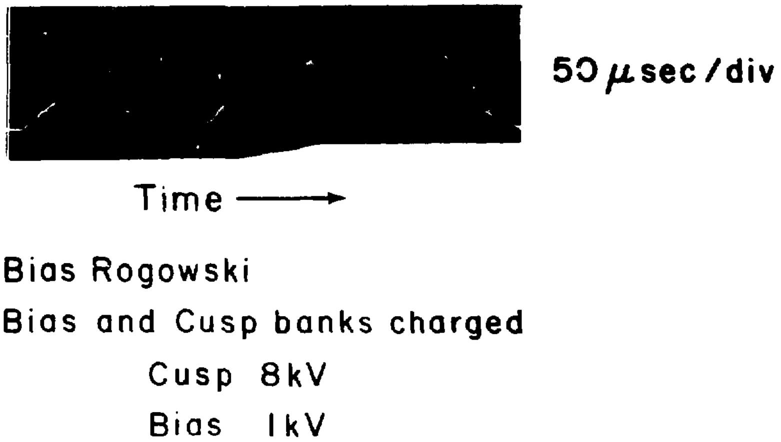

XBC 804-5083

Fig. 26. Current in the 1 kV bias circuit showing coupling with the cusp circuit.

(2) Plasma Current Rogowski: Figure 27 shows the typical variation of the toroidal plasma current in time. The very high frequency variation late in time is due to the data acquisition system. The first evidence of plasma current occurs at the second peak of the preionize circuit current, and is driven in phase at the preionization bank frequency. The discharge of the cusp bank drives a large toroidal plasma current, which remains throughout the rest of the experiment and dominates the preionize driven current. It was found that the magnitude of this current could be controlled to a certain extent by varying the crowbar time of the preionization bank. It was also shown by discharging the uncrowbarred preionization bank without the cusp that this bank freezes in a net toroidal current in the opposite direction as that driven by the cusp. By reversing the polarity of the preionization bank, these frozen in currents were made to add, giving a large net toroidal plasma current. Further, the plasma current is controlled by the magnitudes of the currents in the driving circuits. For example, the larger the cusp bank charging voltage, the larger the net plasma current. Therefore, by changing the crowbar time and polarity of the preionization bank, as well as the charging voltages of the preionization and cusp banks, the magnitude of the net toroidal plasma current could be controlled. The bias bank has no effect on plasma current.

(3) Magnetic Probes: Figure 28 shows the time evolution of the vacuum toroidal magnetic field at R = 18 cm at the axial center of the device due to the bias and cusp banks charged to their normal operating

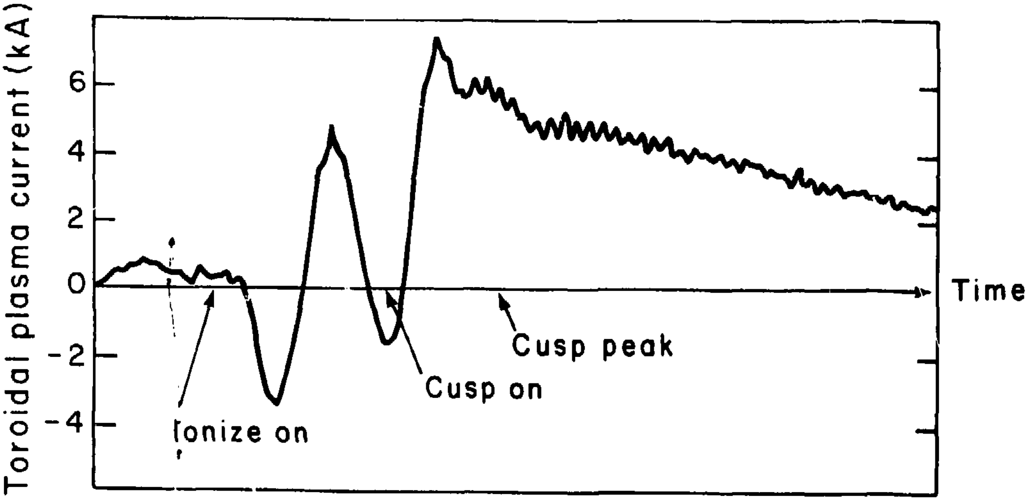

XBL 804-732

Fig. 27. Toroidal plasma current vs time in T IV.

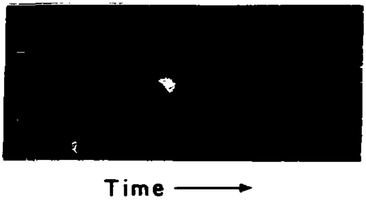

Vacuum $B_{toroidal}$
Axial Center at R = 18 cm
10 μsec/div
1160 Gauss/div

Bias and cusp banks charged
Cusp 15 kV
Bias 1 kV

XBB 804-5079

Fig. 28. Vacuum $B_{toroidal}$ vs time in T IV.

voltages. No effect due to preionization field is seen, as expected. Note that the initial offset is due to the bias field, which at this time is at its peak and essentially constant.

Figure 29 shows the variation of the peak vacuum toroidal magnetic field as a function of R at the axial center. The cusp and bias are charged to their normal voltages. The solid line is a $\frac{1}{R}$ fit to the data, assuming a total axial current of 243 kA, and shows that the data exhibit the expected $\frac{1}{R}$ variation.

The vacuum axial magnetic field as a function of R at the axial center of the device has very different behavior than the toroidal field. This field consists of contributions from the preionize and cusp fields. It is found that the preionize field dominates at small major radius, and the cusp field dominates at large major radius; the preionize field remains approximately constant in R, while the cusp field increases as R increases - in the direction of the poloidal coils. Figure 30 shows the typical B_z field variation at R = 16.8 cm at axial center. Figure 31 shows the R variation of the vacuum B_z field at the axial center of the device. Note that there is some current in the preionize coils after the bank is crowbarred, and this produces a B_z field opposite that is due to the cusp. This is a function of the preionize crowbar time.

The toroidal field in the presence of plasma exhibits interesting behavior. Figure 32 shows a typical $B_{toroidal}$ vs. time trace, taken at R = 13 cm with a 50 mTorr fill pressure of 80% H_2, 20% He. The corresponding vacuum shot is also shown. Strong oscillations having

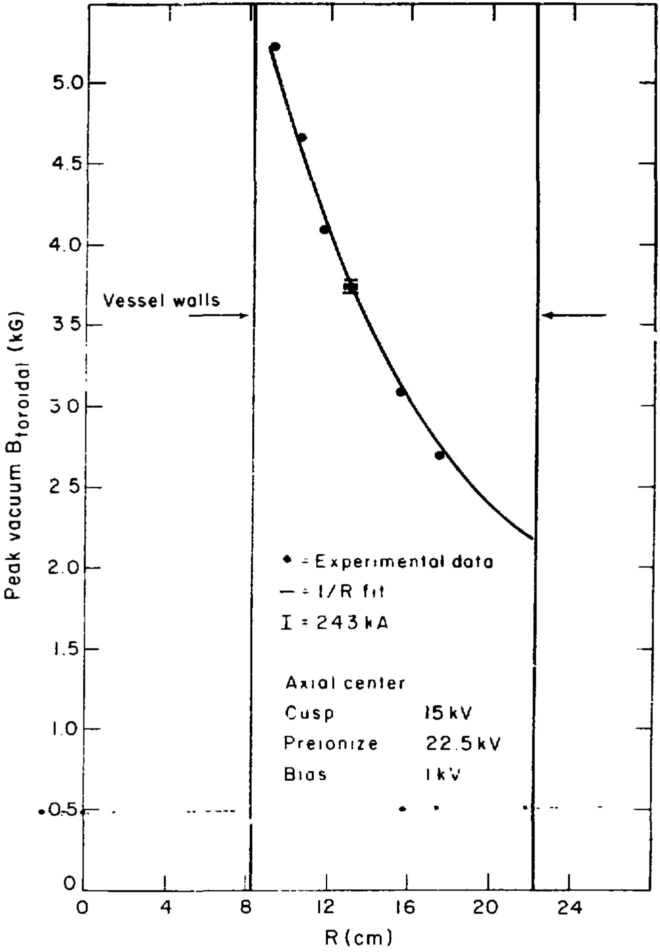

XBL 804-730

Fig. 29. Peak vacuum B_{toroidal} vs major radius in T IV.

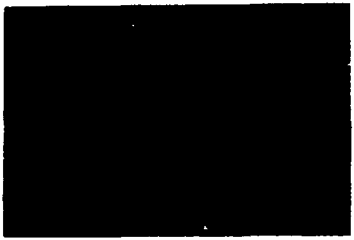

Vacuum B_Z
Axial Center at R = 16.8 cm
10 μsec/div
580 Gauss/div

All banks charged

Cusp	15 kV
Preionize	25 kV
Bias	1 kV

XBB 804-5680

Fig. 30. Vacuum B_Z vs time in T IV.

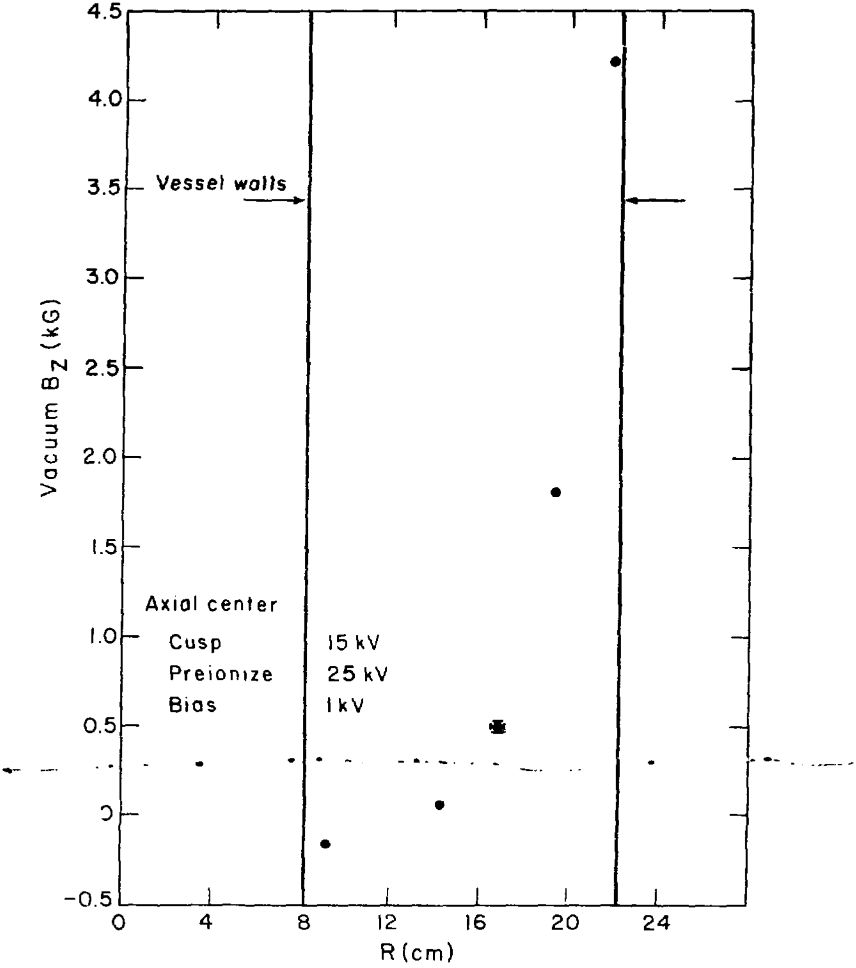

XBL 804-729

Fig. 31. Peak vacuum B_Z vs major radius in T IV.

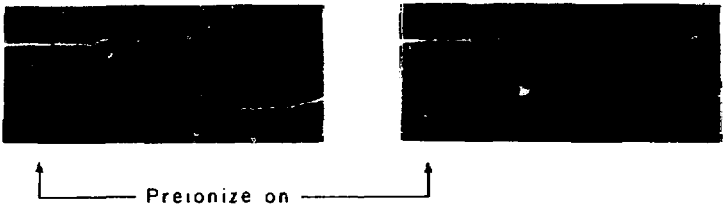

50 mTorr fill pressure

Vacuum

$B_{toroidal}$ vs Time

R = 13 cm at Axial Center

5 μsec/div	1160 Gauss/div
Cusp	15 kV
Preionize	22.5 kV
Bias	1 kV

XBB 804-5081

Fig. 32. $B_{toroidal}$ vs time with and without plasma in T IV. Strong oscillations are evident in the plasma case.

frequencies between 700 kHz and 1 MHz are evident. These exist during the cusp field use, and rapidly damp out after cusp peak. They appear at all major radii along the axial center of the device, and are strongest at R ~ 13 cm. The variation of $B_{toroidal}$ in time is repeatable, and the general shape of the curve does not depend on cusp bank changing voltage.

The variation of the oscillation frequency with fill pressure is illustrated in Fig. 33. This is taken at R = 13 cm at the axial center of the device. All banks are at their normal operating voltages. There is much scatter, though there does appear to be a decrease in frequency with pressure after 10 mTorr.

Evident from Fig. 32 is that there is exclusion of the toroidal magnetic field. The exclusion time ranges from 0.6 to 2.5 μsec, as shown in Fig. 34. The bars show the shot to shot spread at the various major radii. No penetration front can be seen from small to large major radius; an exclusion for ~ 1.8 μsec is observed, followed by an approximately simultaneous arrival of toroidal field for major radii < 13 cm. It is found that the toroidal field arrives at the larger major radius points first, although the toroidal field is strongest at small major radius. Also evident from Fig. 32 is that once the toroidal field arrives, it increases very quickly in time, just before the first oscillations occur. The initial $\frac{dB}{dt}$ is measured to be ~ 0.46 kG/μsec for the vacuum case, and ~ 1.8 kG/μsec for a 50 mTorr plasma case.

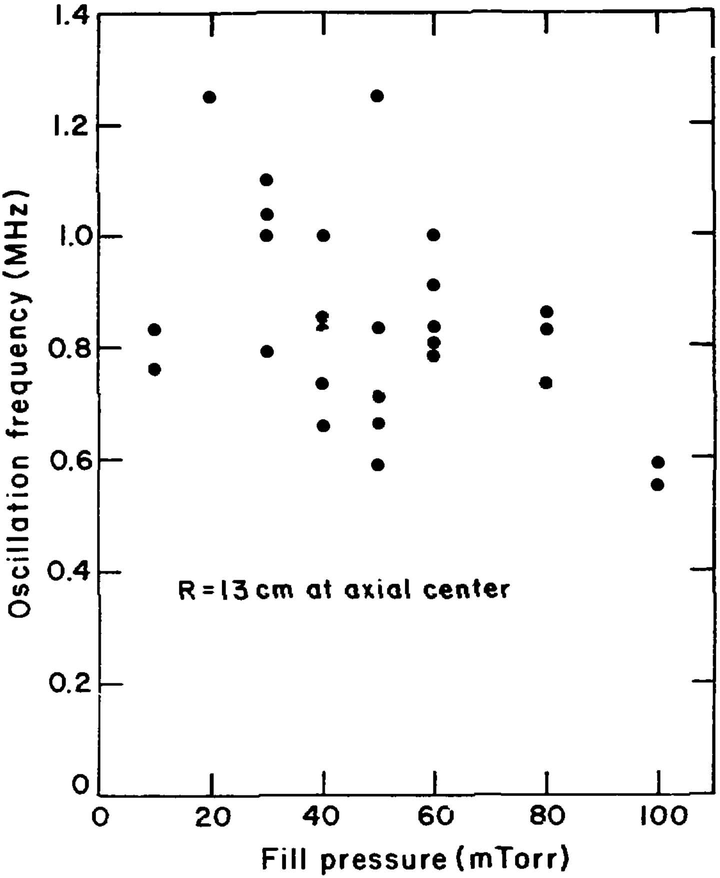

XBL 804-718

Fig. 33. $B_{toroidal}$ oscillation frequency vs fill pressure. Each point represents a separate T IV machine shot.

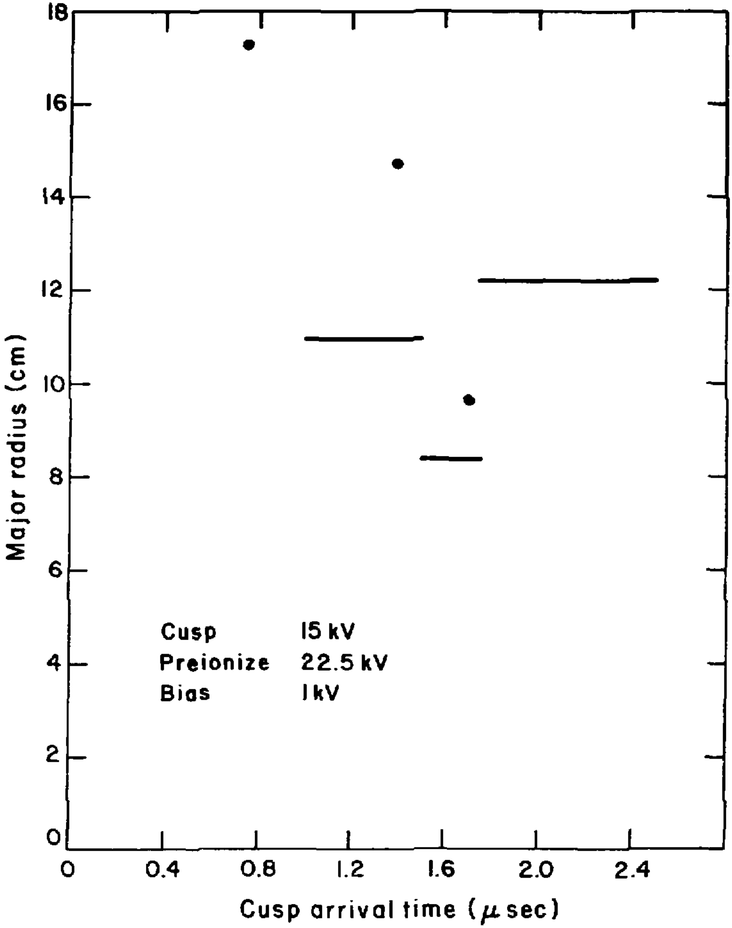

XBL 804-717

Fig. 34. Major radius vs cusp toroidal field arrival time for the parallel bias case in T IV.

Figure 32 also illustrates the typical behavior of the toroidal field before application of the cusp field. With plasma, there is an increase in the toroidal field due to compression of the bias field and plasma by the preionize field. When the bias is reversed, this increase in field also reverses. A small dip occurs before the larger one, and from their separation in time, a frequency of ~ 230 kHz is deduced. Compression by the preionization field would indeed occur at this frequency, which is twice the frequency of the bank.

A much different behavior of the toroidal field is observed when the bias field is reversed with respect to the cusp field. Figure 35 shows $B_{toroidal}$ vs. time at R = 13 cm at the axial center of the device, for normal bank operating voltages. Both a vacuum and a 50 mTorr plasma shot are shown. Oscillations are less obvious in this case. The field, which first increases due to the cusp, returns to its pre-cusp value before the cusp field finally penetrates. This behavior is much more variable than in the parallel bias case, and shots with oscillations similar to those observed in the parallel bias case are found here. Differences in the toroidal field behavior for the two bias cases are found when the cusp bank charging voltage is $\lesssim$15 kV. As this voltage is raised, the differences disappear, and at ~ 20 kV, the reversed bias shots look the same as the parallel bias shots.

The toroidal field is also excluded from the plasma in the reversed field case, as shown in Fig. 36. The bars illustrate the shot to shot spread. A penetration front is evident as the toroidal

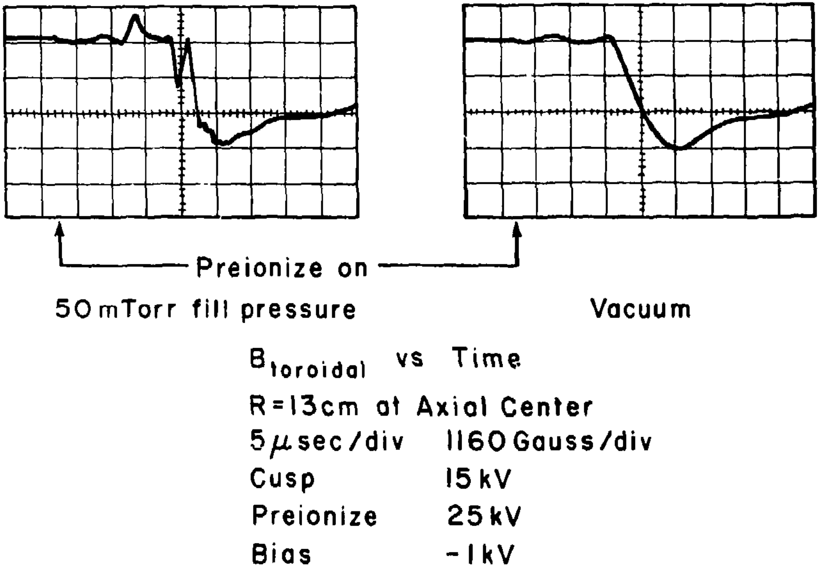

Fig. 35. $B_{toroidal}$ vs time with and without plasma in T IV for the reversed bias case.

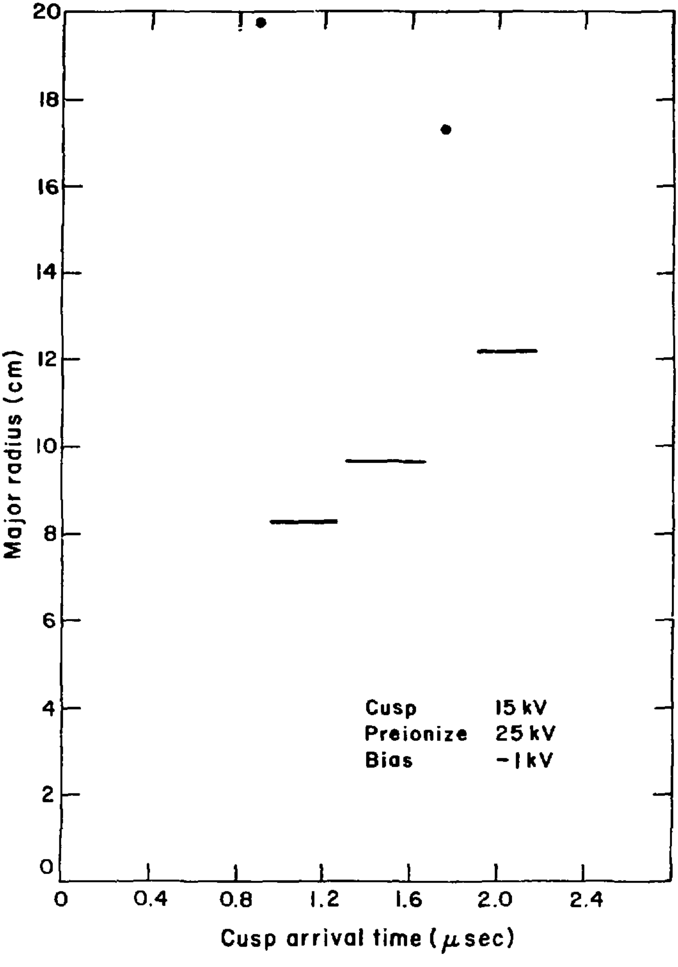

Fig. 36. Major radius vs cusp toroidal field arrival time for the reversed bias case in T IV.

magnetic field due to the cusp moves into the plasma from small major radius. The velocity of penetration is 3-6 cm/μsec. As in the parallel bias case, the rate of rise of the toroidal field is larger in the plasma than in vacuum shot.

The behavior in time of the Z-component of the poloidal magnetic field at R = 9.2 cm at the axial center of the device is shown in Fig. 37. Both a 50 mTorr fill pressure case and a vacuum case are shown for normal operating conditions. Both the plasma and vacuum shots are identical during the first half cycle of the preionize, indicating that the plasma does not break down until the second half cycle in agreement with the plasma current Rogowski. When the plasma does break down, the poloidal field is shielded out of the plasma for R < 18 cm; i.e., the field no longer follows the vacuum field oscillation. For R > 18 cm, the field with plasma present oscillates as in the vacuum case, which indicates less complete shielding. This implies that the plasma current, measured with the Rogowski coil, must be located at R < 18 cm.

Two glitches, or regions of large $\frac{dB}{dt}$, are evident in these data, one associated with the preionize, and one with the cusp. The arrival time of these glitches changes with major radius, as illustrated in Fig. 38. The penetration velocity of the poloidal field is ~ 2 cm/μsec.

The poloidal field at R = 12 cm as a function of Z was observed in order to ascertain where the toroidal plasma current is located. It is

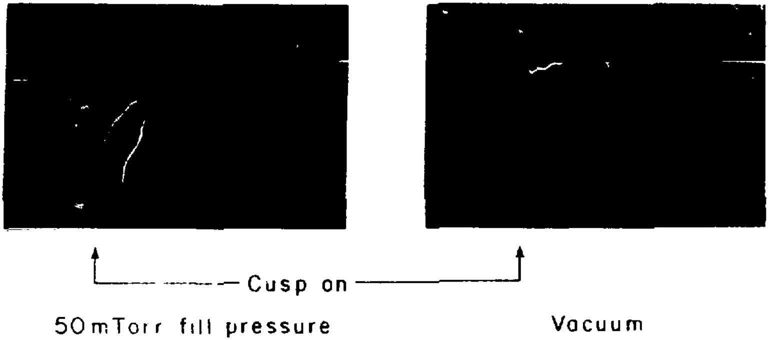

B_Z vs Time

R = 9.2 cm at Axial Center

10 μsec/div 580 Gauss/div

Cusp 15 kV

Preionize 25 kV

Bias 1 kV

Fig. 37. B_z vs time with and without plasma in T I..

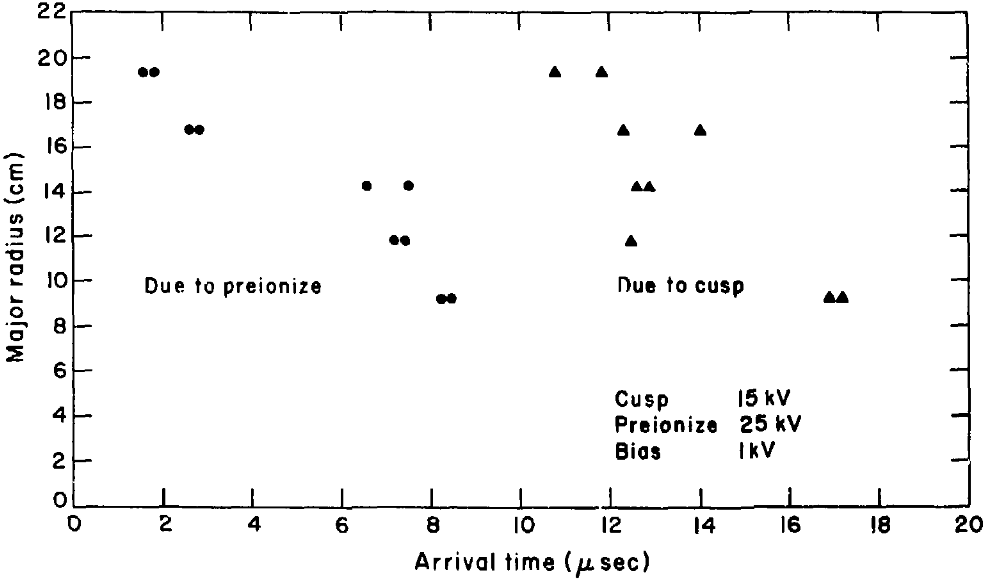

XBL 804-715

Fig. 38. Major radius vs arrival times of preionize and cusp related poloidal magnetic signals in T IV.

inferred that the current is spread out in Z for $R < 18$ cm, and dies away near the end walls in Z.

(4) <u>He-Ne Laser Interferometer</u>: Much work has been done in the past using the interferometer to diagnose the T IV-c plasma.[34,35] For the normal bank charging voltages, the preionization bank ionizes ~ 50% of the gas. This ionization starts near the center of the vessel and rapidly spreads out. The cusp field raises the level of ionization to ~ 90%. At no fill pressure is the gas totally ionized at these voltages.

As the cusp is applied, the density at small major radius increases, while the density at large major radius decreases. At cusp peak, the density profile is approximately flat from $R = 7.5$ to 17 cm. There is a decrease at larger major radius. The density compression quickly dies away after cusp peak. At $R \sim 14$ cm, the electron density is found to increase as the cusp charging voltage is increased, and as fill pressure is increased.

Oscillations in the density, similar to those found in the toroidal magnetic field, are found. Figure 39 shows a typical interferometer voltage out vs. time trace for a 50 mTorr fill pressure case and a vacuum case. These are taken at $R = 14$ cm for normal bank operating voltages. Oscillations are apparent during the cusp rise, and have a frequency of ~ 700 kHz. The line density vs. time is also shown. Oscillations are also apparent in the reversed bias case. It should be emphasized that these measurements are non-local, whereas the magnetic probe measurements are local.

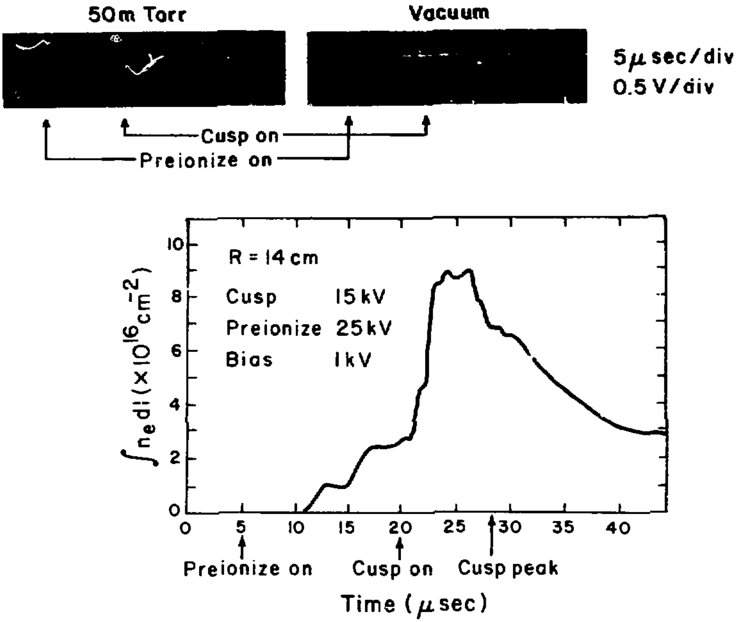

XBB 804-5078

Fig. 39. Top: Interferometer voltage out vs time with and without plasma in T IV.
Bottom: Line density vs time in T IV.

(5) Thomson Scattering: This was done on T IV-c by M. Greenwald and J. Coonrod.[34,35] The apparatus is capable of measuring electron temperature above ~ 4 eV. It is found that these temperatures are reached ~ 3 μsec before cusp peak, and that earlier $T_e < 4$ eV. Figure 40 shows the results of these measurements. A peak electron temperature of 5-6 eV is measured near cusp peak, and falls to below 4 eV in ~ 6 μsec. These results are not changed by raising cusp bank voltage or changing the gas mixture. There is no change in the temperature as fill pressure is varied, until very high pressures (~ 100 mTorr) are reached. At this point, the electron temperature remains below 4 eV.

(6) Spectroscopy:

HeII 4686 Å

Much work has been done in the Tormac project using HeII 4686 Å (see Appendix A) as an ion temperature diagnostic.[50-52] Broad, Gaussian lines indicating ion temperatures > 100 eV have been reported.[30,52] Figure 41 shows a line profile taken along a line of sight near the axial center of the device looking radially inward at a time 2 μsec before cusp peak. The full width at half maximum is 1.9 Å, and corresponds to an ion temperature of 110 eV. The solid curve is the best Gaussian fit, produced by a curve fitting routine which seeks the best Gaussian or Lorentzian fit to the data by varying the line center, amplitude, width, and continuum level of the fit, minimizing the error,

$$\mathrm{ERROR} = \sum^{16} [Y(i) - f(i)]^2,$$

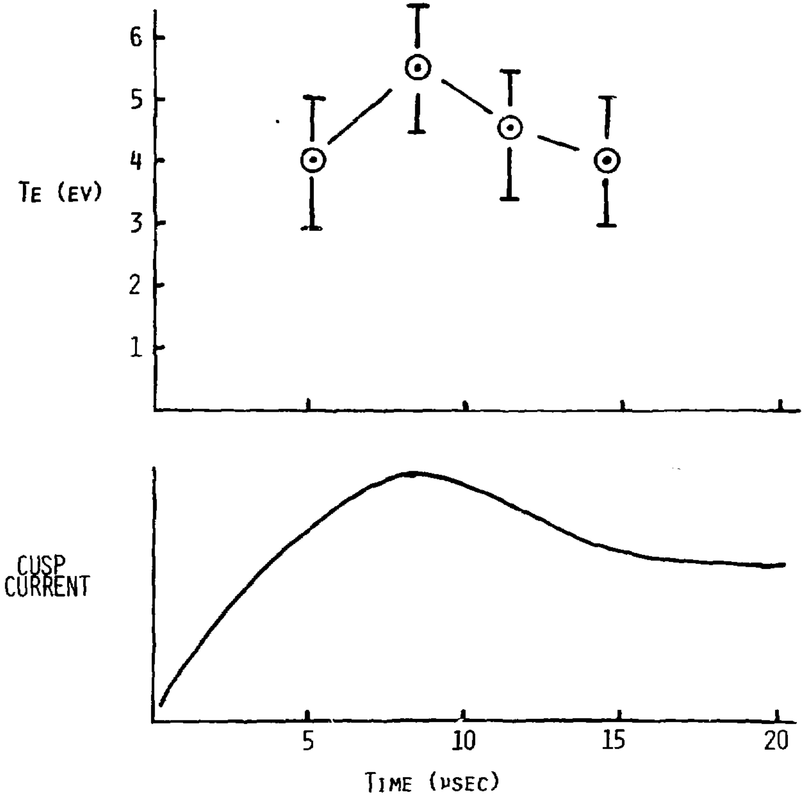

ELECTRON TEMPERATURE vs TIME

XBL 789-10851

Fig. 40

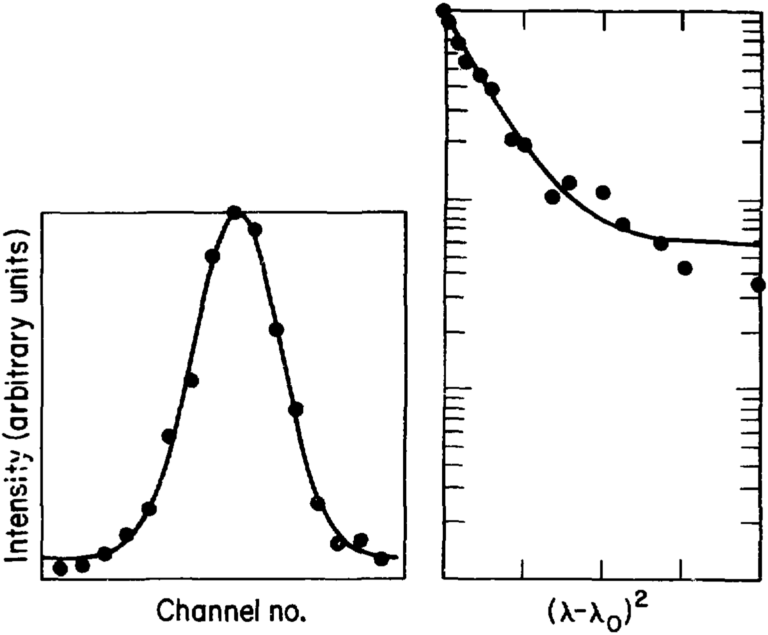

XBL 802-253

Fig. 41. HeII 4686Å line profile from T IV, on a linear (left) and logarithmic (right) scale. Data were taken along a line of sight near the axial center of the device looking radially inward at a time 2 μsec before cusp peak. The full width at half maximum is 1.9Å. Channel separation is 0.3Å.

where Y(i) is the measured intensity of channel i, f(i) is the value of channel i for the trial fit, and the sum is over the 16 spectral channels.[53] For this fit, a 6% continuum has been added, causing the log plot to bend away from the straight line expected for a Gaussian. Even though these data are from a single time step and a single machine shot, their Gaussian quality is striking.

Recent work has found somewhat smaller widths ($T \lesssim 100$ eV) than those found in the past. Previous data were taken with a highly collimated light pipe, using a lens and Al mirrors. It is found that at some line of sight positions, the more highly collimated the collection optics are, the broader the lines appear. This is presumably due to the fact that these are line of sight measurements, and the wider viewing angle allows light from the areas of the plasma having less broad lines to enter, and add to the center of the line. The result is a narrower line.

In general, photon noise causes the experimental data to deviate from the Gaussian fit. In spite of this, the Gaussian does provide the best fit to the data - a Lorentzian does not fit at all. Because the present light pipe optics are inferior to that used in the past in T IV, photon noise is a problem when a large degree of collimation is attempted. However, if a time average is performed, or if several machine shots are averaged, the Gaussian with continuum fits the experimental points extremely well.

Figure 42 shows a typical HeII 4686 Å line profile taken 2.5 μsec before cusp peak. This is from a line of sight at R = 14 cm looking axially. The data are from a five machine shot average, and appear quite noisy, since the light pipe is highly collimated, and the amount of light collected at each shot is small. The full width at half maximum is 2.2 Å, corresponding to an ion temperature of 140 eV. Figure 43 shows a line profile from the same line of sight as above, taken 13.5 μsec after cusp peak. The full width of half maximum is 1.19 Å and corresponds to 43 eV.

Figure 44 shows the typical variation in time of the inferred ion temperature for high cusp bank voltage. Note that peak temperatures occur before cusp peak. Two regimes of dT_i/dt are found:

$$1)\ \frac{dT_i}{dt} \sim -5.6\ \frac{eV}{\mu sec} \quad ,$$

starting about half way up the cusp rise, and

$$2)\ \frac{dT_i}{dt} \sim -1\ \frac{eV}{\mu sec} \quad ,$$

after cusp peak. The very high frequency variation is probably due to data taking system. These two regions are also evident at normal bank operating voltages, though more noise is present.

The widths of the HeII 4686 Å lines are changed by varying parameters. The following are found:

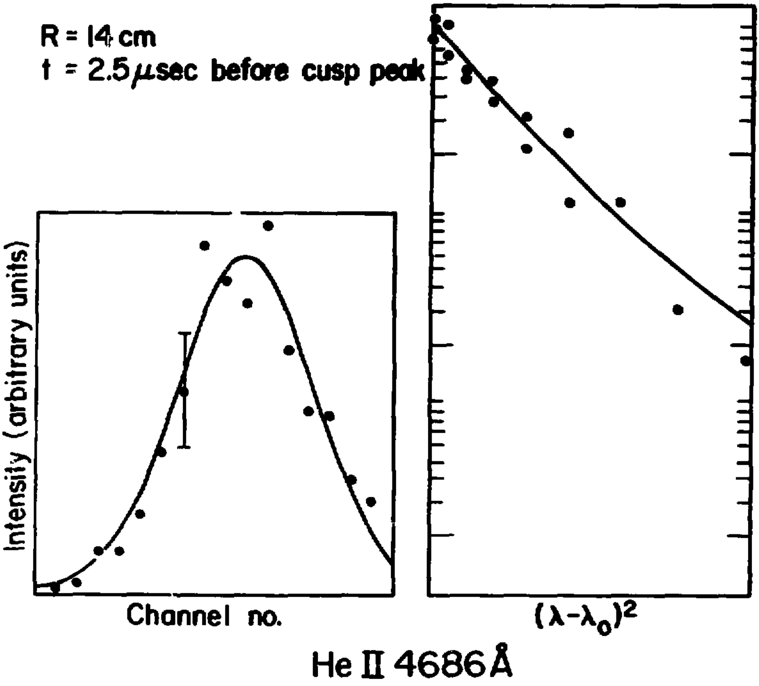

XBL 804-4142

Fig. 42. HeII 4686Å line profile from T IV, on a linear (left) and logarithmic (right) scale. Data were taken along a line of sight at R = 14 cm looking axially at a time 2.5 μsec before cusp peak. Channel separation is 0.3Å.

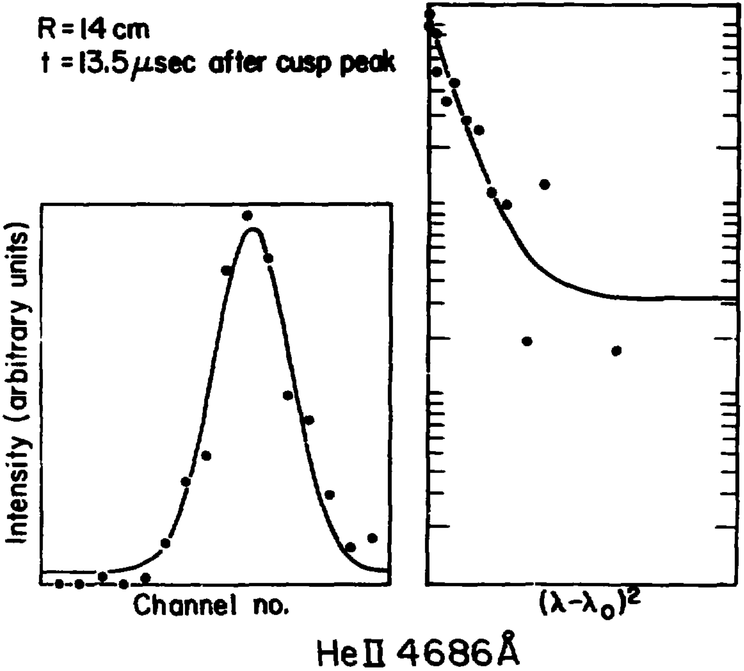

XBL 804 9143

Fig. 43. HeII 4686Å line profile from T IV, on a linear (left) and logarithmic (right) scale. Data were taken along a line of sight at R = 14 cm looking axially at a time 13.5 μsec after cusp peak. Channel separation is 0.3Å.

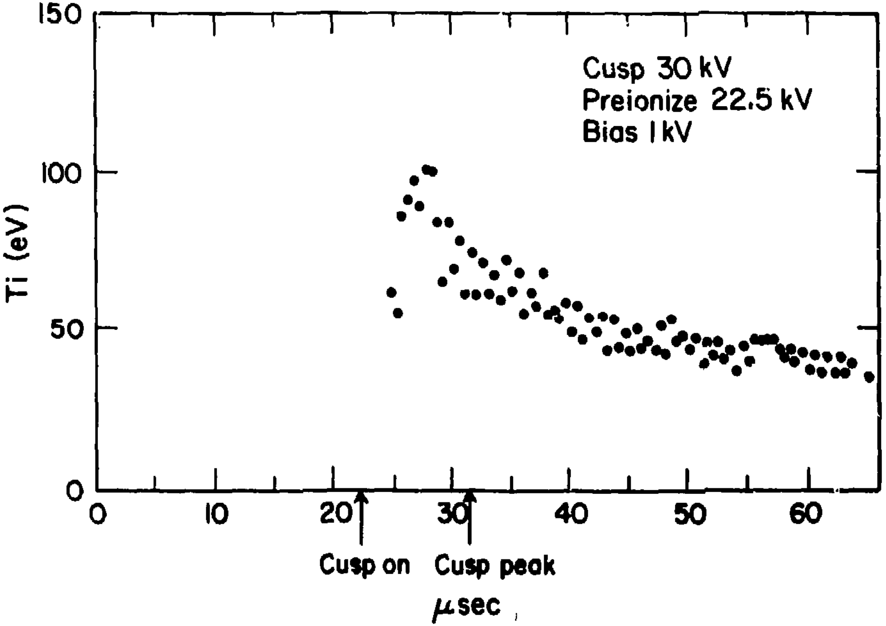

Inferred ion temperature vs time

Fig. 44.

XBL 804-4140

a) Widths increase with fill pressure from 10-50 mTorr; above 50 mTorr, the peak temperature increases slightly with pressure, and no change is seen after cusp peak.

b) No change in widths is seen as the timing of cusp discharge with respect to the preionize discharge is varied.

c) No change in widths is seen as the magnitude of the bias field is varied.

d) Widths increase as the cusp charging voltage is increased. This voltage increase also increases the net toroidal current.

e) Widths increase as the preionize charging voltage is increased. This voltage increase also increases the net toroidal current.

f) Peak temperatures are higher in the reversed bias case, though no change is seen after cusp peak.

g) Looking axially, the largest widths are found at R ~ 14 cm.

h) Little difference is seen when looking axially or radially.

The intensity of the emitted HeII 4686 Å light also changes as the various parameters are varied. The following are found:

a) As the fill pressure is increased, the light intensity decreases. Also, the duration of the intensity peak lengthens; at 20 mTorr, the intensity peak lasts ~ 3 μsec, and at 50 mTorr, it lasts ~ 7 μsec.

b) As the bias field is increased, the peak intensity decreases.

c) As the cusp field is increased, the peak intensity increases, and the duration of the intensity peak decreases.

d) As the preionize voltage is increased, the peak intensity increases, and the duration of the intensity peak decreases.

e) There is no change of the measured intensity as the polarization of the collected light is varied.

f) The intensity of the light is higher, and the duration of the intensity peak is smaller when the direction of the bias field is reversed.

g) The time of occurrence of peak intensity is the same for all major radii, viewing axially.

h) More light comes from large major radius than small major radius.

Hβ 4861 Å

Hβ has been looked at for a number of reasons. It is located within the good response region of the polychromator. Since the intensity behaves differently with temperature than HeII 4686 Å, information on the plasma temperature may be obtained. Hβ is very susceptible to the Stark effect, and information on the electron density may be obtained. In fact, in a plasma such as the Tormac plasma, the width of Hβ is expected to be determined solely by the density.

The problem with using Hβ is that it is burned out above a few eV. Since the measurement is line of sight, it is likely that Hβ originates from outside any compressed, hot plasma. It might come from a region entirely different than HeII 4686 Å.

Figure 45 shows Hβ profiles before, during, and after cusp rise, taken at R = 12 cm looking axially. The characteristic dip due to Stark splitting is sometimes visible and sometimes not. Lines have been found that are very Gaussian and others that are very Lorentzian. Because the Hβ profile is so dependent on the density, and the measurement is line of sight through regions of varying density, it is not surprizing that Hβ has such a wide variety of shapes. It should also be noted that the Doppler effect, thermal or due to mass motion, would tend to wash out the central dip.

Densities inferred from the widths of the lines agree roughly with those from the interferometer. The before cusp line in Fig. 45 has a full width at half maximum of 1.5 Å, which corresponds to a density of $6\text{x}10^{14}$ cm^{-3}. The post cusp peak line in Fig. 45 is hard to interpret in that it is so wide that the whole line could not be measured at once. Also, at this time the intensity is low. Nevertheless, it seems to have a width of ~ 3.5 Å, which corresponds to $2.3\text{x}10^{15}$ cm^{-3}. It is found that there is a large increase in line width as the fill pressure is increased, up to ~ 50 mTorr. Above this point there is not much change.

Observations in Tormac of satellites occuring on Hβ due to the presence of high frequency turbulence have been reported.[54-57] It is possible that the bumps seen on the wings of some lines are due to Langmuir turbulence, although the data at these times are noisy since the intensity is low. However, if the bumps seen on the wings of the after cusp peak spectral line shown in Fig. 45 are interpreted as

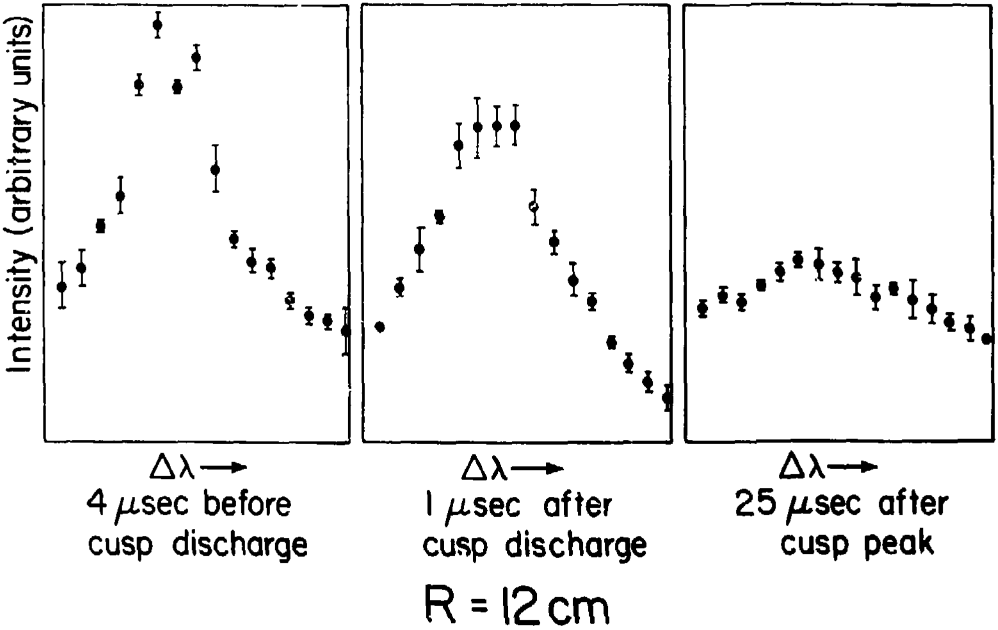

4 μsec before cusp discharge

1 μsec after cusp discharge

25 μsec after cusp peak

XBL 804-4141

Fig. 45. Hβ 4861Å line profile at three different times during the T IV discharge from a line of sight at R = 12 cm looking axially. Channel separation is 0.3Å.

satellites due to turbulence at frequency ~ ω_p, then the density inferred from the satellites location with respect to the line center is in reasonable agreement with both the Stark broadening inferred density and density from the interferometer.

Hβ is found to have the widest lines and the most intensity near the inner wall. Oscillation of the intensity in time with a frequency twice that of the preionizer is found. This oscillation becomes stronger at large major radius.

As the cusp nears its peak, the widths of both HeII 4686 Å and Hβ 4861 Å decreases. It should be pointed out that at this time, Hβ has what appears to be a fairly narrow line, ~ 1 Å, superimposed on a large continuum level. This might be interpreted as cold, low density material superimposed on high density material. Since the measurement is line of sight, it is hard to tell exactly how to interpret the line width. Nevertheless, the intensity is decreasing, and the width of the narrow line is less than the width of He II 4686 Å at the same time. No central dip is present.

Impurities

A number of impurity elements were looked for. Since the emitted light had to be in the range between light pipe cut off and photomultiplier tube cut off, only a few lines were considered. NII 4793.5 Å and CI 5380 Å were not found. Both OII 4705 Å and OII 4699 Å were found. OII 4705 Å is brighter, and will be considered here.

Figure 46 shows the OII 4705 Å lineshape from a line of sight at R = 14 cm looking axially. This is taken 4 μsec before cusp peak, and the solid line is a Gaussian fit with 28% continuum added. Though much less intense than HeII 4686 Å, the lineshapes are very similar. The full width at half maximum is 1.13 Å.

Figure 47 shows the linewidth vs. time. Again, there is a rapid decrease before cusp peak. The widest lines occur about half way up cusp rise - at the same time as HeII 4686 Å. The intensity peak also occurs at the same time as the intensity peak of HeII 4686 Å; i.e., about half way up the cusp rise.

HeI 4922 Å

This line is of interest, since it has a nearby forbidden component at 4920.59 Å. Enhanced emission occurs at the position of the forbidden component when electric fields are present, such as due to non-thermal turbulence. If these electric fields have oscillation frequency Ω, then satellites appear symmetrically about the position of the forbidden component, separated by

$$\Delta\lambda = \frac{\lambda_f^{\,2}}{2\pi c}\,\Omega$$

from the forbidden line, where λ_f is wavelength of the forbidden line, Ω is the oscillation frequency, and c is the speed of light. These satellites are broadened by the usual broadening mechanisms, and are spread out if the turbulent electric field is not monochromatic.

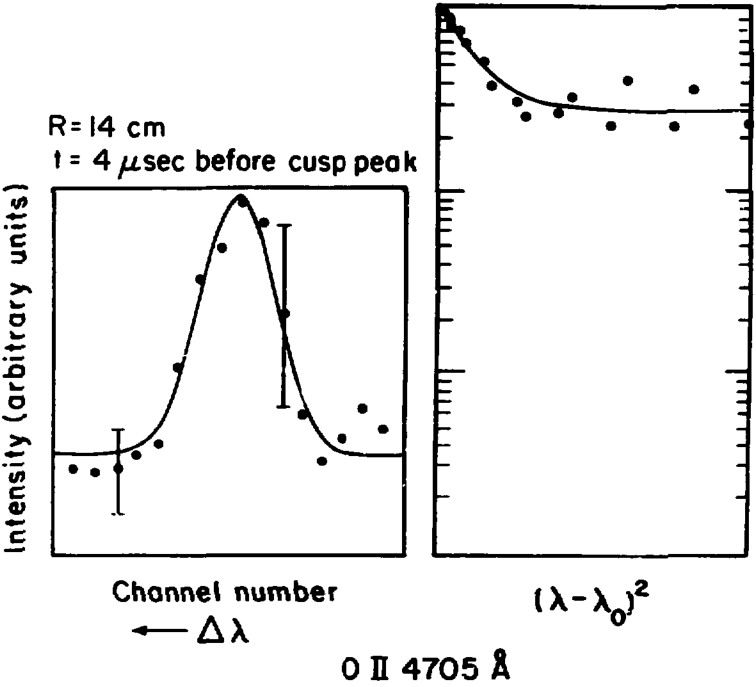

XBL 806–1161

Fig. 46. O II 4705Å line profile from T IV, on a linear (left) and logarithmic (right) scale. Data were taken along a line of light at P = 14 cm looking axially at a time 4 μsec before cust peak. Channel separation is 0.3Å.

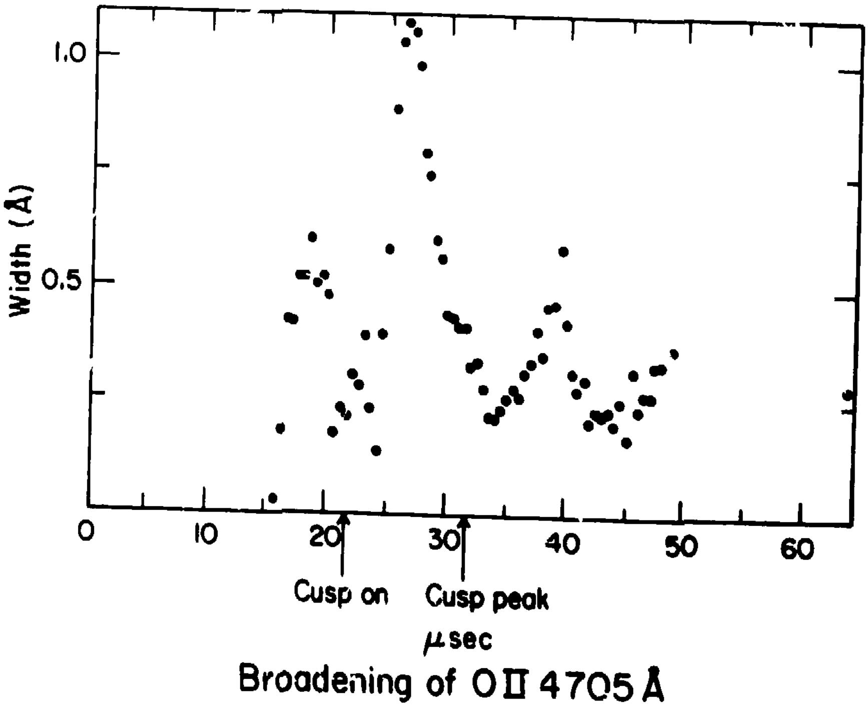

Fig. 47. Width of OII 4705Å vs time in T IV.

XBL 804-4139

Figure 48 shows a typical profile, taken from a line of sight at R = 14 cm looking axially. This is from an average of 10 machine shots, and a 5 μsec time average during the preionization phase. There is structure on the blue wing at the location of the forbidden component, 1.3 Å from the center of the 4922 Å line. This enhanced emission is presumably due to electric fields associated with plasma oscillations. The effect of the density variation along the line of sight is to smear out the satellites. The intensity of the line becomes very low as the cusp discharges, since this is a neutral helium line, and it burns out. When the preionize voltage is raised, the satellite becomes more distinct — less spread out. Changing the bias made no difference in the appearance of the lines.

(7) Flux Loop: This measures the fraction of excluded flux when the plasma is present. The higher the plasma β, the larger this fraction is. It is found[35] that this fraction is about 3% at all times except during the early part of the cusp rise.

B. T V

Much of the information gathered from the diagnostics used on T V is being written for publication.[36,58] Therefore, these results will only be summarized here.

(1) Rogowski coils: Figure 49 shows the preionize and cusp circuit currents as functions of time, for the normal bank operating voltages. At this time, the bias is at its peak and is slowly varying. These data are very similar to the T IV data. One difference is that the preionization frequency is lower for T V, and the bank is not crow-

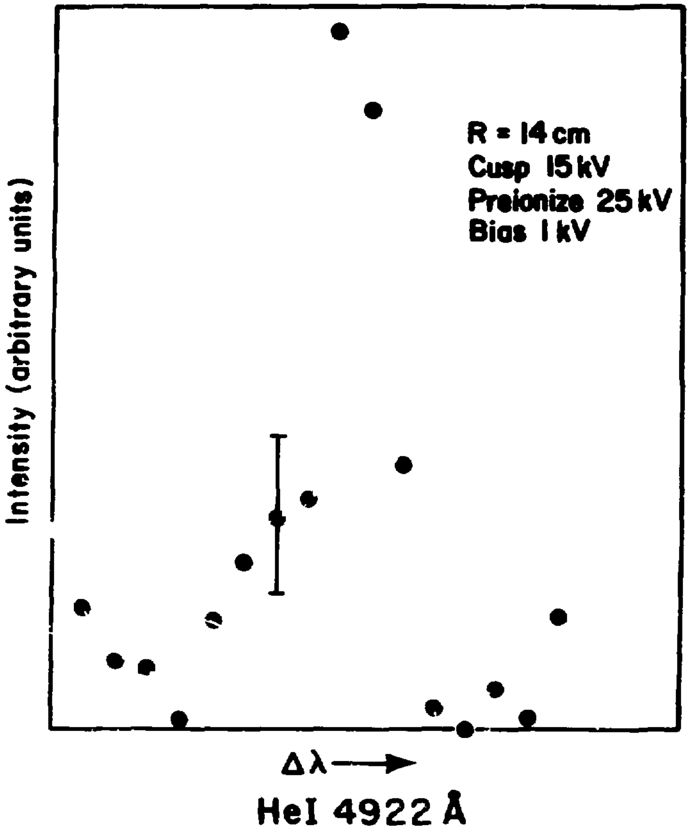

XBL 804-4138

Fig. 48. HeI 4922Å line width from T IV from a line of sight at R = 14 cm looking axially. This is from a 5 μsec time average during the preionization phase, and a 10 machine shot average. Channel separation is 0.3Å.

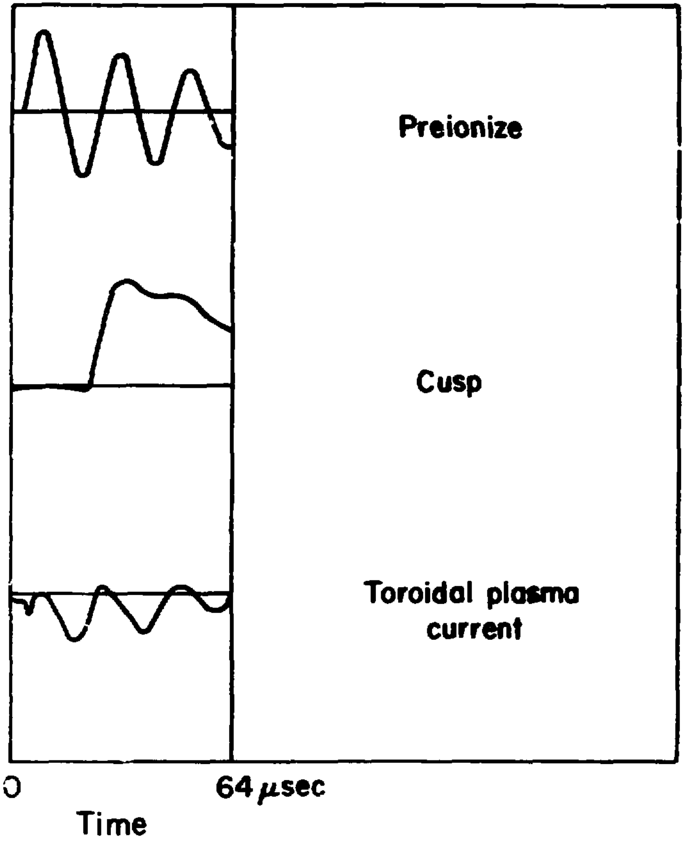

XBL 804-4137

Fig. 49. The T V experimental sequence.

barred. This results in a slight oscillation of the cusp current after the peak, due to the coupling of the two banks. The coupling of the cusp to the bias bank is the same as found on T IV. The presence of plasma results in increased damping of the preionize current.

(2) Plasma current Rogowski: Figure 49 also shows the behavior of the toroidal plasma current in time in relation to the currents in the banks. Both the cusp and the preionizer freeze in current. The peak current is ~ 70 kA. Note that this current is greater than the current found in T IV. Two distinct breakdown modes are found. In one, the current does not start to flow until the second half cycle of the preionization bank - similar to the behavior found in T IV. In the other mode, the plasma current starts to flow almost immediately, and follows the first half cycle of the preionization bank. No relationship between which mode occurs and the machine parameters has been found.

(3) Magnetic probes: A study was made of the penetration of the magnetic field into the plasma, and is being written for publication.[58] The results are as follows:

a) The poloidal magnetic field propagates inward in major radius with a spread of ~ 7-18 cm/μsec (Fig. 50). The front is well defined at large major radius, but has low amplitude and poor reproducibility at small major radius.

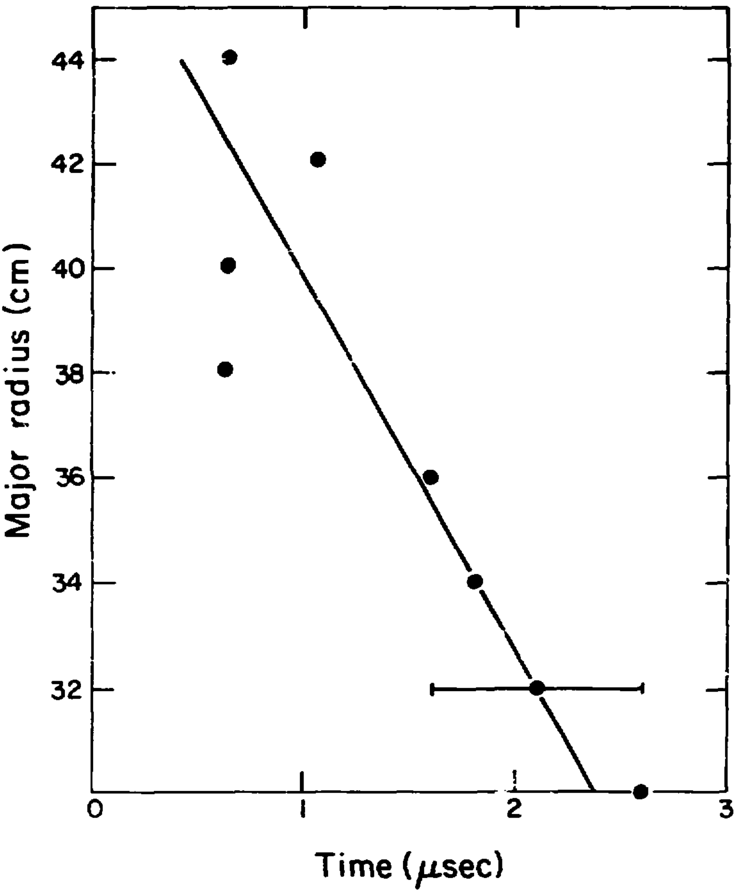

XBL 802-248

Fig. 50. Major radius vs cusp poloidal field arrival time in T V for the parallel bias case.

b) When the toroidal bias field is reversed, the poloidal field behavior is the same, except that the penetration speed is slightly slower than the parallel bias case.

c) The toroidal magnetic field shows no exclusion for the normal parallel bias case; i.e., the speed of penetration is too fast to be resolved.

d) With reversed bias, the toroidal field propagates into the plasma with a velocity of 2-6 cm/μsec. It has qualitatively the same behavior as the poloidal field (Fig. 51).

e) No toroidal field oscillations, as seen in T IV-c were observed under any conditions.

(4) <u>He-Ne Laser Interferometer</u>: The results of this diagnostic are being published in References 36 and 58. They are as follows:

a) Typical behavior of the line density is shown in Fig. 52. The mean density during preionization is ~ 5 x 10^{14} cm^{-3}. At cusp peak, the mean density is ~ 10^{15} cm^{-3}.

b) Simultaneous compression and ionization is seen as the cusp field rises.

c) The location of the density maximum is about where the magnetic well is located.

d) There is propagation of a density front from large major radius inward. No front is seen at small major radius for the parallel bias case (see Fig. 53). This is consistent with the interpretation that the poloidal magnetic field compresses the plasma.

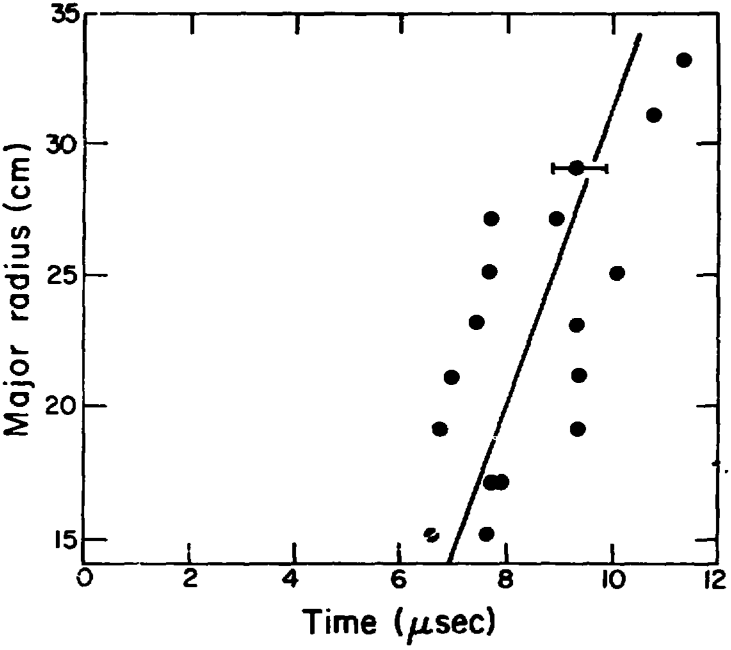

XBL 802-247

Fig. 51. Major radius vs cusp toroidal field arrival time in T V in the reversed bias case.

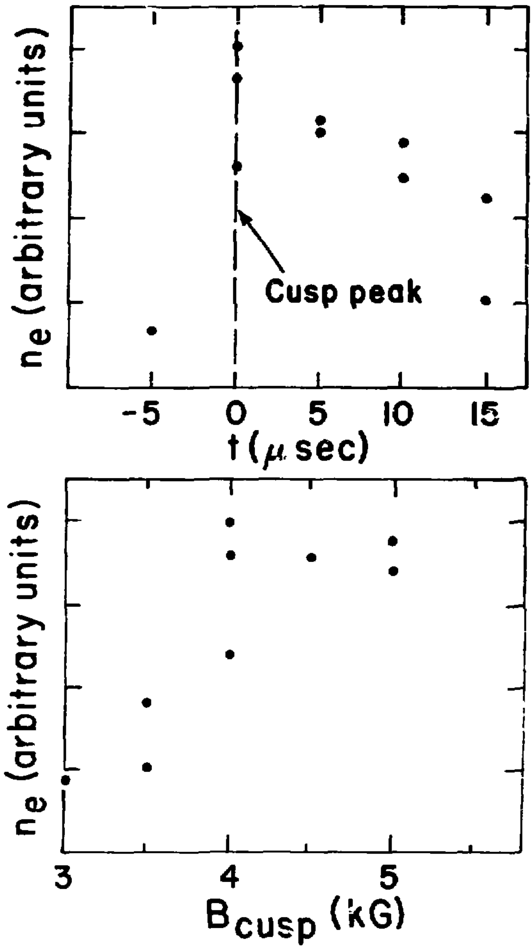

XBL 7911-4596

Fig. 52. Top: Electron density vs time in T V. Each point represents a machine shot.
Bottom: Electron density vs peak cusp field in T V. Each point represents a machine shot.

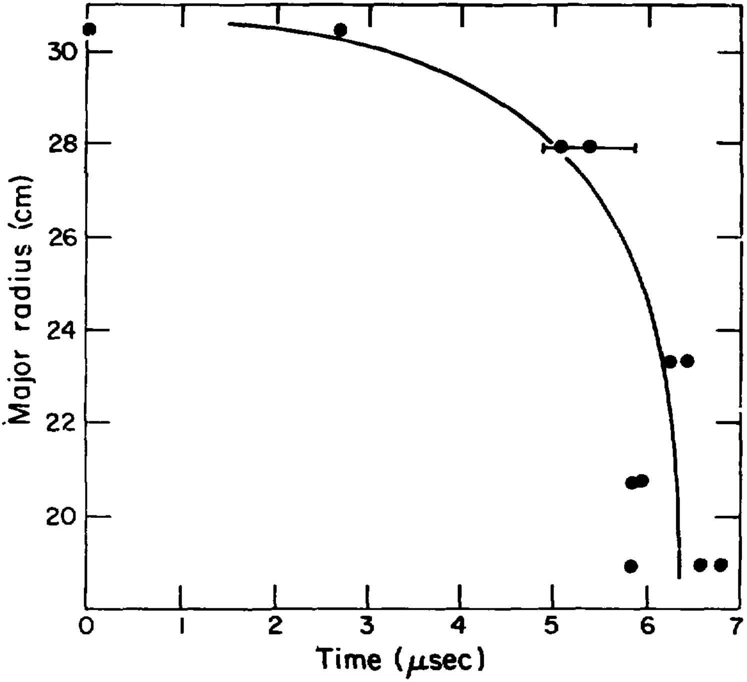

XBL 802-244

Fig. 53. Major radius vs line density arrival time in T V for the parallel bias case. Each point represents a machine shot.

e) In the reversed bias case, two fronts are seen. One propagates from large major radius inward, and the other propagates outward from small major radius (Fig. 54).

f) The decay of the density has a time constant of 20–30 μsec.

(5) Thomson Scattering: Figure 55 shows the measured electron temperature vs. time. The temperature is < 10 eV at all times, and is insensitive to machine parameters. The measured temperature has much scatter from shot to shot. A similar scatter in Thomson scattering measurements has been found in a Z-pinch,[59] and attributed to striation of the plasma current.

(6) Spectroscopy:

HeII 4686 Å

The widths of HeII 4686 Å in T V are smaller than those found in T IV. Figure 56 shows a typical line profile with a Gaussian fit for a line of sight at R = 33 cm, taken at cusp peak. This is a 3 shot average. The full width is 1.3 Å, and corresponds to 53 eV ion temperature. Widths of > 2 Å are found, but in general the widths range from 1 to 1.8 Å.

The data from T V have noise similar to that found in T IV. An average, either in time or over several machine shots, yields very Gaussian lines. The following features are observed in T V:

a) Widths do not change with fill pressure above 10 mTorr.

b) Lines are brightest at ~ 20 mTorr fill pressure.

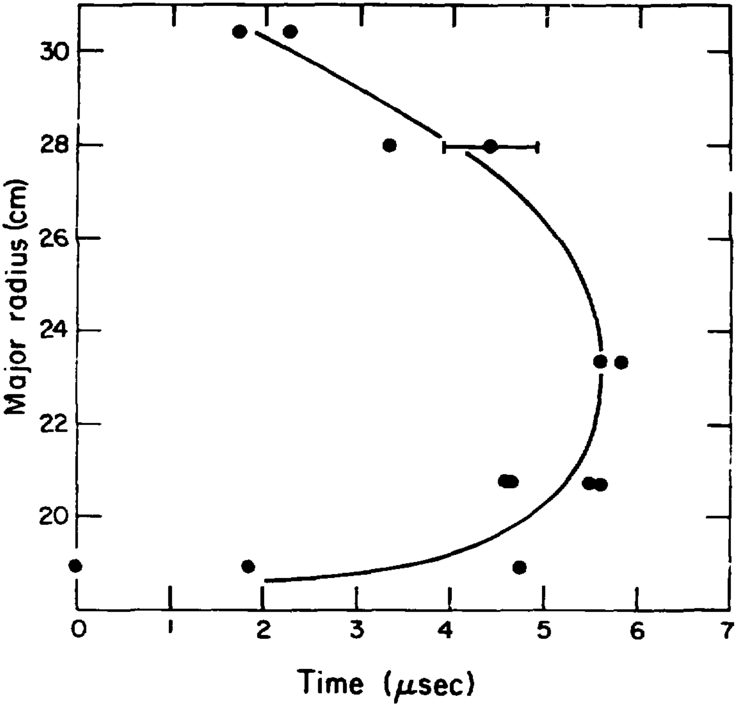

Fig. 54. Major radius vs line density arrival time in T V for the reversed bias case. Each point represents a machine shot.

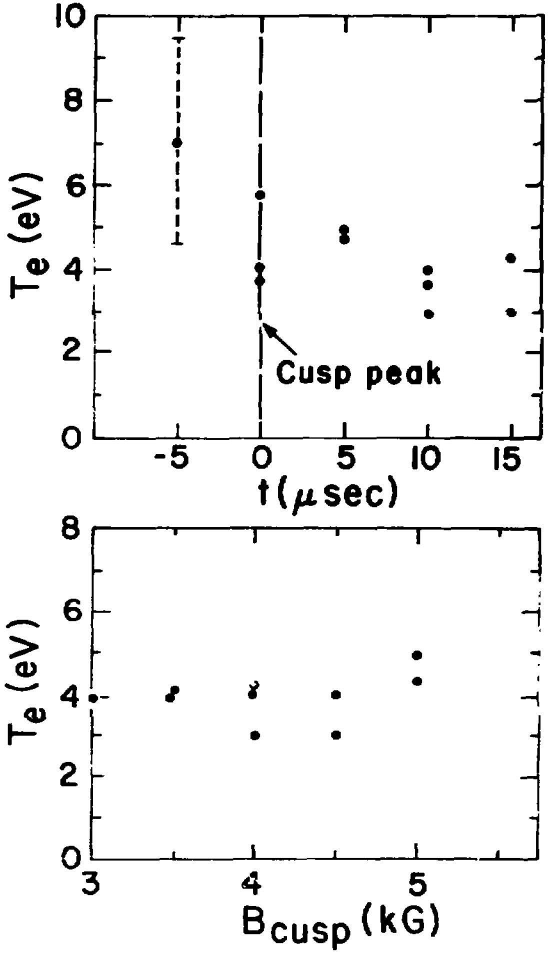

XBL 7911-4595

Fig. 55. Top: Electron temperature vs time in T V. Each point represents a machine shot.
Bottom: Electron temperature vs peak cusp field in TV.

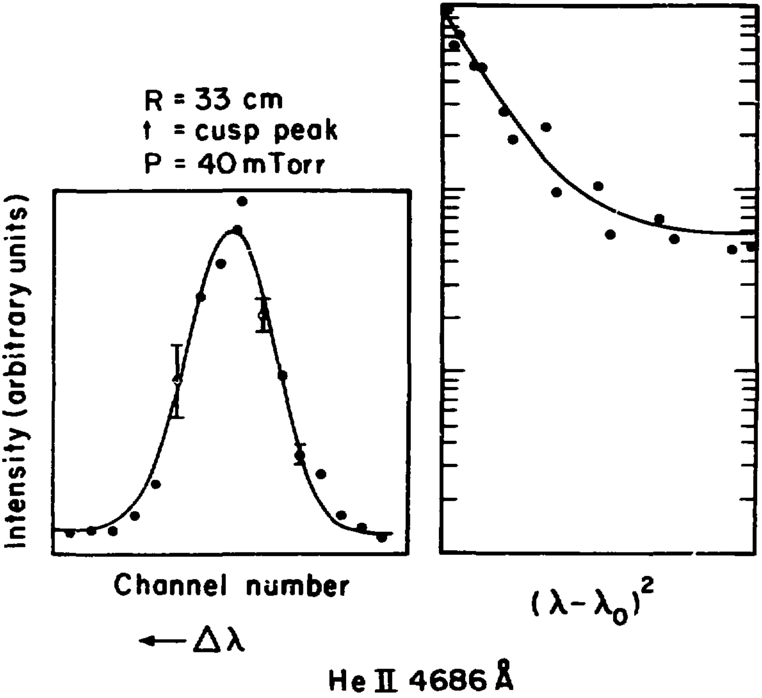

XBL 806-1160

Fig. 56. HeII 4686Å line profile from T V, on a linear (left) and logarithmic (right) scale. Data were taken along a line of sight at R = 33 cm looking axially at cusp peak. These data are from a 3 machine shot average. Channel separation is 0.3Å.

c) Varying the cusp firing time with respect to the preionize changed the light amplitude but not the widths.

d) The widths taken with parallel bias are less than those taken with reversed bias ($\Delta\lambda \sim 0.7$ Å), and the light is less bright. Figure 57 shows the inferred temperature vs. time for the two cases.

e) Oscillations of the widths in time are seen. They are more prevalent in the reversed bias case. The frequency is twice the frequency of the oscillation of the net toroidal plasma current; the maxima of the widths occur at the extremes of the current.

f) For parallel bias, widths of the lines do not change with the preionize voltage or cusp voltage. For reversed bias, they increase with preionize voltage.

g) Less light is observed as the preionize voltage is lowered.

HeII 3203 Å

The uv polychromator is used to observe HeII 3203 Å. The light amplitude is quite low, and the line is only seen when the bias is reversed. Typical full widths near cusp peak are ~ 2 Å.

Hβ 4861 Å

The following are found:

a) Before cusp discharge, the width of Hβ is ~ 1 Å, for 50 mTorr fill pressure.

b) At cusp peak, the width is ~ 1.23 Å, for 50 mTorr pressure

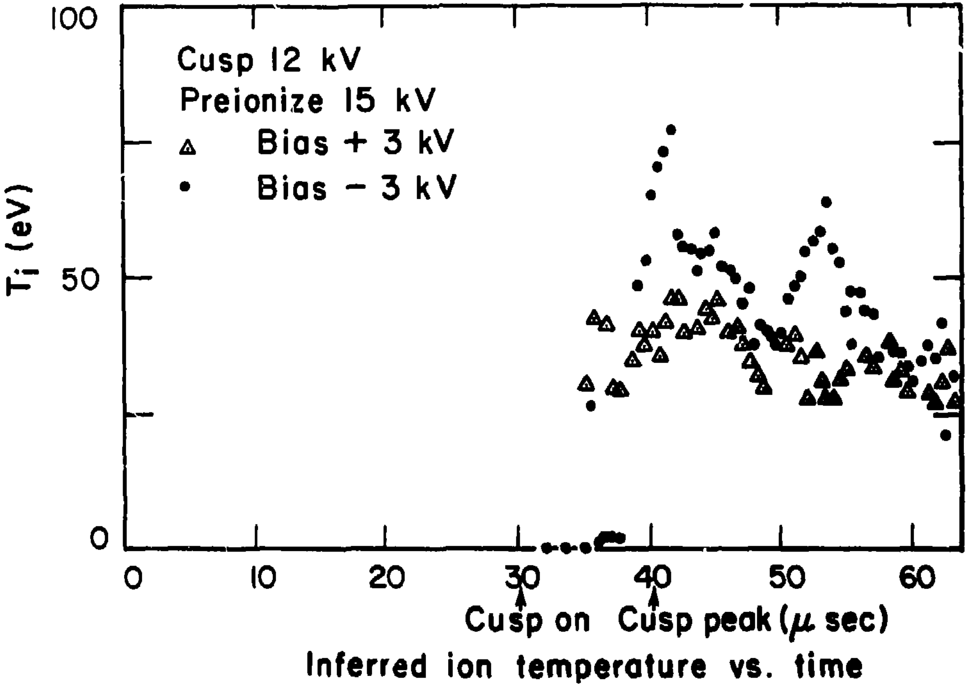

Fig. 57. Ion temperature inferred from Doppler broadening of HeII 4686Å vs time in T V.

XBL 806-1159

c) The width increases as the fill pressure is increased to ~ 30 μTorr, after which there is no change.

d) There is more light in the reversed bias case.

e) There is more light at large major radius.

f) The direction of the bias field has little effect on the widths.

g) There exists a front of Hβ light associated with the cusp discharge. The velocity of the front is ~ 4 cm/μsec, which is similar to the poloidal field penetration speed.

Hα 6563 Å

There is a difference in the widths of Hα between the parallel and reversed bias cases, both during the preionization and cusp phases. Widths of ~ 1.2-1.54 Å are found during preionization, and 1.73-2.2 Å at cusp peak.

HeI 4922 Å

Data are taken using the 80:20 gas mixture of H_2 and He. The line and its satellites are not bright, so that many shots are averaged together to give good statistics. In addition, data are taken using only H_2 gas, and these are subtracted from the above data. This is done to subtract out any impurity lines which may be present, and to better define the helium lines. Nevertheless, there is a great deal of photon noise. The following have been observed:

a) As the fill pressure is raised, the 4922 Å line gets slightly wider.

b) The structure appearing on the blue wing is much better defined when the bias is reversed.

c) The two bumps on the blue wing become farther apart during the rise of the cusp. Figure 58 shows the line before and after cusp discharge. These are 5 μsec time averages and averages over 30 machine shots. If the satellites are interpreted as due to Langmuir turbulence, the density during preionization is ~ 1.7 x 10^{13} cm^{-3}, and during cusp rise is ~ 1.4 x 10^{14} cm^{-3}. These are inferred from the separation of the satellites. Since this is a neutral helium line, it is expected to originate from the cooler, less dense part of the plasma.

d) A rough calculation from the satellite amplitude gives a field magnitude of ~ 11 kV/cm.

HeI 4472 Å

This line is very noisy, probably due to loss of light in the light pipe. Nevertheless, structure on the blue wing is definitely observed, although nothing quantitative can be said.

Impurities

The following lines were looked for, but not found:

NII 4793.5 Å
CI 5380 Å
OII 4151.7 Å
OIV 3736.8 Å
OIV 3811 Å
OV 4130.4 Å

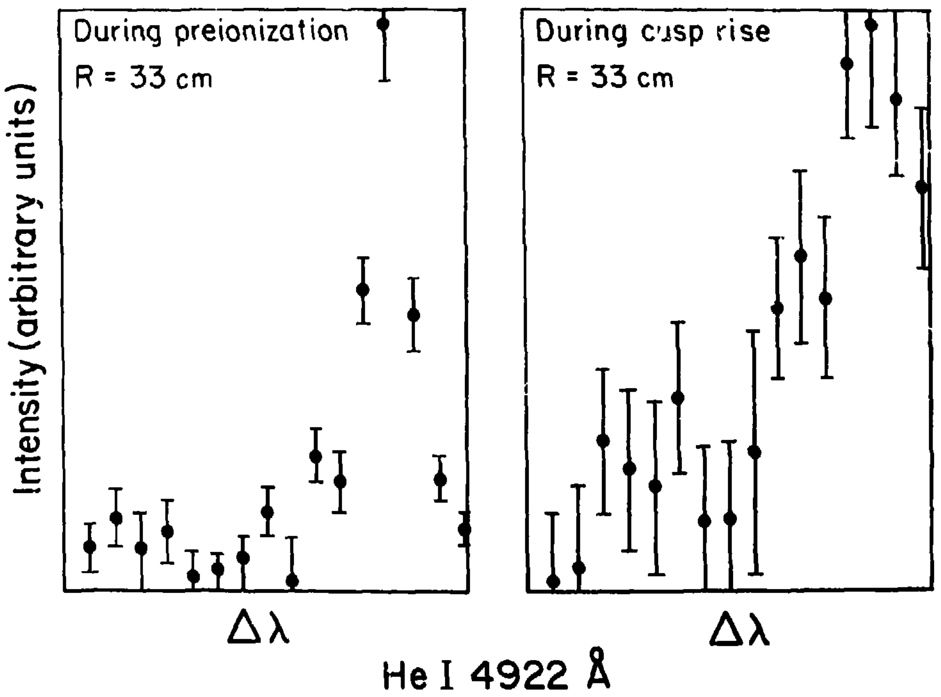

XBL806-1162

Fig. 58. HeI 4922Å line profiles from T V from a line of sight at R = 33 cm looking axially. These are 5 μsec time averages during preionization (left) and during cusp rise (right), and are averages over 30 machine shots. Channel separation is 0.3Å.

OII 4705 Å was observed. It was very dim, and therefore very noisy.

(7) Flux Loop: The excluded flux is ~ 2% for times at and shortly after the peak of the cusp, and decreases thereafter.

(8) Langmuir probe: This diagnostic produced some interesting results:

a) No voltage or electric field was measured in vacuum.

b) With gas present, the measured voltage follows the preionization bank oscillation, with amplitude ~ 400 V.

c) The maximum voltage measured on one probe occurs $\leq 1 \mu$sec after cusp discharge, and is ~ 1.5 kV.

d) Oscillations of ~ 2 MHz are seen during the rise of the cusp (Fig. 59). The amplitude of these oscillations, ~ 30 v/cm, is maximum at ~ 50 mTorr fill pressure.

e) The oscillation amplitude is larger for reversed bias than for zero or parallel bias.

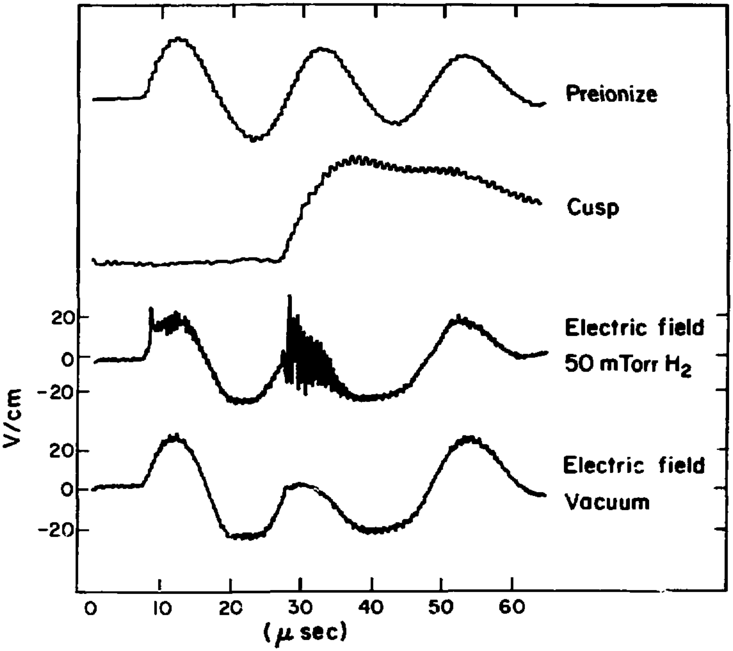

XBL 806-1157

Fig. 59: Measured electric field vs time in T V with and without plasma. Preionize and cusp circuit currents, measured with Rogowski coils, are also shown.

IV. DISCUSSION

The use of spectroscopy as a plasma diagnostic has many advantages. Light is emitted throughout the evolution of the plasma, and its collection is non-perturbing. The characteristics of this light, such as its intensity as a function of wavelength, widths and shapes of spectral lines, and line center location depend on the nature of the plasma.[60-64] Information on what elements are present, electron and ion temperatures and densities, magnetic and electric field strengths, and the properties of possible turbulence present in the plasma may be obtained. The disadvantage of using spectroscopy as a diagnostic is that often the measurement is difficult to interpret. One problem is that many effects are usually present at once, and separating their effects on the measured light is difficult. Another problem is that the measurement is line of sight — the collected light comes from many spatial positions across the plasma. Unless the plasma has spatial symmetry, or many lines of sight are taken to ensure a good reconstruction,[53,65,66] the exact location of the emitters is difficult to ascertain. The light may originate in regions having different plasma properties, and, thus, interpretation becomes uncertain. For example, since the measurement of some plasma properties requires the intensity at several wavelengths, there always exists some uncertainty as to whether the light originates from the same region along the line of sight. Another problem is that the intensity of the emitted light arising from a bound-bound transition depends on the density of the emitters in the upper state of the line. This in turn depends on the plasma parameters. This dependence is a function of the plasma model assumed. Some plasma models, as applied to the Tormac plasma, are discussed in Appendix B.

A. General Theory of Line Emission

For a bound-bound transition, the emissivity at wavelength λ and position x, defined as the power radiated at that position and wavelength per volume, solid angle, and wavelength interval, may be written as[60]

$$\epsilon(\lambda,x) = \frac{\hbar(2\pi c)^2 r_o}{\lambda^3} \quad \frac{g_n}{g_m} f_{mn} N_m(x) L(\lambda,x),$$

where m = upper state of the line

n = lower state,

g_n = degeneracy of state n,

r_o = classical electron radius = e^2/mc^2

f_{mn} = absorption oscillator strength,

$N_m(x)$ = density of emitters in state m at position x,

and $L(\lambda,x)$ = lineshape factor, which satisfies

$$\int L(\lambda,x)d\lambda = 1.$$

The intensity of the radiation $I(\lambda,x)$, defined as the power at position x and wavelength λ per area, solid angle, and wavelength interval, is measured by the polychromator. It obeys the following radiation transfer equation:

$$\frac{d}{dx} I(\lambda,x) = \epsilon(\lambda,x) - k(\lambda,x)\, I(\lambda,x),$$

where $k(\lambda,x)$ is the total absorption coefficient, defined and applied to Tormac in Appendix C. For an optically thin plasma (see Appendix C), the solution of this equation may be written as

$$\begin{aligned} I(\lambda) &= \int \epsilon(\lambda,x)dx \\ &= \frac{\hbar(2\pi c)^2 r_o}{\lambda^3} \; \frac{g_n}{g_m} \; f_{mn} \int N_m(x)\; L(\lambda,x)dx, \end{aligned}$$

where $I(\lambda)$ is the intensity measured at the detector, and the integral is over the line of sight through the plasma. This equation shows that the measured intensity gives information on the plasma parameters not only through $N_m(x)$ (Appendix B), but also through $L(\lambda,x)$, the line shape factor.

B. Line Broadening Mechanisms

$L(\lambda,x)$ is affected by the plasma through the action of various broadening mechanisms. By knowing which broadening mechanism is dominant, or by folding in the effects of several mechanisms on $L(\lambda,x)$, information on various plasma parameters may be obtained. A discussion of these broadening mechanisms is, therefore, necessary to understand the shape of spectral lines.

Natural line broadening, due to uncertainty in the energy of the levels, is never a factor, and is ignored. Doppler broadening is the broadening of spectral lines due to motion of the emitters.[60] This motion causes a shift in the wavelength of the emitted line, expressed as

$$\Delta\lambda = \lambda_0 \frac{v}{c} ,$$

where $\Delta\lambda$ is the wavelength shift, λ_0 is the wavelength of the light measured in the frame of the emitter, v is the velocity of the emitter away from the detector, and c is the speed of light. If $f(x,v)$ is the velocity distribution function of the emitting particles at position x, the line shape $L(\lambda,x)$ for Doppler broadening is given by (see Appendix D)

$$L(\lambda,x) = \int_{-\infty}^{\infty} \delta(\lambda - \lambda_0 - \Delta\lambda) \quad f(x,v)\, dv.$$

The delta function is used here since natural line broadening is ignored, and only Doppler broadening is considered. If the emitters have a Maxwellian distribution with zero average velocity, then

$$f(x,v) = \frac{1}{(2\pi)^{1/2}\, V_{th}(x)} \quad \exp\left[- \frac{v^2}{2V_{th}(x)^2}\right]$$

and

$$L(\lambda,x) = \frac{c}{(2\pi)^{1/2}\,\lambda_0\, V_{th}(x)} \quad \exp\left[-\frac{c^2(\lambda-\lambda_0)^2}{2\lambda_0^2\, V_{th}^2(x)}\right] ,$$

where

$$V_{th}(x) = \left(\frac{T(x)}{M}\right)^{1/2} ,$$

$T(x)$ is the emitter temperature at x and M is mass of the emitter. The full width at half maximum of the line is then given by

$$\Delta\lambda_{1/2} = 2^{3/2}\,(\ln 2)^{1/2}\;\lambda_0\sqrt{\frac{T(x)}{Mc^2}} .$$

For HeII 4686 Å, this gives

$$\Delta\lambda_{1/2} = \sqrt{\frac{T}{30.2}}\ \text{Å} ,$$

for Hβ 4861 Å

$$\Delta\lambda_{1/2} = \sqrt{\frac{T}{7}}\ \text{Å} ,$$

where T is the ion temperature in eV. Therefore, if thermal Doppler broadening is dominant, the line is Gaussian, and the width gives the temperature of the emitters. The additional requirement for this analysis to be valid is discussed briefly in Appendix D.

Another broadening mechanism that is important in laboratory plasmas is Stark broadening. Electric fields associated with either individual charged particles or with collective modes split and shift the energy levels of the emitter.[60-62] The result is a shape and a broadening of the line which depends on the density and temperature of the perturbers in the first case, or the frequency and magnitude of the field in the second case.[54-57,60-62,64,67-78] The exact form is very dependent on which line is involved, and the calculations can be quite complex (Appendix D).

The effect of individual charged particles on HeII 4686 Å has been calculated.[61] The full width at half maximum due to interparticle fields, including correlation effects, may be written

$$\Delta\lambda \sim 2.9 \times 10^{-14}\, N_e^{.83}\ \text{Å}.$$

The effect of the perturber temperature on the width of this line is small. The full width at half maximum for Hβ 4861 Å is

$$\Delta\lambda \sim 2.0 \times 10^{-10}\, N_e^{2/3}\ \text{Å}.$$

Both of these lines are subject to the linear Stark effect, in which the shift in the energy levels is proportional to the electric field. HeII 4686 Å has a central, unshifted component which is strongly affected by electron impact broadening. Hβ 4861 Å, however, has no unshifted central component, and has a central dip. It is strongly broadened by ion quasistatic broadening, which accounts for the characteristic $N^{2/3}$ dependence of the Holtsmark theory.

The broadening due to collective modes is similar to that due to individual particles, in that it can be divided into quasistatic or impact broadening. The two cases are distinguished by the relationship of the autocorrelation time of the light amplitude to the period of the mode, instead of to the collision time.[78] For emitters strongly affected by quasistatic broadening - lines not having central Stark components, such as Hβ - the relation between the full width of a line arising from a transition n→n' and the average turbulent electric field of low frequency modes (quasistatic), for the linear Stark effect, is given by

$$\Delta\lambda = \frac{3}{4}\,\frac{(n^2-n'^2)h\lambda_o^{\,2}}{2\pi Z\ mec}\quad E,$$

where m is the mass of the electron, E is the electric field strength in CGS units, and Z is 1 for hydrogen, 2 for helium. Lines having strong central components, such as HeII 4686 Å, are not appreciably broadened by these quasistatic fields.

High frequency modes, usually $\omega\sim\omega_p$, broaden lines by impact broadening. Therefore, the effect of these modes on the full widths of lines not having a central component is small. At these frequencies, the magnitude of the electric field is important in determining the effect of these modes on the lines. Two frequency ranges are important: 1) the frequency of the modes, ω, is larger than ω_E, the precession frequency of the dipole moment of the emitter in the electric field - perturbation theory may be used,[71] and 2) the frequency is smaller than ω_E. For case 1,

$$\omega > \omega_E = \frac{3}{2} \frac{n a_0 e E}{h} ,$$

where a_0 is the Bohr radius, and n is the upper level quantum number. This leads to a series of satellites, located at a distance from the unbroadened line given by

$$\Delta\lambda_i = i \frac{\lambda_0^2 \omega}{2\pi c} ,$$

where i is an integer. The intensity of these satellites is dependent on the stochasticity of the fields.[71] Note that if these modes have a frequency spread, the satellites are spread out, and may not appear as distinct. For case 2, $\omega < \omega_E$, the full width of lines having a central component is enhanced, and is given by[73]

$$\Delta\lambda = \frac{3\lambda_0^2 a_0}{m_e \omega_p c} \quad W_e \, n^2 \quad [n^2 - (n_1 - n_2)^2 - m^2 + 1] ,$$

where n is the principle quantum number of the upper state, n_1, n_2, and m are parabolic quantum numbers, and W_e is the energy density of Langmuir oscillations,

$$\int \frac{E_k^{\;2}}{8\pi}\, dk \; .$$

For Langmuir turbulence in Tormac, the critical field for which $\omega_E = \omega_p$ for HeII 4686 Å is

$$E_c = \frac{2\omega_p \hbar}{3na_o e} = 128 \text{ kV/cm} \; .$$

For $E < E_c$, this mode should create satellites. Note that these satellites are at least as broad as the line itself, in that they are not only subject to all the broadening mechanisms of the line, but they are also spread out due to the finite width of the turbulent spectrum.

C. Experimental Data

From the results of Thomson scattering on T IV and T V, the full widths of HeII 4686 Å and Hβ 4861 Å are expected to be ~ 0.4 Å and 0.85 Å, respectively, assuming thermal Doppler broadening. Using the inferred density of ~ 3×10^{15} cm^{-3} for T IV, the full widths of HeII 4686 Å and Hβ are expected to be ~ 0.2 Å and ~ 4.2 Å, assuming Stark broadening by interparticle fields. This is for times close to cusp peak. These expectations roughly agree with the measured results for Hβ, within the experimental uncertainty in the density. (Recall that the interferometer gives a line of sight measurement, and that there is no way of relating this measurement of density to the collected light, also a line of sight measurement, with any certainty.

In fact, the measured width of Hβ is expected to be less than the above calculated width, since Hβ would be less intense in the compressed part of the plasma, and emitting strongly in the low temperature, low density material.) However, the calculated width of HeII 4686 Å, folding in both of the above effects and instrumental effects, in no way corresponds to the measured width. The value of the density, which explained Hβ widths, would have to be $\gtrsim 4 \times 10^{16}$ cm^{-3} to explain HeII 4686 Å widths. After cusp peak, widths > 1 Å are observed to last a very long time. Thomson scattering indicates that the temperature is < 4 eV, and magnetic probes indicate that the open magnetic field lines have penetrated the plasma at this time. Therefore, density $\gtrsim 10^{16}$ cm^{-3}, needed to explain these widths, is unlikely. Spectroscopic measurements indicate that the broadening in time in T IV can be broken up roughly into two regions: the first region occurs during the rise of the cusp, and the second region begins at cusp peak. In the first region, very high widths are observed, which quickly fall before cusp peak. In the second region, the widths are much lower, and fall more slowly. The fact that two regions in time are found suggests that two different broadening mechanisms are operating in the two regions. Therefore, each time region will be discussed separately.

(1) Cusp Rise - T IV

This period is characterized by the rapid rise of large magnetic fields in a bicusp geometry. The induced electric field calculated from Faraday's law for these parameters is < 1kV/cm, and is insufficient to broaden HeII 4686 Å by the Stark effect. Magnetic probe and interferometric measurements indicate that this is a time of violent fluctuations in both toroidal magnetic field and density. The measured frequency of these fluctuations is well within the range of MHD theory ($\omega \ll \Omega_i$). These facts indicate that compressional Alfven modes are being excited by the cusp field. Similar measurements and conclusions were reported for θ - pinch experiments.[79] In addition, it is well known that a non-zero fluid velocity is associated with this mode. This would give rise to Doppler broadening. The properties of this MHD mode will be examined, and the characteristics of the resulting spectral lines will be noted.

Compressional Alfven Mode

To simplify the analysis, the following assumptions are made:

a) Low β — the effects of plasma pressure are discussed later.

b) Terms of order $\frac{M_e}{M_i}$ are ignored.

c) Infinite conductivity — the effects of finite conductivity are discussed later.

d) No sources or sinks of particles.

e) All quantities are written as $\underline{A}\,(\underline{r},t) = \underline{A}^{(0)}(\underline{r},t) + \underline{A}^{(1)}(\underline{r},t)$, where the superscripts indicate the order, and $\underline{A}^{(1)} \ll \underline{A}^{(0)}$.

f) $\underline{U}^{(0)} = \underline{E}^{(0)} = \underline{J}^{(0)} = 0$ — no zero order fluid velocity, electric field, or current.

g) For this mode $\omega << \Omega_i$.

Define the following:

ρ_m = mass density = $\sum_s M_s N_s$,

ρ_e = charge density = $\sum_s q_s N_s$,

$\underline{U}$ = fluid velocity = $\dfrac{\sum_s N_s M_s \underline{U}_s}{\rho_m}$,

$\underline{J}$ = current density = $\sum_s N_s q_s \underline{U}_s$,

$\underline{U}_s$ = average fluid velocity of species = $\int dv\, f_s(v) v$,

and s = species label.

Using these assumptions, the zero order equations yield the following solutions:

$$\rho_e^{(0)} = 0,$$

$$\rho_m^{(0)} = \text{constant in time},$$

and $\underline{B}^{(0)}$ = constant in time.

Note that $\rho_m^{(0)}$ and $\underline{B}^{(0)}$ may still be functions of space. Using these solutions and the above assumptions, the equations for the first order quantities may be written as follows:

1) $$\frac{\partial \rho_m^{(1)}}{\partial t} + \nabla \cdot (\rho_m^{(0)} \underline{U}^{(1)}) = 0$$

2) $\rho_m^{(0)} \frac{\partial \underline{U}^{(1)}}{\partial t} = \frac{1}{c} \underline{J}^{(1)} \times \underline{B}^{(0)}$

3) $\underline{E}^{(1)} + \frac{1}{c} \underline{U}^{(1)} \times \underline{B}^{(0)} = 0$

4) $\nabla \cdot \underline{E}^{(1)} = 4\pi \rho_e^{(1)}$

5) $\nabla \times \underline{E}^{(1)} = - \frac{1}{c} \frac{\partial \underline{B}^{(1)}}{\partial t}$

6) $\nabla \times \underline{B}^{(1)} = \frac{4\pi}{c} \underline{J}^{(1)}$

At this point, one other assumption will be introduced. Assume that $\rho_m^{(0)}$ and $\underline{B}^{(0)}$ are also uniform in space. The consequences of removing this assumption are discussed later. This now allows the first order quantities to be written as

$$\underline{A}^{(1)} (\underline{r},t) = \underline{A}_0^{(1)} e^{i(\underline{k}\cdot\underline{r}-\omega t)} .$$

The compressional Alfven mode has the following properties[12]:

$\underline{k}\cdot\underline{E}_0^{(1)} = 0$; i.e., the wave is transverse,

$\underline{k}\perp\underline{B}^{(0)}$,

and $\underline{E}_0^{(1)}\perp\underline{B}^{(0)}$.

Incorporating these into the first order equations yields

$$k^2 \underline{E}_o^{(1)} = \frac{4\pi i\omega}{c^2} \underline{J}_o^{(1)} ,$$

and

$$\frac{i\omega\omega_{po}^{2}}{4\pi}\,\underline{E}_o^{(1)} + \Omega_i^{(0)}\Omega_e^{(0)}\,\underline{J}_o^{(1)} = 0 ,$$

where

$$\omega_{po}^{2} = \frac{4\pi\, N^{(0)}\, e^{2}}{M_e}$$

$$\Omega_i^{(0)} = \frac{e\, B^{(0)}}{M_i c}$$

and

$$\Omega_e^{(0)} = \frac{e\, B^{(0)}}{M_e c} .$$

This gives the dispersion relation

$$\omega = \pm\, kV_A ,$$

where

$$V_A = \frac{B^{(0)}}{(4\pi\rho_m^{(0)})^{1/2}} .$$

These relations show that the current and the electric field are in the same direction. Also, the magnetic field of this mode is in the same direction as the zero order field, which if the zero order field is in the toroidal direction agrees with the measurements. The fluid velocity is perpendicular to both the electric and magnetic fields, and lies along $\underline{k}$.

If the low β assumption is removed, the first order momentum equation and Ohm's law are altered as follows:

$$\rho_m^{(o)} \frac{\partial \underline{U}^{(1)}}{\partial t} = \frac{1}{c} \underline{J}^{(1)} \times \underline{B}^{(o)} - \nabla P \quad ,$$

$$\underline{E}^{(1)} + \frac{1}{c} \underline{U}^{(1)} \times \underline{B}^{(o)} + \frac{M_i}{\rho_m^{(o)} e} \nabla P = 0 \quad ,$$

where P is the total electron pressure, assumed to be isotropic. The following adiabatic law must be included to complete the set of equations:

$$P \rho_m^{-\gamma} = \text{Constant} \quad ,$$

where $\gamma = \frac{f+2}{f}$, and f is the number of degrees of freedom. Solving this set of equations as before, the dispersion relation for the mode of interest becomes

$$\omega = k \left(C_s^2 + V_A^2\right)^{1/2} \quad ,$$

where C_s is the sound speed, and is given by

$$C_s^2 = \frac{\gamma P^{(o)}}{\rho_m^{(o)}} \quad .$$

For the Tormac parameters, $V_A \sim 10C_s$. Therefore, in this plasma, the plasma pressure has negligible effect on this mode, and is ignored.

If a non-zero resistivity were left in the calculation, the dispersion relation would be altered as follows:

$$\omega = \pm kV_A \left[1 - \frac{k^2\eta^2c^4}{64\pi^2V_A^2}\right]^{1/2} \quad ,$$

where η is the resistivity. The effect of increasing η is that the wavelength decreases for a given ω. Assuming classical resistivity and a wavelength of 5 cm, and using the measured parameters of 10^{15} cm^{-3} density, 1 kG magnetic field, and 5 eV temperature,

$$\frac{k^2\eta^2c^4}{64\pi^2V_A{}^2} \sim 2 \times 10^{-3} \quad ,$$

and, therefore, does not alter the mode significantly. One effect the resistivity does have is to damp the mode, with the damping rate given by

$$\gamma = -\frac{\eta k^2c^2}{8\pi} \quad .$$

For a wavelength of 5 cm, $\gamma \sim -4.1 \times 10^5$ rad/sec, which implies a damping time of 15 μsec, assuming classical resistivity and T ~ 5 eV. The shorter wavelength modes are damped more quickly than longer wavelength modes. For this reason, the longer wavelength modes are expected to play a dominant role in broadening HeII 4686 Å.

The effects of the fundamental mode will now be considered. A slab model is assumed, with the toroidal magnetic field along the Z-axis, the light collection system looks along X, and k is along X. This is a valid representation of the system since the acceptance angle of the light collection optics is so small. Assume that the plasma is located at $|x| \leq L$, so that the wavelength of the fundamental mode is $\lambda = 4L$. Also, for the fundamental mode, $\underline{U}^{(1)}(x=0,\ t) = 0$. Using the first order equations, together with all the stated assumptions, the following relations may be written for the fundamental mode:

$$\underline{E}^{(1)}(x,t) = E_0^{(1)} \sin\left(\frac{\pi x}{2L}\right) \sin(\omega t) \quad \hat{y} \ ,$$

$$\underline{J}^{(1)}(x,t) = \frac{kc^2 E_0^{(1)}}{4\pi V_A} \sin\left(\frac{\pi x}{2L}\right) \cos(\omega t) \quad \hat{y} \ ,$$

$$\underline{B}^{(1)}(x,t) = \frac{c\ E_0^{(1)}}{V_A} \cos\left(\frac{\pi x}{2L}\right) \cos(\omega t) \quad \hat{z} \ ,$$

$$\underline{U}^{(1)}(x,t) = \frac{c\ E_0^{(1)}}{B^{(0)}} \sin\left(\frac{\pi x}{2L}\right) \sin(\omega t) \quad \hat{x} \ ,$$

$$\rho_m^{(1)}(x,t) = \frac{\rho_m^{(0)} c E_o^{(1)}}{V_A\ B^{(0)}} \cos\left(\frac{\pi x}{2L}\right) \cos(\omega t) \quad ,$$

and

$$\rho_e^{(1)} = 0 \quad ,$$

where $\omega = |kV_A|$, $|x| \leq L$, and $E_o^{(1)}$ is the parameter which describes the amplitude of the mode. From experimental observations, $\omega \sim 4.4 \times 10^6$ rad/sec, and the oscillations in the field occur when $B^{(0)} \sim 1$kG, and have magnitude ~ 600G. Taking $n^{(0)}$ to be $\sim 1 \times 10^{15}$ cm^{-3}, the fluid velocity is given by

$$\underline{U}^{(1)}(x,t) \sim 4.2 \times 10^6 \sin\left(\frac{\pi x}{2L}\right) \sin(\omega t) \quad \hat{x} \ .$$

Note that this varies in time at frequency ω. It should be emphasized that the HeII 4686 Å width is varying rapidly in time. However, the data acquisition system sampling frequency is comparable to ω, and it is difficult to separate these effects.

The oscillating field amplitude seen in the experiment is not small compared to the zero-order field amplitude. The linear problem is solved here, since it yields approximate results, and is much simpler than the full non-linear problem.

Using the line shape formula for Doppler broadening presented in the line broadening section, the lineshape is given by

$$L(\lambda,x) = \frac{c}{\lambda_0 (2\pi)^{1/2} v_{th}} \exp\left\{ -\left[\frac{c(\lambda - \lambda_0)}{\lambda_0} - U(x) \right]^2 / 2v_{th}^2 \right\} ,$$

where $U(x) \sim 4.2 \times 10^6 \sin(\frac{\pi x}{2L})$, and

$$v_{th} = \left(\frac{T}{M_i}\right)^{1/2}$$

is assumed constant in x. Using a formula presented earlier, the measured intensity of the spectral line may be written as

$$I(\lambda) \propto \int_{-L}^{L} N_m(x) L(\lambda,x) dx ,$$

where $N_m(x)$ is the density of emitters in the upper state of the line which participate in the postulated fluid motion. As derived above, the density perturbation due to this mode is proportional to $\cos(\frac{\pi x}{2L})$, so assume that $N_m(x) \propto \cos(\frac{\pi x}{2L})$. Figure 60 shows the line shapes calculated using the above assumptions for T equals 1 and 5 eV, both with and without the Alfven mode present. The additional broadening is quite obvious; the full width of the 1 eV line without the mode is 0.18 Å, whereas with the mode present it is 1.3 Å, corresponding to 54 eV. As the temperature is raised, the line shape approaches a Gaussian. The wings of the line always appear Gaussian, and this is seen experimentally. The center of the line is not Gaussian, and this is often seen experimentally (see Fig. 42).

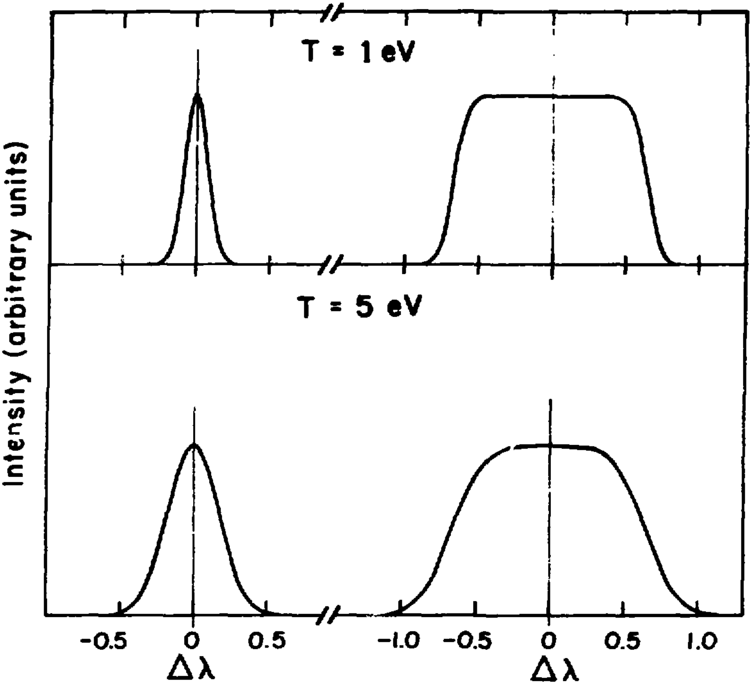

XBL 806-1158

Fig. 60. HeII 4686Å line profile vs Δλ with and without Alfven mode present for an ion temperature of 1 eV (top) and 5 eV (bottom).

The line shape depends critically on what is taken for $N_m(x)$, and, unfortunately, this cannot be known exactly. This number depends sensitively on the density and temperature of the plasma at point x, as mentioned in Appendix B. Since T(x) is not known, $N_m(x)$ cannot be known. Note also that if T varies with x, it changes not only $N_m(x)$, but also $L(\lambda,x)$, and the total effect on $I(\lambda)$ cannot be predicted without knowing the exact spatial dependence.

Another uncertainty in this analysis is that $N^{(0)}$, the zero order density, is not known here. At the time these modes appear, $N^{(0)}$ is varying due to the ionizing effect of the cusp fields. If $N^{(0)}$ is lower than assumed above, the broadening due to these modes would increase.

One assumption used to derive these results was that both the zero order density and magnetic field were constants in space. This resulted in $U(x) \propto \sin(\frac{\pi x}{2L})$. The assumption was made for convenience. In the experiment, one would expect a peaking of the zero order density around x=0 due to the action of both the preionize and cusp fields. However, removing this assumption results in a much more complicated problem. For example, keeping the x dependence of $\rho_m^{(0)}$ and $B^{(0)}$ gives

$$\frac{d^2}{dx^2}\left[U_o^{(1)}(x)\ B^{(0)}(x)\right] = \frac{-4\pi\omega^2\rho_m^{(0)}(x)}{B^{(0)}(x)}\ U_o^{(1)}(x) \ ,$$

where the quantities are now written as

$$\underline{A}(x,t) = \underline{A}^{(0)}(x) + \underline{A}_0^{(1)}(x) \quad e^{-i\omega t}.$$

If $B^{(0)}$ is still assumed to be a constant, this equation reduces to

$$\frac{d^2}{dx^2} U_o^{(1)}(x) + \frac{\omega^2 \, 4\pi\rho_m^{(0)}(x)}{B^{(0)\,2}} \; U_o^{(1)}(x) = 0 \quad .$$

The problem of what to take for $\rho_m^{(0)}(x)$ still remains. However, if $\rho_m^{(0)}(x)$ is peaked at x=0, instead of being flat, and the fundamental mode is considered, then the form of the equation indicates that U(x) is greater at all spatial points for the peaked case. Whether this has the effect of broadening the lines further depends on $N_m(x)$.

Much information that is not known goes into the calculation of the line shape. However, experimental measurements which support this broadening hypothesis exist. The broadening of the OII 4705 Å impurity line has behavior similar to HeII 4686 Å; i.e., there is maximum broadening during cusp rise followed by a rapid fall. Also, the amount of broadening is the same when looking from any direction in the poloidal plane, as would be expected from this mechanism. Hβ does not have similar broadening behavior in time. However, Hβ is so strongly Stark broadened that this amount of Doppler broadening is smaller than that due to Stark, especially later in the cusp rise. Furthermore, Hβ may not be coming from the same regions, as discussed earlier.

The energy contained in this mode is very high. However, since the magnetic field penetrates into the plasma very quickly, the plasma is on open field lines which intersect the walls. The energy from this mode can be conducted along the lines and deposited in the cool, surrounding plasma, and on the walls.

Higher harmonics having smaller wavelengths must certainly exist, even though they are more highly damped. Their effect on the line shape cannot be predicted, since it depends on their relative amplitudes. The damping time depends on the value of the resistivity. If classical resistivity is assumed, the damping time for the fundamental is $\lesssim 15$ μsec.

It should be noted that the electric field associated with this mode is very small. The field magnitude is given by

$$E^{(1)} = \frac{B^{(1)}}{n} \leq 50 \text{ v/cm} ,$$

where n is the index of refraction. These fields would have no effect on the line through the Stark effect.

(2) Post Cusp Peak - T IV

By this time, the preionize and cusp banks have been crowbarred, and all fields are decaying. The plasma extends from the inner wall out, and is located on open field lines in a low β situation. The temperature is < 4 eV, and the density compression dies away within ~ 6 μsec after cusp peak. Nevertheless, HeII 4686 Å lines having widths > 1 Å are consistently observed out to 30 μsec past cusp peak. (These large widths have been observed to extend longer than 50 μsec past cusp peak in the past.) The compressional Alfven modes occurring during cusp rise are observed to rapidly damp out after cusp peak. Some other mechanism must be responsible for the broadening of the spectral lines, as Doppler broadening does not seem to be a major effect at this time.

One striking feature found during this period is the large toroidal current flowing in the plasma (Fig. 27). This current decays slowly, and has considerable magnitude even late in time. Experimental evidence exists that the broadening increases as this current is raised. It is well known that currents of this magnitude flowing in a cold plasma can excite turbulence.[71,75,76,80,81,82] This turbulence can affect the line shapes of spectral lines. This possibility will now be examined.

Turbulence

A thermal level of fluctuating electric fields, having frequencies around ω_p, always exists. The magnitude of these fields depends on the plasma parameters. Usually this is very small when compared to the average Holtsmark field strength; i.e., usually

$$\frac{\langle E^2_{turb} \rangle^{1/2}}{\langle E_H \rangle} \sim \frac{1}{100} ,$$

where E_{turb} is the turbulent electric field strength, and $\langle E_H \rangle$ is the average Holtsmark field strength ~ 8e $n^{2/3}$. However, in Tormac, where the temperature is low and the density relatively high, this ratio is

$$\frac{\langle E_{turb}^{2}\rangle^{1/2}}{\langle E_{H}\rangle} \sim \frac{1}{10}$$

This says that there exists a rather large level of thermal fluctuations due to the existing plasma conditions in Tormac, and that only a relatively small amount of non-thermal fluctuations, generated, for example, by a large current in the plasma, would be needed to raise the turbulent fields above the particle fields. If this occurs, the Stark broadening of the HeII 4686 Å spectral lines would be dominated by the turbulent fields.

In an earlier section, it was stated that such high frequency fields affect spectral lines through the Stark effect in the impact approximation. The problem of the effect of high frequency stochastic fields generated by a current in the plasma on lines subject to the linear Stark effect has been considered in Ref. 71. There it is shown that if the field has frequency ω_p, the spectral line splits into a series of satellites spaced ω_p apart. The intensity of the n^{th} satellite is found to be

$$I_n \sim \exp\left[-\frac{n^2\omega_p^2}{2(\Delta\omega)^2}\right]$$

where $$\Delta\omega = \alpha\left(\sum_{K=1}^{N} E\,k^{2}\right)^{1/2} ,$$

α is the constant of the linear Stark effect for the line in question, E_k is the magnitude of the field for mode k, and N modes are included. This form for the intensity of the satellites is for stochastic fields, and is not obtained for the monochromatic, fixed phase case. For Langmuir waves, the dispersion relation is given by

$$\omega^2 = \omega_p^2 \, (1 + 3\, k^2 \, \lambda_e^2) \quad ,$$

where λ_e is the Debye length. Therefore, the actual frequency of the turbulence is slightly different from ω_p; i.e., ω depends on k. When a beam of electrons passes through the plasma, Langmuir turbulence is excited.[81] It has been calculated that during the saturation stage, the intensity of mode k is given by

$$|E_k|^2 \approx 4\pi^2 \, nm \, \frac{\omega_p^3}{k^4 v} \quad ,$$

where v and n are the velocity and density of the beam electrons, and m is the mass of the electron. When an allowance is made for the dependence of ω on k, and the above expression for $|E_k|^2$ is used, the line shape may be written[71]

$$I(\omega) \propto \exp\left[- \frac{\omega^2}{(\Delta\omega)^2}\right] \quad ,$$

where $\Delta\omega = 2\alpha \left[\frac{2}{3} \pi \, nm \, v^2\right]^{1/2}$.

Therefore, the line shape for a spectral line subject to the linear Stark effect due to stochastic Langmuir turbulence generated by a beam of electrons is a Gaussian. The full width at half maximum for HeII 4686 Å is given by

$$\Delta\lambda \sim 2.18 \times 10^{-15}\, n^{1/2}\, v,$$

where $\Delta\lambda$ is in Å, n is the beam density in cm^{-3}, and v is the velocity of the electrons in cm/sec.

If the expression for $|E_k|^2$ is integrated over k, using the limits given in Ref. 71, the energy density in $ergs/cm^3$ of the saturated turbulence is given by

$$\frac{E^2_{turb}}{8\pi} = \int \frac{|E_k|^2}{8\pi}\, dk \sim \frac{1}{2}\, nmv^2 \quad .$$

Combining this with the above formula gives

$$\frac{E^2_{turb}}{8\pi} \sim 100\ (\Delta\lambda)^2 \quad .$$

The full width of HeII 4686 Å at this time is ~ 1.3 Å. This corresponds to a turbulent energy density of 169 $ergs/cm^3$. At this time, the electron temperature is known to be < 4 eV, while HeII 4686 Å is bright. As shown in Appendix B, this means that the temperature is $\gtrsim$ 3 eV. If the density is taken to be ~ 1×10^{15} cm^{-3}, the plasma energy density is ~ 9.6×10^3 $ergs/cm^3$, so the turbulent energy density is ~ 2% of the plasma energy density. The velocity of the current electrons, for this density, is ~ 1.9 x 10^7 cm/sec, which is of the same order as the electron thermal velocity.

Since the plasma is in contact with the walls, the energy losses are expected to be large. Once the turbulence has saturated, energy must be fed into the system to maintain the saturated level of turbulence, and make up for any losses. This energy is supplied by the toroidal current, which is observed to decay in time. To estimate this energy input, the current at this time is modeled as an LR circuit, with L/R ~ 38 μsec (see Fig. 27). It is necessary to compute the inductance of the system. This is done by modeling the plasma current channel as the inner conductor of a coax cable, and the main field winding as the outer conductor. Estimating the current channel as 3 cm in radius (this is one fourth of the wavelength of the fundamental of the compressional Alfven mode for the Tormac plasma parameters, as discussed earlier), the inductance of the circuit is ~ 21 μH. Using this, the energy given up by the current in the L/R time to the entire volume of plasma, taken as filling the vessel, is ~ 360 J. To check if this is a reasonable estimate, the loss of the energy of the ions is estimated as

$$P_i \sim \frac{n_i T_i \text{ (Volume)}}{\tau_i} \sim \frac{13\text{J}}{5.9\ \mu\text{sec}} \sim 2.2\ \text{J}/\mu\text{sec} \quad ,$$

where P_i is the energy lost per time due to ambipolar losses to the walls, τ_i is the loss time ~ l/Cs, l is the length of the system, and C_s is the sound speed. P_e, the power loss for electrons, is

~ $3P_1$. The total power lost is ~ 8.8 J/μsec. That these two estimates roughly agree is consistent with the experimental observation that the temperature remains ~ 3 eV. The resistivity of the plasma inferred from the above measurements and assumptions, ~ 0.18 ohm-cm, is larger than the classical Spitzer resistivity, ~ 9×10^{-3} ohm-cm, as would be expected for such an effect.

For comparison, the energy density of the thermal fluctuations is ~ 0.4 ergs/cm³ and the energy density,

$$\frac{\langle E_H\rangle^2}{8\pi} ,$$

of the theoretical Holtsmark fields is ~ 59 ergs/cm³. The Holtsmark fields are ~ 10 kV/cm, while the turbulent fields are $\gtrsim$ 20 kV/cm. These field magnitudes, while significant from the point of view of atomic physics, are within the limit of weak plasma turbulence, $e\phi < T$. In the Tormac plasma, this limit is

$$E_{max} \approx \frac{T}{e\lambda_D} \approx 165 \text{ kV/cm}.$$

This turbulence will tend to heat up the electrons. However, the losses increase as the temperature increases, and the energy is lost along the open lines. The electron temperature tends to remain constant. The current itself is unlikely to be carried as modeled above. It is not expected to be in the form of a beam of electrons. Since the driving electric field is in the direction of the current, it cannot generate a beam having an $\underline{E} \times \underline{B}$ velocity in the toroidal direction. Runaway electrons are not expected to be confined for very long due to the rapid penetration of the open magnetic field lines into the plasma. In addition, other experiments have suggested that such currents in a partially ionized gas tend to become striated.[59] This would tend to spread out the turbulence, and hence the broadening. Large widths are seen over the entire vessel. The plasma current Rogowski belt measures only net current. The field directions and the freezing in of the current would tend to produce currents in opposite directions, so that the actual local current density in the plasma is probably greater than the average amount.

Currents are known to generate other kinds of turbulence, in addition to the Langmuir case described above. Another example is ion-acoustic turbulence. These modes are expected to be highly damped in the bulk plasma, since $T_e \sim T_i$. However, in the vicinity of the current, T_e is expected to be larger than T_i, if only by a small amount. Therefore, near the current, ion-acoustic modes can exist. The intensity and spectral distribution of the modes are given by[71]

$$E_k^2 \sim \frac{M_i n C_s^2 \lambda_D^2}{k} \quad ,$$

where C_s is the sound speed, and n is the density of the electrons. The full width at half maximum in Å of a spectral line due to these fields is given by[71]

$$\Delta\lambda \sim 0.024 \left[n_e T_e \frac{T_e}{T_i} \frac{V_o}{V_e}\right]^{1/2} ,$$

where T_e and T_i are in ergs, and V_o is the directed velocity of the electrons. These quantities are not known in the vicinity of the current. However, for a density of 1 x 10^{15} cm^{-3}, and an electron and ion temperature of 3 and 2 eV, respectively, the calculated half widths are between 0.5 and 2Å, for reasonable values of V_o/V_e.

The toroidal plasma current is, therefore, capable of producing anomalously broad Gaussian HeII 4686 Å lines after cusp peak. Hβ at this time is less bright than during preionization and cusp rise, and the data are subject to photon noise. However, at small major radius, where Hβ is brightest, lines have been found having widths $\gtrsim$ 3 Å. These widths are what would be expected from Holtsmark broadening, at the density at this location. As mentioned earlier, the width of Hβ is dominated by quasistatic broadening, and impact broadening, such as due to this turbulence, has little effect on the width. The ion-acoustic turbulence in Tormac may have frequency components in the quasistatic regime. However, Hβ is unlikely to be emitting in the vicinity of the current where the temperature is $\gtrsim$3 eV, and, thus, does not exhibit any effects due to the turbulence. The satellites that are produced by impact broadening are spread out due to the frequency spread of the turbulence. The low light amplitude and consequent photon noise, together with the instrument function and channel separation of the polychromator, make observation of the satellites difficult. Other lines such as OII 4705 Å and HeI lines are not subject to the linear Stark effect, and do not display this behavior.

(3) T V

T V does not exhibit oscillations in the magnetic field. Since the magnitude of the field is lower than in T IV, and the rise time longer, it is not surprising that compressional Alfven modes are not launched by the rise of the cusp field. This observation is supported by the fact that the two regions of broadening behavior of HeII 4686 Å found in T IV are not observed in T V. The broadening does not exhibit the sharp peak found in T IV, but it does resemble the post cusp peak broadening found in T IV. The net toroidal plasma current in T V is greater than that in T IV, and is expected to play a larger role in the broadening of HeII 4686 Å. The broadening is found to vary as the net plasma current varies (Fig. 57). Therefore, the broadening seen in T V is explained by the turbulence mechanism used to explain the post cusp peak broadening in T IV. One difference is that more neutrals are present in the larger device, and provide an additional loss mechanism. The current oscillates in time due to the oscillating preionizer, but where this current is located in the plasma, and what fraction it is of the total plasma current is not known. The decay rate of the current is larger here than in T IV due to the larger size of the device. Without knowing the details of the current structure, it is hard to assess the effect of the larger current on HeII 4686 Å. However, the width is determined by the energy density of the turbulence, which is determined by the velocity and density of the current electrons. Since the plasma parameters are similar in both devices, the broadening is expected and is observed to be similar.

D. Computer Simulation

The Tormac start-up has been studied using two computer models. These will now be briefly discussed.

1) A 2-D single fluid resistive MHD code has been written and run by A. Aydemir and C. K. Chu. It uses classical resistivity and heat conductivity. The following are found:

a) The plasma does not implode to the minimum-B position.

b) Implosion is over in 2.5 μsec, and the plasma does not implode evenly.

c) The plasma then expands toward the inner wall and along the open field lines.

d) By 8 μsec after cusp discharge, most of the plasma is near the inner wall, and along a narrow strip at the midplane.

e) During the initial part of the cusp rise, there exist closed poloidal field lines due to the toroidal plasma current. They open up at a rate faster than expected from resistive diffusion. In some cases, no closed lines exist after 3 μsec into the cusp rise.

These results tend to agree with the experimental measurements. The interferometer shows the plasma near the inner wall and not compressed at the minimum-B position. Magnetic probes show the poloidal lines quickly penetrating the plasma.

2) A hybrid code, run by M. C. Vella at the author's request, was used to model Tormac start-up.[83] It treats the electrons as a

fluid, and treats the ions as particles. The individual orbits of the ions in the self-consistently determined electric and magnetic fields are followed. Possible turbulence effects during start-up are investigated. The following are found:

a) It takes ~ 1.5 μsec after cusp discharge for anything to happen for parallel bias case.

b) For reversed bias, it takes ~ 2-2.5 μsec for events to start.

c) The cusp field is seen to sweep up particles in both cases, though the density is more peaked and more particles are swept up in reversed bias case. Peak densities in the parallel bias case are ~ 3 x 10^{16} cm^{-3}, while in the reversed bias case they are ≳ 5 x 10^{16} cm^{-3}.

d) In the parallel bias case, toroidal field oscillations are seen, having magnitude up to 1 kG. Density oscillations are also seen.

e) In the reversed bias case, very small, if any, oscillations are apparent, either in magnetic field or density.

f) Electron and ion temperatures are ≲ 20 eV for both cases.

g) The effect of the turbulence is very small. Three instabilities are included: ion acoustic, modified two stream, and Buneman. Neither the ion acoustic nor Buneman instabilities are detected. The modified two stream instability is seen, but the electric field levels are very small, ≲ 120 V/cm.

h) The same general results are found for T V. Oscillations appear in the toroidal field and in the density for parallel bias.

Qualitative agreement is found between the hybrid code and the experiment. Oscillations in toroidal field and density are seen in the parallel bias case in T IV in both simulation and experiment. Much less oscillation is seen in the reversed bias case. Temperatures predicted by the simulation are higher than those observed experimentally. This would tend to turn off the Buneman instability. The densities given by the code cannot be verified by experiment, due to the line of sight nature of the interferometer measurement. The behavior of T V does not agree with the simulation. No oscillations at all are seen contrary to the code.

Because of the oscillations, the parallel bias runs developed numerical problems before cusp peak. The reversed bias case ran much longer. No times after cusp peak were simulated.

V. CONCLUSIONS

The Tormac plasma in T IV and T V has been studied using a variety of diagnostics. A consistent picture has emerged. The plasma is partially ionized, ~ 50%, by the preionization bank. The cusp field further ionizes the plasma to ≳ 90%, and moves it toward the inner wall. Exclusion of the main confinement magnetic field is not maintained for more than 2 μsec, and in T V, no exclusion of the toroidal field is observed at all. No thin sheath is found, and the open magnetic field lines do not remain separated from the bulk plasma. The electron temperature, as measured by Thomson scattering, is < 10 eV. Conditions are such that the electrons would quickly drain any ion energy, forcing the ion temperature to be similar to the electron temperature. Therefore, the Tormac concept has not been set up in these experiments.

Spectroscopy has been used as an ion temperature diagnostic by interpreting the widths of the observed Gaussian HeII 4686 Å spectral lines as determined by thermal Doppler broadening. This gives results which are inconsistent with the picture inferred from the other diagnostics. The behavior of the widths of HeII 4686 Å can be divided into two regions in time in T IV: 1) Large widths > 2 Å, corresponding to an ion temperature > 100 eV, are observed during the rise of the cusp, and decay quickly before the peak; 2) widths ~ 1.3 Å, corresponding to ~ 50 eV, are seen to last long after cusp peak, decaying with a time constant of ~ 50 μsec. An impurity line, OII 4705 Å, found in T IV has similar behavior. In T V, smaller widths are found, ~ 80 eV peak in temperature, and behave as the post cusp peak behavior found in T IV.

An explanation of the widths found during cusp rise in T IV has been suggested. Ion motion associated with compressional Alfven modes, known to be excited by the cusp rise, causes additional broadening of the line by the Doppler effect. Due to the finite temperature of the plasma, Gaussian-like lines are produced. Widths inferred from the magnitude of the toroidal field oscillation are similar to those observed.

Since the decay time of these modes is <15 μsec, another mechanism after cusp peak is necessary to broaden the lines. A net toroidal current of ~ 10 kA in T IV and 70 kA in T V is observed to last long after cusp peak. It has been shown that this current is capable of generating turbulence having electric fields which broaden the line by the Stark effect. This mechanism is assumed to be responsible for all of the broadening seen in T V, since no Alfven modes are observed.

ACKNOWLEDGEMENTS

This thesis has been one of the more major achievements of my existence. It has taken a lot of blood, sweat, toil, and tears -- not to mention cash from DOE and EPRI. There are many people I would like to thank for their help and kind advice, as well as a few around this lab I would just as soon forget. I shall let the latter group continue its well-deserved obscurity, while expressing my true indebtedness to the former.

It is conventional to indicate that those who have helped one write a thesis are too numerous to mention. That is not the case here. In fact, I can count all of those who so graciously helped me using only my fingers and toes. These include: Wulf B. Kunkel, my advisor (Wulf's advice and assistance have been truly invaluable), Ian Brown, John Coonrod, Benedict Feinberg, Martin Greenwald, Morton Levine, Booth Myers, Rory Niland, Philip Pincosy, Bruno Vaucher, and Michael Vella. I would also like to thank the technicians who showed me which was ~~the~~ business end of a screwdriver: Jim Galvin, Joe Moldener, Bob Peterson, and Gary Tabler. My thanks go to the TID Word Processing Center in Building 50 for typing this work. Finally, I would like to thank Karen Dolmatch Shaw, whose untimely but necessary move to Washington, D. C. provided the needed kick in the pants to finish this thesis in an approximately timely fashion.

This work was supported by the U. S. Department of Energy under contract No. W-7405-ENG-48.

APPENDIX A

Structure of HeII 4686 Å

This line arises from singly-ionized helium, which is hydrogen-like in structure. The transition is from $n = 4$ to $n = 3$, and the emitted photon has energy

$$\Delta E = 4(13.6)\left[\frac{1}{3^2} - \frac{1}{4^2}\right] = 2.64 \text{ eV} .$$

Each of these energy levels is split due to LS (Russel-Saunders) coupling, and, therefore, the HeII 4686 Å line actually consists of 13 fine structure components.[84] This is illustrated in Fig. A1. Table A1 gives the line positions and relative intensities of the 13 components, assuming the relative intensities are determined by a statistical population of the levels.[85]

Furthermore, each of these components are split by the Zeeman effect. The magnetic field causes each component to split into $(2j+1)$ components, symmetrically distributed about the $B = 0$ position. This energy shift is given by,

$$\Delta E = m_j \ \mu_B \ gB,$$

where ΔE = energy shift due to B,

m_j = magnetic quantum number associated with level j,

μ_B = Bohr magneton,

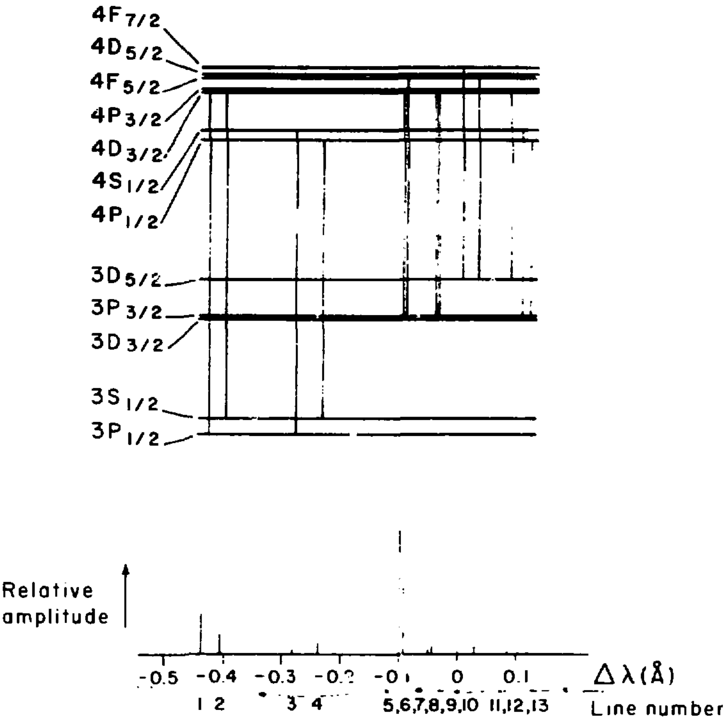

XBL 804-731

Fig. A1. Top: Schematic of the energy levels of the HeII ions showing the transitions contributing to the HeII 4686Å line.
Bottom: Relative amplitude of the 13 transitions contributing to HeII 4686Å vs Δλ, assuming a statistical population of the levels.

and

$$g = 1 + \frac{j(j+1) + s(s+1) - l(l+1)}{2j(j+1)} \quad ,$$

where j,s,l are the quantum numbers associated with that energy level. For the fields found in Tormac, $\Delta E \sim 1.7 \times 10^{-5}$ eV, which gives $\Delta\lambda \sim 0.03$ Å. Because the full width at half maximum of the lines from Tormac are >> 0.3 Å, the Zeeman effect is unimportant.

The n = 3 and n = 4 levels of the helium ion may also be split by the presence of an electric field, due either to the presence of charged particles or to collective effects in the plasma. The electric field removes the degeneracy of the sublevels and causes an energy shift proportional to the electric field strength.

Each of these sub-levels is subject to the Doppler effect. As seen in the discussion section, the full width at half maximum of a Doppler broadened line is given by

$$\Delta\lambda = 2^{3/2} (\ln 2)^{1/2} \lambda \sqrt{\frac{T}{M_i c^2}} \quad .$$

If the instrumental width of the polychromator is $\Delta\lambda_i$, and only Doppler broadening is important, then the intensity of the HeII 4686 Å line is given by,

$$I(\lambda) = \sum_{n=1}^{13} A_n \exp\left[-\frac{(\lambda-\lambda_n)^2 \, 4 \ln 2}{(\Delta\lambda)^2 + (\Delta\lambda_i)^2}\right] \quad ,$$

where A_n = amplitude of the n^{th} fine structure component, and λ_n = wavelength of the n^{th} fine structure component. For the widths seen in this experiment, fine structure is unimportant. Furthermore, since the instrumental broadening is ~ 0.6 Å, and the polychromator channel separation is 0.3 Å, the fine structure is never a factor, and is ignored in this report.

Table A1

Line number	Transition 3–4	Line positions λ_n relative to No. 9 in Å	Relative intensity A_n (statistical)
1	$^2P_{1/2}-^2D_{3/2}$	-0.427	21.27
2	$^2S_{1/2}-^2P_{3/2}$	-0.397	11.12
3	$^2P_{1/2}-^2S_{1/2}$	-0.280	1.11
4	$^2S_{1/2}-^2P_{1/2}$	-0.236	5.56
5	$^2D_{3/2}-^2F_{5/2}$	-0.100	70.00
6	$^2P_{3/2}-^2D_{5/2}$	-0.100	38.25
7	$^2D_{3/2}-^2P_{3/2}$	-0.047	0.13
8	$^2P_{3/2}-^2D_{3/2}$	-0.046	4.25
9	$^2D_{5/2}-^2F_{7/2}$	0	100.00
10	$^2D_{3/2}-^2F_{5/2}$	+0.027	5.00
11	$^2D_{5/2}-^2P_{3/2}$	+0.060	0.63
12	$^2P_{3/2}-^2S_{1/2}$	+0.102	2.22
13	$^2D_{3/2}-^2P_{1/2}$	+0.114	1.13

APPENDIX B

Plasma Equilibrium Models Applied to Tormac

Plasma models are used to relate the populations of various quantum levels to the plasma parameters. Each model has its own set of assumptions and regions of validity, and care must be taken to apply the correct model to the problem.

Local Thermal Equilibrium (LTE): This is an equilibrium model of the plasma in which all processes are balanced by their inverse processes. Since the plasma is considered optically thin (Appendix C), the emitted light goes through the plasma without interaction, and is lost. Therefore, one condition for the LTE model to be valid is that the collisional processes dominate the photon processes, since then the important processes are indeed balanced by their inverse processes. This condition may be written as[60,62,63]

$$n_e \geq 1.72\times10^{14}\ T_e^{1/2}\ X^3,$$

where n_e is the electron density in cm^{-3}, T_e is the electron temperature in eV, and X is the energy of the emitted photon in eV. For the HeII 4686 Å line, this criterion gives

$$n \geq 3.2\times10^{15}\ cm^{-3}$$

for $T_e = 1$ eV. Other validity criteria may be found in Reference 60.

If LTE is valid, the equilibrium may be described by the following:

$$\frac{n(z,p)}{n(z,q)} = \frac{g(z,p)}{g(z,q)} e^{-[E(p) - E(q)]/T_e}$$

and

$$\frac{n(z+1,1)\, n_e}{n(z,1)} = \frac{g(z+1,1)\, 2}{g(z,1)} \left(\frac{2\pi\, mT_e}{h^2}\right)^{3/2} e^{-(X-\Delta)/T_e} ,$$

where $n(z,p)$ = density of ions in ionization state z and in quantum level p,

$g(z,p)$ = degeneracy of level p of ionization state z,

$E(p)$ = energy of level p,

T_e = electron temperature in energy units,

n_e = electron density,

X = ionization energy of ion of charge z,

Δ = lowering of ionization energy due to presence of plasma,[60,62]

m = electron mass,

and $p = 1$ indicates the ground state.

These equations are solved for the Tormac plasma (80% H_2, 20% He) for various initial fill pressures. Figure B1 shows the ground state densities of the various species as a function of electron temperature for 30 mTorr fill pressure. Figure B2 shows the density of the $n = 4$ level of hydrogen and ionized helium as a function of electron temperature (Hβ 4861 Å and HeII 4686 Å originate from these levels). Note that this model indicates that HeII 4686 Å has maximum intensity

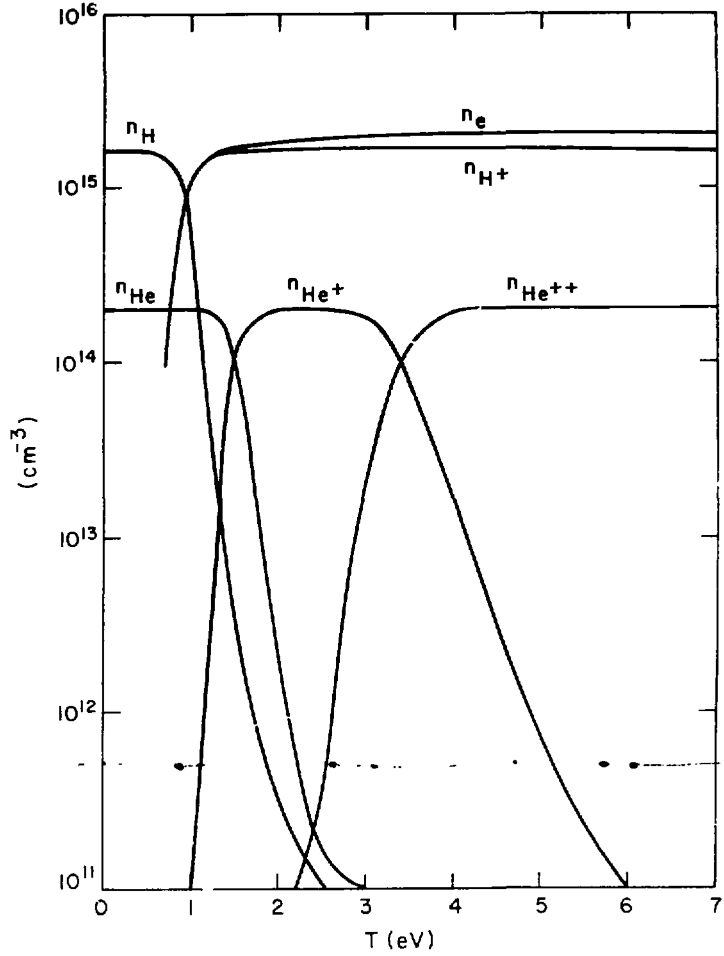

XBL 804-733

Fig. B1: Ground state populations of various species vs temperature for 30 mTorr fill pressure in LTE.

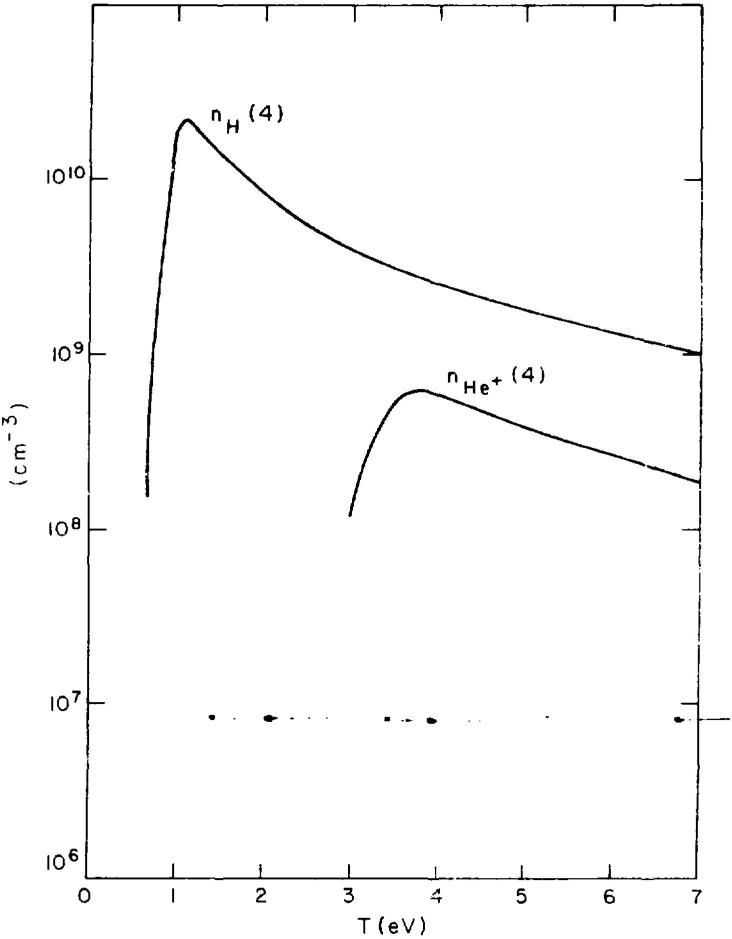

XBL 804-735

Fig. B2: Populations of n = 4 level of hydrogen and ionized helium vs temperature for 30 mTorr fill pressure in LTE.

for T_e near 4 eV. From the validity criterion, these numbers may not be correct for a fill pressure of 30 mTorr, although the general trends are certainly correct.

Steady State Corona Equilibrium: In this model, processes are not balanced by their inverse processes. Equilibrium between states of different ionization levels is determined by a balance between electron collisional ionization and radiative recombination. This model is valid at lower densities than LTE, for then three body recombination ($A^+ + e + e \rightarrow A + e$) becomes negligible compared to radiative recombination ($A^+ + e \rightarrow A + h\nu$). Within a given ionization level, electron collisional excitation is balanced by spontaneous emission. This equilibrium is then described by

$$\frac{n(z,p)}{n(z,1)} = \frac{n_e\, X(T_e,1,p)}{\sum\limits_{q<p} A(p,q)} \quad ,$$

and

$$\frac{n(z+1,1)}{n(z,1)} = \frac{S(T_e,z)}{\alpha(T_e,z+1)} \; ,$$

where $X(T_e,1,p)$ = excitation coefficient - number of electron excitation collisions in 1 cm^3 per second from the ground state to state p in the same ionization level,

$A(p,q)$ = Einstein spontaneous decay coefficient - number of decays per second from state p to state q,

$S(T_e,z)$ = ionization coefficient - number of electron ionization collisions in 1 cm^3 per second from the ground state of level z to the ground state of level (z+1),

and $\alpha(T_e,z+1)$ = radiative decay coefficient - number of decays in 1 cm^3 per second from the ground state of level (z+1) to the ground state of level z.

Values of these rate coefficients are discussed in Reference 63. Figure B3 shows the ground state densities of the various species of the 30 mTorr Tormac plasma as a function of electron temperature. Figure B4 shows the n = 4 level of ionized helium as a function of T_e. Note that in this model, this peaks at 7 eV, as opposed to 4 eV in the LTE case. In this model, the ground state populations are much greater than the populations in the excited levels. As a result, no ionization takes place from an excited level - only from the ground state. This model is valid for low densities and high temperatures.

In the collisional radiative model,[86,87] the rate equations themselves are solved; the time derivatives are not, in general, set to zero and ionization from the excited levels is included.[60,62,63] More physics is included in this model and, therefore, the system becomes more difficult to solve. This has not been done, although this is certainly the correct model for Tormac. The LTE and corona models bracket the Tormac case, and are more easily solved. They show that, in equilibrium, singly ionized helium becomes doubly ionized between 4 and 8 eV. This says that in equilibrium HeII 4686 Å light

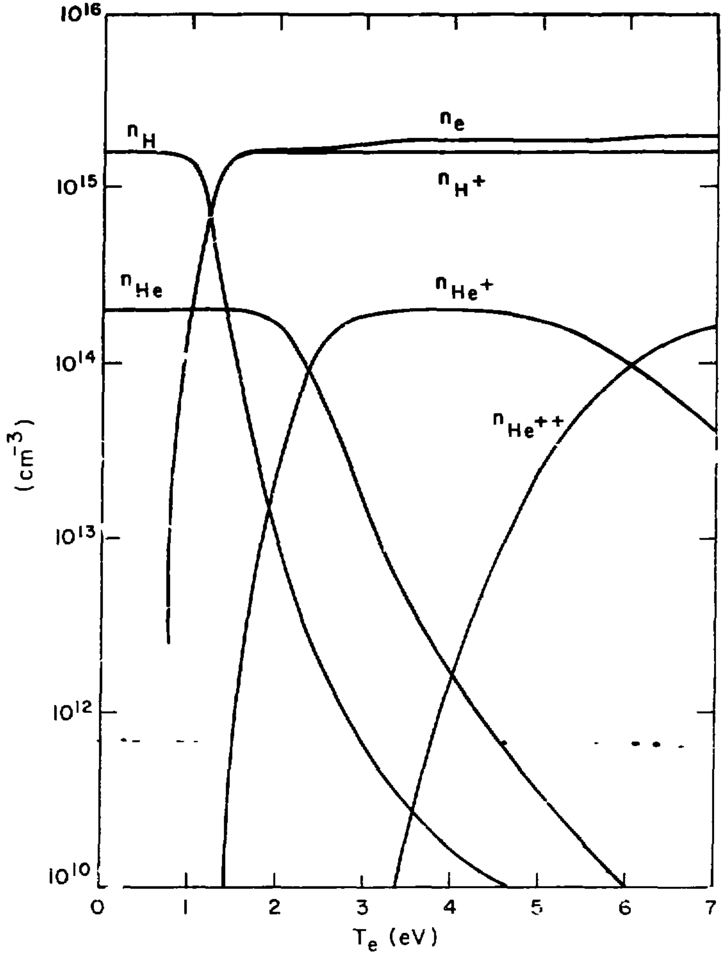

XBL 804-737

Fig. 33: Ground state populations for various species vs electron temperature for 30 mTorr fill pressure in corona equilibrium.

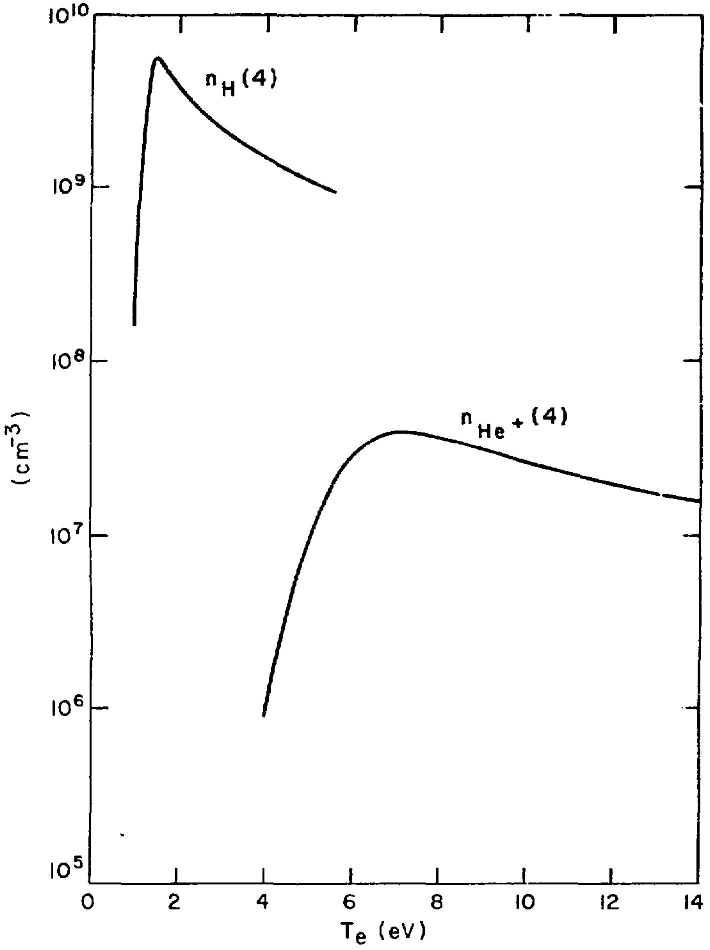

XBL 804-734

Fig. B4: Populations of n = 4 level of hydrogen and ionized helium vs electron temperature for 30 mTorr fill pressure in corona equilibrium.

is useful as a diagnostic for $T_e < 10$ eV. At higher temperatures, it is certainly burned out, and any light seen along a line of sight comes from lower temperature material, presumably located outside the region of interest.

APPENDIX C

Light Intensity and Optical Depth

Define the total absorption coefficient at wavelength λ and position x as[60]

$$k(\lambda,x) = \sigma^a_{mn} N_n(x) - \sigma^i_{nm} N_m(x),$$

where σ^a_{mn} = absorption cross section = $\pi r_o f_{mn} \lambda^2 L(\lambda,x)$,

σ^i_{nm} = induced emission cross section =

$$\frac{g_n}{g_m} \sigma^a_{mn} \quad ,$$

m,n = upper, lower state,

f_{mn} = absorption oscillator strength,

r_o = classical electron radius =

$$\frac{e^2}{mc^2}$$

$N_n(x)$ = density of particles in state n at position x,

g_n = degeneracy of level n,

and $L(\lambda,x)$ = normalized line shape factor.

Note that this not only takes into account the absorption of the photon propagating through the plasma, but also the induced emission of other photons as a result of this propagation. $k(\lambda,x)$ may be written as

$$k(\lambda,x) = \pi r_0 \; f_{mn} \; \lambda^2 L(\lambda,x) \frac{g_n}{g_m} N_m(x) \left[\frac{g_m \, N_n(x)}{g_n \, N_m(x)} - 1 \right] \quad .$$

The optical depth may then be defined as

$$\tau(\lambda,x) = \int_x^L k\,(\lambda,x')dx' \;,$$

where L is the edge of the plasma near the detector, and x is some position inside the plasma; i.e., optical depth is the integral of the total absorption coefficient along the path of the light, extending back into the plasma from the detector, and is a dimensionless number. The larger $\tau(\lambda,x)$ is, the larger the role absorption plays in the radiation transfer process, and, therefore, the more complicated the problem becomes. This is because the absorption coefficient depends on the population of the excited level, which depends to some extent on the absorption of the radiation. For very large $\tau(\lambda,x)$, the measured intensity approaches that of a black body.

The general radiation transfer equation is given by[60]

$$\frac{d}{dx} I(\lambda,x) = \varepsilon(\lambda,x) - k(\lambda,x) \; I(\lambda,x),$$

where $I(\lambda,x)$ = intensity (power per area, solid angle, and wavelength interval) at wavelength λ and position x,

and $\varepsilon(\lambda,x)$ = emission (power per volume solid angle, and wavelength interval) at wavelength λ and position x.

The general solution of this equation in terms of optical depth is given by

$$I(\lambda,L) = \int_{x_0}^{L} \varepsilon(\lambda,x)\, e^{-\tau(\lambda,x)}\, dx,$$

where $I(\lambda,L)$ is the intensity measured at the detector $(x = L)$, x_0 is the far edge of the plasma, the integral is over the light path, and it is assumed that no light enters the plasma from an external source. For the case of optically thin plasma ($\tau \ll 1$), to lowest order, the measured intensity is

$$I(\lambda,L) = \int_{x_0}^{L} \varepsilon(\lambda,x)\, dx \ .$$

To ensure that the Tormac plasma is optically thin, an LTE model of the plasma is assumed (Appendix B). This is done for two reasons: 1) this is the easiest case to do, and 2) this is the worst case in the sense that if the plasma is optically thin in this model, then it will be optically thin in the corona model, and also in the true model, which is bracketed by these models. For LTE,

$$\frac{N_m(x)}{N_n(x)} = \frac{g_m}{g_n} \exp\left[\frac{-hc}{\lambda_0 T(x)}\right] \quad ,$$

where λ_0 = wavelength of line interest =

$$\frac{hc}{E_m - E_n} ,$$

and E_m = energy of level m. For a homogeneous LTE plasma of length ℓ, the optical depth is given by

$$\tau(\lambda) = 8.85\mathrm{x}10^{-13} \; \frac{g_n}{g_m} \; \lambda^2 \; f_{mn} \; L(\lambda) N_m \left[\exp\left(\frac{hc}{\lambda_o T}\right) - 1\right] \ell \quad .$$

If the line in question is assumed to be Doppler broadened,

$$L(\gamma) = \frac{c}{(2\pi)^{1/2} V_{th} \gamma_o} \exp\left[- \frac{c^2}{\gamma_o^2} (\gamma - \gamma_o)^2 / 2 \; V_{ch}^2\right]$$

where $V_{th} = \left(\frac{T}{M_i}\right)^{1/2}$.

The line center has the largest optical depth, so the calculation will be done for the line center. The optical depth at line center may then be written as

$$\tau(\lambda_o) = 3.53\mathrm{x}10^{-13} \; \frac{c}{V_{th}} \; \frac{g_n}{g_m} \; \lambda_o f_{mn} N_m \left[\exp\left(\frac{hc}{\gamma_o T}\right) - 1\right] \ell \quad .$$

For HeII 4686 Å,

V_{th} = $4.95\mathrm{x}10^5 \; T^{1/2}$ cm/sec,

f_{mn} = 0.842

$g_n = g_3$ = 18,

$g_m = g_4$ = 32,

and T = ion temperature in eV.

Therefore, the optical depth per length of plasma for HeII 4686 Å is given by

$$\frac{\tau}{\ell} = \frac{4.75\times10^{-13}}{T^{1/2}} \quad N_4(T)\left[\exp\left(\frac{2.64}{T}\right) - 1\right] \quad .$$

For Hβ 4861 Å,

$v_{th} = \quad 9.9\times10^5\ T^{1/2}$ cm/sec,

$f_{mn} = \quad 0.1193$,

$g_n = g_2 = \quad 8$,

and $\quad g_m = g_4 = \quad 32$.

Therefore, the optical depth per length of plasma for Hβ 4861 Å is given by

$$\frac{\tau}{\ell} = \frac{1.55\times10^{-14}}{T^{1/2}} \quad N_4(T)\left[\exp\left(\frac{2.56}{T}\right) - 1\right] \quad .$$

Figure C1 shows the optical depth per length of a 30 mTorr Tormac plasma for HeII 4685 Å and Hβ 4861 Å, assuming a homogeneous LTE plasma, and assuming the line shape is determined solely by Doppler broadening. For this case the plasma is definitely optically thin. This analysis was also done for fill pressures out to 500 mTorr, and the plasma was found to be optically thin to these two spectral lines. Of course, at such high fill pressures as 500 mTorr, if there were any substantial compression, the plasma would not be optically thin. However, for $\lesssim$50 mTorr fill pressure and Tormac type density compression, the plasma is always optically thin.

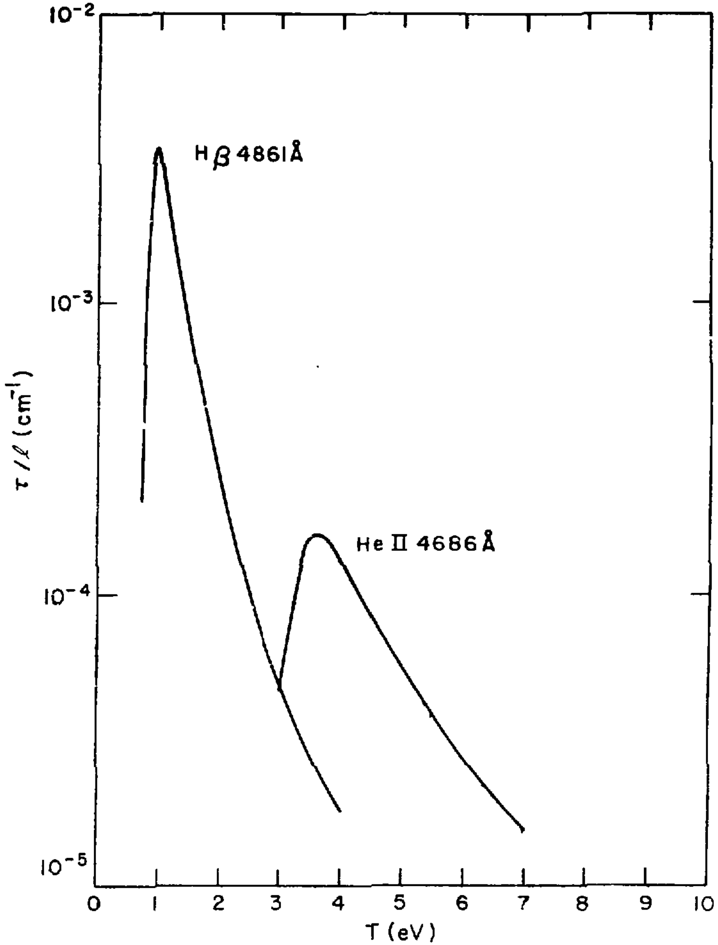

XBL 804-736

Fig. C1: Optical depth per length of a 30 mTorr plasma vs temperature for HeII 4686Å and Hβ 4861Å, assuming LTE and Doppler broadening.

APPENDIX D

Line Shape

The total power radiated at frequency ω per frequency interval for spontaneous electric dipole emission is given by[60,78]

$$P(\omega) = \frac{4}{3}\frac{\omega^4 e^2}{c^3} \sum_{m,n} \left|\langle n|\underline{r}|m\rangle\right|^2 \delta(\omega-\omega_{mn})\ \rho_m,$$

where

$$\omega_{mn} = \frac{E_m - E_n}{\hbar} \quad ,$$

ρ_m is the probability of occurrence of initial state m, and $\underline{r}$ is the position vector of the radiating electron. The average over initial states and sum over final states is done to include all contributions to the line. Over the spectral line, ω^4 remains approximately constant, so the frequency dependence is usually separated as follows:

$$P(w) = \frac{4}{3}\ \frac{\omega^4 e^2}{c^3}\ L(\omega),$$

where $L(\omega) = \sum_{m,n} \left|\langle n|\underline{r}|m\rangle\right|^2 \delta(\omega-\omega_{mn})\rho_m$. $L(\omega)$, the line shape, contains the fast ω dependence. Define the Fourier transform of the line shape as

$$\phi(\tau) = \int_{-\infty}^{\infty} d\omega e^{-i\omega\tau} L(\omega) = \sum_{m,n} e^{-i\omega_{mn}\tau} \left|\langle n|\underline{r}|m\rangle\right|^2 \rho_m \ . \qquad (1)$$

Since $L(\omega)$ is real, $\phi^*(\tau) = \phi(-\tau)$, so the line shape may be written as

$$L(\omega) = \frac{1}{2\pi} \int_{-\infty}^{\infty} d\tau e^{i\omega\tau} \phi(\tau) = \frac{1}{\pi} \ \mathrm{Re}\left[\int_{0}^{\infty} d\tau e^{i\omega\tau} \phi(\tau)\right] \quad .$$

The purpose of introducing $\phi(\tau)$ is that it has a simple interpretation; it is the autocorrelation function of the emitted light amplitude. Furthermore, it is easier to work with than the formula for $L(\omega)$. Once $\phi(\tau)$ is obtained, $L(\omega)$ is computed using the above formula.

Define $A(t)$ as the amplitude of the emitted light, and $a(\omega)$ as its Fourier transform:

$$a(\omega) = \frac{1}{2\pi} \int_{-\infty}^{\infty} dt \ e^{i\omega t} A(t) \ .$$

By manipulation, autocorrelation of the light amplitude =

$$\langle A(t+\tau)A^*(t)\rangle = \langle A(t)A^*(t-\tau)\rangle$$

$$= \int d\omega \int d\omega' \ e^{i\omega' t - i\omega(t+\tau)} \ \langle a(\omega)a^*(\omega')\rangle \quad ,$$

and

$$\langle a(\omega)a^{*}(\omega')\rangle = \frac{1}{2\pi}\int_{-\infty}^{\infty} d\tau\ \langle A(t)A^{*}(t-\tau)\rangle^{i\omega\tau}\delta(\omega-\omega') \quad ,$$

where the brackets indicate a statistical average, and it is assumed that the process is stationary. From the theory of stochastic processes, the Fourier transform of the correlation function of the amplitude of the stochastic variable is the spectral power $P(\omega)$, the power per frequency interval. Using the above expressions,

$$\langle a(\omega)a^{*}(\omega')\rangle = P(\omega)\ \delta(\omega-\omega'),$$

and $\langle A(t+\tau)A^{*}(t)\rangle = \int d\omega e^{-i\omega\tau}P(\omega) = \phi(\tau),$

where the constant factors have been ignored.

As an example, consider Doppler broadening. Define the phase shift of the light amplitude between times t_1 and t_2 due to motion or collision as

$$\theta(t_2,t_1) = \int_{t_1}^{t_2} \Delta\omega(t')\ dt' \quad ,$$

where $\Delta\omega$ is the frequency change due to the process in question — here the motion of the emitter. The light amplitude may be written as

$$A(t) = e^{-i\omega_0 t\ -\ i\theta(t,0)}$$

Therefore, $\phi(\tau) = \langle A(t+\tau)A^{*}(t)\rangle = \langle e^{-i(\omega_0\tau+\theta(t+\tau,t))}\rangle.$

For Doppler, $\Delta\omega = \omega_0 \frac{v}{c}$, so that

$$\theta(t+\tau,\ t) = \omega_0 \int_t^{t+\tau} \frac{v(t')}{c}\ dt' \quad .$$

If one assumes that the time τ is $<< \tau_{mfp}$, the mean time between collisions, then the probability of a collision in time τ is negligible, and $v(t')$ is constant. Therefore,

$$\phi(\tau) = \int_{-\infty}^{\infty} dv\ f(v)\ \ e^{-i(\omega_0+\omega_0 \frac{v}{c})\tau} \quad ,$$

where $f(v)$ is the velocity distribution function of the emitters. The line shape is then given by

$$L(\omega) = \frac{1}{2\pi} \int_{-\infty}^{\infty} d\tau\ e^{i\omega\tau} \int_{-\infty}^{\infty} dv\ f(v)\ e^{-i(\omega_0 + \omega_0 \frac{v}{c})\tau}$$

$$= \int_{-\infty}^{\infty} dv\ f(v)\ \delta\ (\omega-\omega_0 - \omega_0 \frac{v}{c}) \quad .$$

This agrees with the line shape formula presented in the discussion section. Note that this analysis indicates an additional validity criterion: $\tau << \tau_{mfp}$. Since $\tau \sim (\omega_{1/2})^{-1}$, where $\omega_{1/2}$ is the width of the line, this criterion becomes:

$$\lambda_{mfp} >> \lambda_0 \ ,$$

where λ_{mfp} is the mean free path of the emitters, and λ_0 is the wavelength of the emitted light. This condition is easily met in Tormac.

Stark calculations[60-62,78] are much more involved in that the light amplitude correlation function cannot be written down as easily as for the Doppler effect. Equation 1 is usually rewritten as

$$\phi(\tau) = \mathrm{Tr}\,[\underline{r}\,T^{+}\,\underline{r}\,T\,\rho] ,$$

where T is the time development operator of the system, ρ is the density matrix, and Tr indicates the trace. The problem is then simplified by making the classical path approximation, which reduces the problem to the solution of the Schrodinger equation for the emitter wave functions. The perturbing electric fields are due to perturbers, which are assumed to be moving along classical paths.

The problem is then simplified further by breaking the problem into two extreme cases:

1) Quasistatic Broadening - where the autocorrelation time of the light amplitude is much less than the collision time. The motion of the perturbers is unimportant. The line width is calculated by assuming the perturbers are at fixed positions and solving for $\phi(\tau)$. This gives a spectrum of sharp lines. Then, a statistical average over the perturber positions is performed, and a broadened line is produced.

2) Impact Broadening - where the autocorrelation time of the light amplitude is much longer than the collision time. Many collisions are necessary to perturb the emitter. The broadening is calculated by adding a non-hermitian interaction to the atomic Hamiltonian, and

solving the Schrodinger equation for the time evolution operator. This is then used to calculate $\phi(\tau)$. For details, the reader is referred to the literature.[61]

REFERENCES

1. S. I. Braginskii and B. B. Kadonstev, Plasma Physics and the Problems of Controlled Thermonuclear Reactions, Vol. 3, Pergamon Press (1959).
2. J. Berkowitz, H. Grad, and H. Rubin, Proc. 2nd U. N. Conf. on Peaceful Uses of Atomic Energy, Vol. 31, United Nations, Geneva (1958).
3. I. J. Spalding, Adv. in Plasma Physics, Vol. 4, ed. Simon and Thomson, Interscience (1971).
4. J. Berkowitz, Proc. 2nd U. N. Conf. on Peaceful Uses of Atomic Energy, Vol. 31, United Nations, Geneva (1958).
5. J. Berkowitz, K. O. Frederichs, H. Goertzel, H. Grad, J. Killeen, and E. Rubin, Proc. 2nd U. N. Conference on Peaceful Uses of Atomic Energy, Vol. 31, United Nations, Geneva (1958).
6. H. Grad and H. Rubin, Proc. 2nd U. N. Conference on Peaceful Uses of Atomic Energy, Vol. 31, United Nations, Geneva (1958).
7. M. A. Levine, A. H. Boozer, and W. B. Kunkel, Proc. of the High Beta Workshop, Los Alamos, New Mexico (1975).
8. M. G. Haines, Nucl. Fusion 17, 811 (1977).
9. M. A. Levine, A. H. Boozer, G. Kalman, and P. Bakshi, Phys. Rev. Lett. 28, 1323 (1972).
10. A. H. Boozer and M. A. Levine, Phys. Rev. Lett. 31, 1287 (1973).
11. N. T. Gladd, Y. Goren, C. S. Lin, and R. C. Davidson, Phys. Fluids 20, 1876 (1977).
12. T. J. M. Boyd and J. J. Sanderson, Plasma Dynamics, Barnes and Noble, New York (1969).

13. G. Kalman and P. Bakshi, Bull. Am. Phys. Soc. 17, 1040 (1972).

14. J. H. Hammer, Ph. D. Thesis, Lawrence Berkeley Laboratory report number LBL-8748 (1979).

15. H. Grad, Phys. Fluids 9, 2472 (1966).

16. S. Hamasaki, R. C. Davidson, N. A. Krall, and P. C. Liewer, Nucl. Fusion 14, 27 (1975).

17. F. H. Coensgen, W. F. Cummins, B. G. Logan, A. W. Molvik, W. E. Nexsen, T. C. Simonen, B. W. Stallard, and W. C. Turner, Phys. Rev. Lett. 35, 1501 (1975).

18. L. M. Zelenzi, Sov. J. Plasma Phys. 1, 319 (1975).

19. D. E. Baldwin, H. L. Berk, and L. D. Perlstein, Phys. Rev. Lett. 36, 1051 (1976).

20. N. A. Krall, Phys. Fluids 20, 311 (1977).

21. C. C. Gallagher, L. S. Combes, and M. A. Levine, Phys. Fluids 13, 1617 (1970).

22. C. C. Gallagher and M. A. Levine, Bull. Am. Phys. Soc. 18, 1295 (1973).

23. I. G. Brown, B. Feinberg, M. A. Levine, and R. A. Niland, Bull. Am. Phys. Soc. 22, 1067 (1977).

24. B. R. Myers and M. A. Levine, Bull. Am. Phys. Soc. 22, 1067 (1977).

25. I. G. Brown, B. Feinberg, W. B. Kunkel, M. A. Levine, R. A. Niland, R. S. Shaw, and B. G. Vaucher, Bull. Am. Phys. Soc. 24, 1086 (1979).

26. B. R. Myers, M. A. Levine, and P. A. Pincosy, Bull. Am. Phys. Soc. 24, 1087 (1979).

27. R. B. Howell and H. J. Karr, Phys. Fluids 19, 2012 (1976).

28. D. R. Matt and F. R. Scott, Phys. Fluids 15, 1047 (1972).

29. G. E. Georgiou and T. C. Marshall, Bull. Am. Phys. Soc. 24, 1108 (1979).

30. R. S. Shaw, J. Coonrod, M. Greenwald, M. A. Levine, B. R. Meyers, and M. C. Vella, Lawrence Berkeley Laboratory report number LBL-10218 (1980), to be published in Plasma Physics.

31. B. R. Myers, private communication.

32. R. H. Lovberg, in Plasma Diagnostic Techniques, ed. R. H. Huddlestone and S. L. Leonard, Academic Press, New York (1965).

33. M. A. Levine, I. G. Brown, and C. C. Gallagher, Lawrence Berkeley Laboratory report number LBL-3262 (1975).

34. M. Greenwald, Ph. D. Thesis, Lawrence Berkeley Laboratory report number LBL-8166 (1978).

35. J. W. Coonrod, Ph. D. Thesis, Lawrence Berkeley Laboratory report number LBL-8167 (1978).

36. I. G. Brown, B. Feinberg, W. B. Kunkel, M. A. Levine, R. A. Niland, R. S. Shaw, and B. G. Vaucher, Lawrence Berkeley Laboratory report number LBL-10586 (1980), to be published.

37. M. C. Vella and B. Feinberg, Lawrence Berkeley Laboratory report number LBL-7569 (1978).

38. M. A. Levine, Lawrence Berkeley Laboratory internal report number UCID-8038 (1978).

39. E. P. Butt, et al., 6th Conf. on Plasma Physics and Controlled Nuclear Fision, CN-33/E9.2, Tokyo (1974).

40. N. A. Krall and A. W. Trivelpiece, Principles of Plasma Physics, McGraw-Hill, New York (1973).

41. A. W. DeSilva and G. C. Goldenbaum, Plasma Diagnostics by Light Scattering, Part III of Methods of Experimental Physics, Vol. IX, Part A, Academic Press, New York (1970).

42. H. J. Kunze, in Plasma Diagnostics, Chap. 9, ed. W. Lochte-Holtgreven, North Holland, Amsterdam (1968).

43. J. Sheffield, Plasma Scattering of Electromagnetic Radiation, Academic Press, New York (1975).

44. R. E. Siemon, Appl. Opt. 13, 699 (1974).

45. P. H. Van Cittert, Z. Instr. 46, 557 (1926).

46. S. L. Leonard, in Plasma Diagnostic Techniques, Chap. 2, ed. R. H. Huddlestone and S. L. Leonard, Academic Press, New York (1965).

47. J. C. Sprott, Rev. Sci. Instrum. 37, 897 (1966).

48. J. C. Sprott, Univ. of Wisconsin report number PLP 88 (1966).

49. J. W. Coonrod, Lawrence Berkeley Laboratory report number LBL-4468 (1975).

50. M. A. Levine, Bull. Am. Phys. Soc. 17, 1040 (1972).

51. R. S. Shaw, B. R. Myers, and M. C. Vella, Lawrence Berkeley Laboratory report number LBL-9696 (1978).

52. M. A. Levine, Bull. Am. Phys. Soc. 21, 1048 (1976).

53. R. A. Niland, private communication.

54. M. A. Levine and C. C. Gallagher, Phys. Lett. 32A, 14 (1970).

55. C. C. Gallagher and M. A. Levine, Phys. Rev. Lett. 27, 1693 (1971).

56. C. C. Gallagher and M. A. Levine, Phys. Rev. Lett. 30, 897 (1973).

57. C. C. Gallagher and M. A. Levine, J. Quant. Radiat. Transfer 15, 275 (1975).

58. B. Feinberg, R. S. Shaw, B. G. Vaucher, and M. C. Vella, Lawrence Berkeley Laboratory report number LBL-10318 (1980), to be published.

59. R. D. Bengtson, V. P. Myerscough, T. L. Pittman, P. E. Phillips, and A. Sanchez, Plasma Physics 21, 139 (1979).

60. H. R. Griem, Plasma Spectroscopy, McGraw-Hill, New York (1964).

61. H. R. Griem, Spectral Line Broadening by Plasmas, Academic Press, New York (1974).

62. W. Lochte-Holtgreven, ed., Plasma Diagnostics, North Holland, Amsterdam (1968).

63. R. W. P. McWhirter, in Plasma Diagnostic Techniques, ed. R. H. Huddlestone and S. L. Leonard, Academic Press, New York (1965).

64. W. L. Wiese, in Plasma Diagnostic Techniques, ed. R. H. Huddlestone and S. L. Leonard, Academic Press, New York (1965).

65. R. M. Mersereau, Computer Graphics and Image Processing 1, 179 (1973).

66. R. A. Brooks and C. DiChiro, Phys. Med. Biol. 21, 689 (1976).

67. S. H. Autler and C. H. Townes, Phys. Rev. 100, 703 (1955).

68. W. W. Hicks, R. A. Hess, and W. S. Cooper, Phys. Rev. A 5, 490 (1972).

69. A. Sanchez and R. D. Bengston, Phys. Rev. Lett. 38, 1276 (1977).

70. G. Bekefi, C. Deutsch, and B. Yaakobi, Chap. 13 in Principles of Laser Plasmas, ed. G. Bekefi, John Wiley, New York (1976).

71. E. V. Lifshitz, Sov. Phys. JETP 26, 570 (1968).

72. S. P. Zagorodnikov, G. E. Smolkin, E. A. Striganova, and G. V. Sholin, Sov. Phys.-Doklady 15, 1122 (1971).

73. E. K. Zavoiskii, Yu. G. Kalinin, V. A. Skoryupin, V. V. Shapkin, and G. V. Sholin, Sov. Phys.-Doklady 15, 823 (1971).

74. G. V. Sholin, Sov. Phys.-Doklady 15, 1040 (1971).

75. L. P. Zakatov. A. G. Plakhov, V. V. Shapkin, and G. V. Sholin, Sov. Phys.-Doklady 16, 451 (1971).

76. W. S. Cooper and R. A. Hess, Phys. Rev. Lett 25, 433 (1970).

77. W. W. Hicks, Ph. D. Thesis, Lawrence Berkeley Laboratory report number LBL-2470 (1972).

78. M. Baranger, in Atomic and Molecular Processes, ed. D. R. Bates, Academic Press, New York (1962).

79. E. M. Little, W. E. Quinn, and F. L. Ribe, Phys. Fluids 4, 711 (1961).

80. E. V. Lifshitz, A. K. Berezin, and Yu. M. Lyapkalo, Sov. Phys.-Tech. Phys. 11, 798 (1966).

81. V. D. Shapiro, Sov. Phys.-JETP 17, 416 (1963).

82. J. Jancarik, T. P. Kochanski, and K. W. Gentle, Plasma Physics 21, 45 (1979).

83. S. Hamasaki, N. A. Krall, C. E. Wagner, and R. N. Byrne, Phys. Fluids 20, 65 (1977).

84. R. M. Eisberg, Fundamentals of Modern Physics, John Wiley, New York (1961).

85. T. Sato, L. C. J. M. de Kock, Th. G. A. Winkel, Plasma Physics 15, 925 (1973).

86. R. W. P. McWhirter and A. G. Hearn, Proc. Phys. Soc. 82, 641 (1963).

87. D. R. Bates, A. E. Kingston, and R. W. P. McWhirter, Proc. Roy. Soc. A257, 297 (1962).